

Diss. ETH Nr. 12331

**Scale Dependence of the Charm Production
Cross Section in Photoproduction
and Performance of the Central Silicon Tracker
at the H1 Experiment**

A dissertation submitted to the
Swiss Federal Institute of Technology Zurich
for the degree of
Doctor of Natural Sciences

presented by

Monika Biddulph

Dipl. Phys. Universität Gesamthochschule Siegen
born 14. Oktober 1966 at Siegen, Germany

accepted on the recommendation of
Prof. Dr. R. A. Eichler, examiner and
Dr. R. Horisberger, co-examiner

July 1997

Diss. ETH Nr. 12331

**Scale Dependence of the Charm Production
Cross Section in Photoproduction
and Performance of the Central Silicon Tracker
at the H1 Experiment**

A dissertation submitted to the
Swiss Federal Institute of Technology Zurich
for the degree of
Doctor of Natural Sciences

presented by

Monika Biddulph

Dipl. Phys. Universität Gesamthochschule Siegen
born 14. Oktober 1966 at Siegen, Germany

accepted on the recommendation of
Prof. Dr. R. A. Eichler, examiner and
Dr. R. Horisberger, co-examiner

July 1997

Abstract

At HERA, charm quarks are predominantly produced by quasi real photon-gluon fusion. The cross section is directly proportional to the gluon density in the proton. In winter 1994/1995, a new device for tagging scattered electrons with very little energy loss was installed in the H1 detector. In this work, the new electron tagger is used to measure the ep-cross section of the reaction $D^* \rightarrow K\pi\pi$ for the visible range ($p_t(D^*) > 1.8 \text{ GeV}$, $-1.5 < \eta(D^*) < 1.5$). The result is

$$\sigma_{vis}(ep \rightarrow D^* X) = (30.55 \pm 5.46_{stat} \pm_{3.96_{syst}}^{4.82}) \text{ nb}.$$

Using the Weizsäcker Williams Approximation to calculate the photon flux, and extrapolating from the visible range to the total kinematical range, the γp -cross section is calculated to be

$$\sigma_{\gamma p \rightarrow c\bar{c}} = (6.42 \pm 1.15_{stat} \pm 0.79_{syst,1} \pm_{0.45_{syst,2}}^{0.73} \pm 2.15_{theor}) \mu b$$

Using this new measurement together with three measurements of σ_{ep} obtained using data collected in 1994, a fit is performed to calculate the energy (W) dependence of the γp -cross section. Using a dependence of the form $\sigma = \sigma_0 W^{2\lambda}$ gives the following result on the slope parameter λ :

$$\lambda = 0.61 \pm_{0.24}^{0.28}.$$

In the winter 1994/1995, the Central Silicon Tracker was also installed in the H1 experiment at HERA. The construction and the readout of the CST are described. First data taken during the luminosity period of 1995 are analysed and the performance of the detector is discussed. An algorithm for hit-finding and noise suppression has been developed and a signal to noise ratio S/N of

$$\frac{S}{N}(p\text{-side}) = 11 : 1 \qquad \frac{S}{N}(n\text{-side}) = 4 : 1$$

has been found. The efficiency is estimated to be $\epsilon = 87\%$ for the p-side and $\epsilon = 41\%$ for the n-side.

Zusammenfassung

Bei HERA werden charm Quarks hauptsächlich in Photoproduktion durch den Prozeß der Photon-Gluon Fusion erzeugt. Hier ist der Wirkungsquerschnitt direkt proportional zur Gluondichte im Proton.

Im Winter 1994/1995 wurde ein neues Gerät zum Nachweis von unter sehr kleinen Winkeln abgelenkten Elektronen in H1 installiert. Die im ersten Teil dieser Arbeit beschriebene Analyse benutzt diesen sogenannten Elektron-Tagger, um den Elektron-Proton Wirkungsquerschnitt für die Reaktion $D^* \rightarrow K\pi\pi$ in dem für den Detektor sichtbaren Bereich ($p_t(D^*) > 1.8 \text{ GeV}$, $-1.5 < \eta(D^*) < 1.5$) zu messen. Das Ergebnis beträgt

$$\sigma_{vis}(ep \rightarrow D^* X) = (30.55 \pm 5.46_{stat} \pm 3.96_{syst}^{4.82}) \text{ nb}.$$

Unter Benutzung der Weizsäcker Williams Näherung wird der Photonenfluß berechnet, und mit der Extrapolation auf den gesamten kinematischen Bereich der Photon-Proton Wirkungsquerschnitt bestimmt:

$$\sigma_{\gamma p \rightarrow c\bar{c}} = (6.42 \pm 1.15_{stat} \pm 0.79_{syst,1} \pm 0.45_{syst,2}^{0.73} \pm 2.15_{theor}) \mu b$$

Zusammen mit drei Wirkungsquerschnitten, berechnet mit im Jahr 1994 aufgezeichneten Daten, wird eine Anpassungsrechnung durchgeführt, um die Abhängigkeit der Wirkungsquerschnitte von der Energie W zu bestimmen. Die funktionale Abhängigkeit wird als $\sigma = \sigma_0 W^{2\lambda}$ angenommen, und folgendes Ergebnis für die Steigung λ wird ermittelt:

$$\lambda = 0.61 \pm 0.28_{0.24}.$$

Ebenfalls im Winter 1994/1995 wurde das Zentrale Silizium Spurnachweisgerät in H1 eingebaut. Im zweiten Teil der vorliegenden Arbeit werden Bau und Auslese dieses Nachweisgerätes beschrieben. Anhand erster Daten aus der Betriebsperiode in 1995 werden Algorithmen zur Treffer Erkennung und Rauschunterdrückung entwickelt und Signal zu Rausch Verhältnisse S/N von

$$\frac{S}{N}(p - \text{Seite}) = 11 : 1 \qquad \frac{S}{N}(n - \text{Seite}) = 4 : 1$$

berechnet. Die Ansprechwahrscheinlichkeit wird zu $\epsilon = 87\%$ für die p-Seite und zu $\epsilon = 41\%$ für die n-Seite bestimmt.

Contents

Abstract	2
Zusammenfassung	3
Contents	5
1 The H1 Detector at HERA	6
1.1 HERA	6
1.2 HERA kinematics	10
1.3 Physics at HERA	11
1.4 The H1 Detector	14
1.4.1 The Luminosity System	17
1.4.2 The Electron Tagger at 44 m	19
1.4.3 The Central Tracking Chambers	20
1.5 The Trigger System and Calculation of Trigger Efficiencies	22
2 The Photoproduction of Charm Quarks	26
2.1 Production Processes	26
2.2 The Reconstruction of D^*	29
2.3 Simulation	30
3 The Cross Section	32
3.1 Determination of the Cross Section	32
3.2 D^* Selection	34
3.3 Determination of Reconstruction Efficiency and Acceptance	36
3.4 Systematic Errors	38
3.5 Results	39
3.6 Differential cross sections in $p_t(D^*)$ and $\eta(D^*)$	40
3.7 The W Dependence of the γp -Cross Section	45
3.8 Summary	50
4 The Central Silicon Tracker	51
4.1 Detectors	53
4.2 Mechanical Construction	58
4.3 Read Out Concept	59

4.4	The APC128	63
4.4.1	The Preamplifier	64
4.4.2	The Operation of the APC128	65
4.4.3	The Calibration Mechanism	67
4.5	The Decoder Chip	67
4.5.1	The Principle of the Clock Mechanism	69
4.5.2	The Current Supply - DAC	70
4.5.3	The Monitoring of Temperature and Supply Voltages	71
4.5.4	Testing the APC and Decoder Chips	73
5	Analysis of CST Data	76
5.1	Raw Data	76
5.2	Special Event Studies	78
5.3	Subtraction of the Chip Offset	79
5.3.1	Common Mode Calculation	80
5.3.2	Pedestal Subtraction	84
5.4	Noise	85
5.5	Hit Finding	87
5.6	Connection between CST Hits and H1 Tracks	88
5.7	Performance of the CST	91
5.8	Conclusions	95
	List of Figures	101
	List of Tables	102
	Bibliography	103
	Acknowledgements	106
	Curriculum vitae	107

Chapter 1

The H1 Detector at HERA

Collider particle physics experiments provide some of the most important recent knowledge of modern particle physics by producing collisions with ever greater centre of mass energy. Particles resulting from the collisions are then measured and their properties compared to theoretical predictions. To supply particle collisions with very high center of mass energy, storage rings can be used. In these storage rings two preaccelerated particle beams are accelerated to their final energies (going round in the rings clockwise and anti clock wise) and can be stored for several hours. In so called interaction points, the particles meet and collide. The fragments of the colliding particles and the newly produced particles can be detected in huge detectors built around the interaction points.

A short introduction into HERA, an electron proton ring collider is presented in this chapter. Then a brief overview of physics at HERA, together with a description of the kinematic variables used, is given. In the next section, the H1 detector is shortly described. The adjoining sections give more detailed descriptions of those components which are of importance in the following analysis.

1.1 HERA

HERA (Hadron Electron Ring Anlage) is a facility where protons and electrons are accelerated and stored in separate rings and brought to collision at very high energies at two interaction points. Its purpose is to investigate the proton structure at very small distances. It was put into operation in 1992.

Fig. 1.1 shows a sketch of the rings. Both electrons and protons are preaccelerated in smaller rings, then injected into the 6.3 km circumference rings of HERA and accelerated to their final energies. The proton ring is equipped with superconducting magnets in order to be able to achieve a proton energy of 820 GeV. In the electron ring, the electrons are accelerated to an energy of 27.5 GeV. Here, the maximum energy is limited by the synchrotron radiation power.

In 1994, it was decided to accelerate positrons instead of electrons. The reason was instabilities of the electron beam at high electron densities. These were caused by

positively charged gas ions which were pulled into the negatively charged electron beam. The positrons drive these ions away from the beam. Nevertheless, in the following, the word electron is used as a generic term both for positrons and electrons.

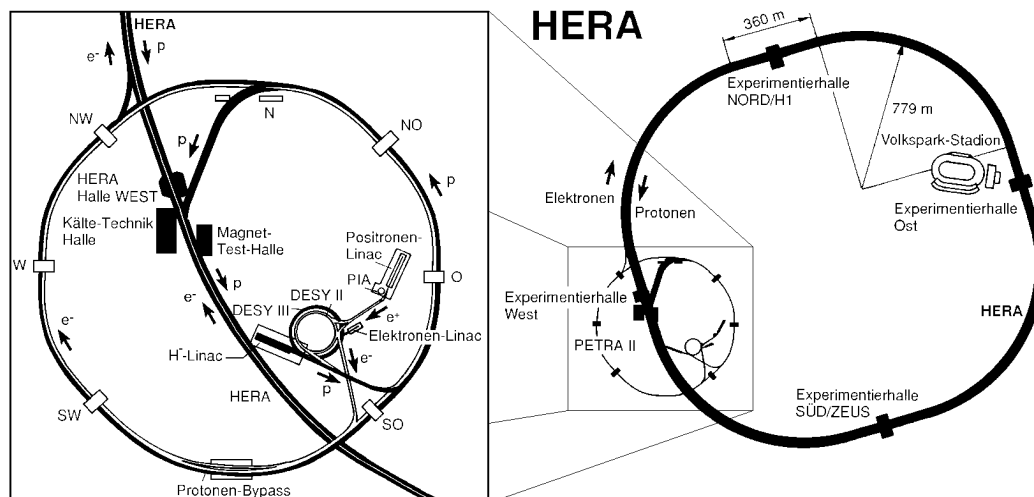


Figure 1.1: *The HERA ring collider at DESY in Hamburg. The Experiment H1 is situated in the north section of the ring.*

At a center of mass energy of 300 GeV the two beams collide at two interaction points. H1 is one of the experiments, at one of the interaction points, the other one being ZEUS [1]. Two more experiments use the HERA beams: HERA-B (for a description see for example [2]) and HERMES (e.g. [3]), which are fixed target experiments, the first using the proton beam to collide with a fixed wire target, the latter using the polarized electron beam on a polarized gas target to measure the proton spin structure.

The accelerated electrons and protons are bundled in bunches. These bunches 'sit' in so called RF (radio frequency) buckets. It is possible to have up to 210 bunch positions along the circumference of the storage ring, with bunch crossing intervals of 96 ns. In 1995 typically 189 electron bunches and 180 proton bunches were stored in the rings per fill, resulting in mean total currents of $I_e \approx 18 mA$ and $I_p \approx 54 mA$ (peak values were $I_e = 36 mA$ and $I_p = 73 mA$).

To estimate background rates and reactions with the beam gas, several of the electron and proton bunches are left without a partner to collide with (see bunch structure in fig.1.3). These bunches are called pilot bunches. In 1995, there were typically 15 electron- and 6 proton pilot bunches.

The longitudinal size of the proton bunch is of the order of a few tens of centimeters and is limited by the slope of the RF voltage, $\frac{dV}{dt}$, and depends therefore on the frequency. There are two frequencies used simultaneously to oscillate the cavities

which accelerate the beams. These are 54 MHz and 208 MHz. The highest frequency, 208 MHz, defines the size of the bunch length, which is of the order of 5 ns.

Sometimes the proton particles escape the main bunch and collect into neighbouring 208 MHz RF buckets. These bunches are then ahead in time (+5ns) or behind in time (-5ns) the main bunch and are called early or late satellites.

The H1 detector is designed to measure interactions that occur at the centre of the tracking system. It is possible for proton satellite bunches to collide with electron bunches, thus creating interactions which occur ± 75 cm away from the nominal interaction point. These interactions can, and do, trigger the H1 detector, but it is very difficult to reconstruct the event, and are therefore normally classed as background events. This is then a wasted trigger and contributes to the deadtime of the experiment. Therefore a good quality proton beam has the ratio I_{main}/I_{sat} as high as possible, where I_{main} is the current in the main bunch and I_{sat} is the current in the satellite bunch.

One way to show the ratio of the intensity of the main bunches to the satellite bunches is the use of the H1 forward time of flight system (FTOF). In the H1 reference frame, 'forward' is defined in the flight direction of the proton beam. The FTOF detector system consists of two scintillation counters which are mounted close to the beam pipe. Some of the protons in the beam collide with electrons or with the residual gas in the beam pipe and create particle showers which are detected by the FTOF. The FTOF measures the time of these showers with respect to the time that a normal interaction would occur. When the FTOF times are plotted for many particles it shows the rate of loss of protons as a function of position along the bunch. A typical time distribution, summed over all bunches, is given in fig1.2. The FTOF measures the loss of protons from the main and satellite bunches, which is not necessarily the number of protons in the main and satellite bunches. Nevertheless this measurement can be used to estimate the contribution of satellite bunch events to the luminosity measurement [4].

The analyses which are performed in this thesis use data collected with the H1 detector in 1995.

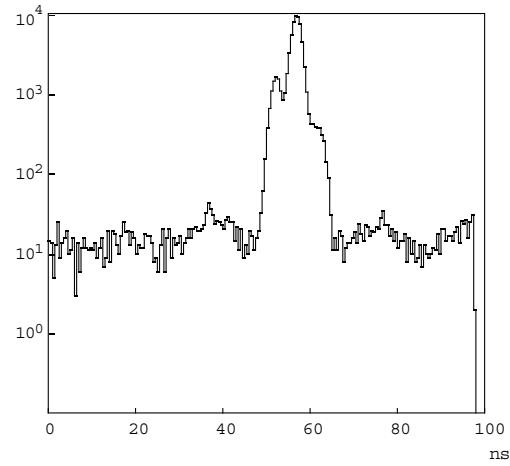


Figure 1.2: *Example of the proton bunch structure as measured by the H1 FTOF system. The horizontal axis shows the time scale in ns, the vertical axis shows the number of hits in the FTOF system. The main peak refers to the protons in the main bunches, the peaks left and right show the (5ns) satellites.*

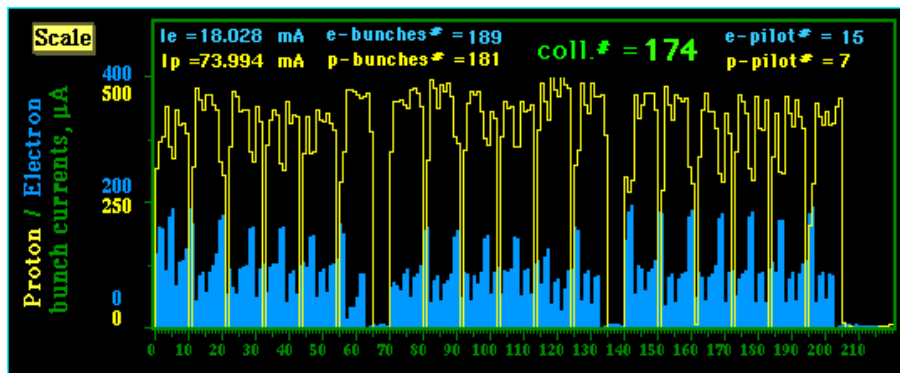


Figure 1.3: *Picture of the bunch population in HERA. The horizontal axis shows the bunch number and the vertical axis the current per bunch in μA .*

1.2 HERA kinematics

In order to give a good description of the physics processes, one needs a suitable set of variables which match the specific conditions at HERA. Fig.1.4 shows the kinematics of electron proton scattering at HERA. The four momentum of the incoming and of the scattered electron are described by (E_e, \vec{k}) and (E'_e, \vec{k}') , respectively, (E_p, \vec{p}) are energy and momentum of the incoming proton. The hadronic final state is indicated by X , and it's mass is described by $m_X^2 = E_{p'}^2 - p'^2$.

The positive z-axis points in the direction of the proton beam. The angle θ is measured between the positive z-axis and a particle track.

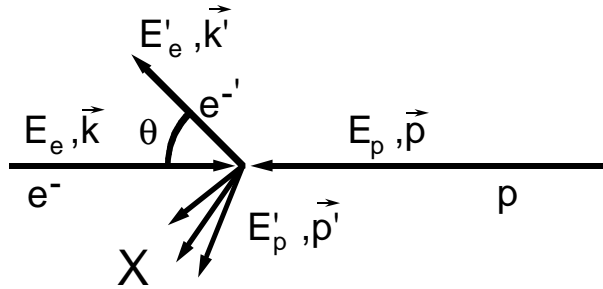


Figure 1.4: Kinematics of the ep scattering at HERA

To describe the kinematics in the H1 physics analysis, the following Lorentz invariant variables are used. Only three out of five variables are independent, and can be chosen to match the specific needs:

s	$=$	$(k + p)^2$	ep-center of mass energy squared
Q^2	$=$	$-q^2 = -(k - k')^2$	square of the four momentum transfer between electron and proton
x	$=$	$\frac{Q^2}{2 \cdot p \cdot q}$	Bjorken x, in the parton model language corresponding to the fraction of the initial proton momentum which is carried by the parton involved in the interaction, in the infinite momentum frame of the proton.
y	$=$	$\frac{q \cdot p}{k \cdot p}$	fraction of energy lost by the electron in the rest system of the proton
W^2	$=$	$\hat{s} = y \cdot s - Q^2$	γp system center of mass energy, squared

y and x range between zero and one. Using above formulae and neglecting the electron and proton masses one obtains in the laboratory frame of H1:

$$Q^2 = 4 \cdot E_e \cdot E'_e \cdot \cos^2 \frac{\theta_e}{2} \quad , \quad (1.1)$$

and

$$y = 1 - \frac{E'_e}{E_e} \cdot \sin^2 \frac{\theta_e}{2} \quad , \quad (1.2)$$

where θ_e is the polar angle of the scattered electron. Therefore an electron whose trajectory is only slightly deflected in the scattering process has $\theta_e \approx \pi$. For processes where Q^2 is almost zero ($Q^2 < 1 \text{ GeV}^2$), the photon is said to be quasi real, with

$$E_\gamma = y \cdot E_e.$$

Because of the low momentum transfer, the electron is deflected under very small angles. Therefore eq.1.2 can be simplified and y then gives the fraction of energy which the electron loses:

$$y \approx \frac{E_e - E'_e}{E_e}.$$

Some of the electrons can be detected in the electron taggers, which will be described in more detail in chapter 1.4.

A variable which is useful for the kinematical description of particles in the final state is the rapidity:

$$\eta = \frac{1}{2} \ln \left(\frac{E + p_z}{E - p_z} \right) = \text{arctanh} \left(\frac{p_z}{E} \right). \quad (1.3)$$

Under the assumption that the mass of the particle is much smaller than its transverse momentum, eq.1.3 can be approximated to:

$$\hat{\eta} = -\ln \operatorname{tg} \frac{\theta}{2} \quad (1.4)$$

where $\hat{\eta}$ is called pseudorapidity.

1.3 Physics at HERA

The highly energetic colliding $e^+ p$ beams at HERA and the hermetic detector provide the opportunity to measure physics processes over a wide kinematical range. New regions are explored for processes with very high four momentum transfer Q^2 , as well as for processes with low Q^2 and at low x in a range down to $x = 10^{-5}$.

For processes with high four momentum transfer Q^2 or with high transverse

momentum (p_t) tracks in the final state, the electron and proton scatter inelastically. The parton model describes these processes as incoherent scattering of the electron by quarks inside the proton. The basic assumption is that the collision occurs in two independent stages. First, the electron scatters off one parton. The time scale which is involved here is the time required to define the energy transfer. The second step, which takes place over a much longer time, is the recombination of partons to form the hadronic final state. Because the second step, the hadronisation, takes place over a much longer time scale, the two processes can be treated separately. This allows the deep inelastic γp -cross section to be factorized into the cross section on the partonic level describing the hard scattering process, and the parton density distributions [5].

$$\sigma_{\gamma p} = \int f_{q/p}(x_p, \mu_F) \hat{\sigma}_{\gamma q}(\hat{s} = x_\gamma x_p s) dx_\gamma dx_p.$$

Here $f_{q/p}(x_p)$ is the probability to find a quark with the energy fraction x_p in the proton and $\hat{\sigma}_{\gamma q}$ is the cross section of the hard process, at the γq -system center of mass energy \hat{s} .

Since the QCD coupling constant α_s is small at high scales, the short distance cross section can be calculated as a perturbative series in the running coupling of α_s .

The factorisation scale μ_F can be thought of as the scale which separates the long- and short distance physics. Thus a parton inside the proton, emitted with a small transverse momentum, less than the scale μ_F , is considered part of the hadron structure and is absorbed into the parton distribution. The scale μ_F is often chosen to be of the order of the scale which characterizes the hard interaction.

The process of interest in this work is the photoproduction of charm pairs, and is dominated by the process of photon-gluon fusion (see fig. 2.1). In the γg -center of mass (CM) system the energy squared $\hat{s}_{\gamma g}$ can be calculated using the four momenta of the outgoing quark and antiquark:

$$\hat{s}_{\gamma g} = (p_\gamma + p_g)^2 = (p_q + p_{\bar{q}})^2.$$

With $p_q = (E_q, \vec{p}_q)$ \hat{s} gives

$$\hat{s}_{\gamma g} = E_q^2 - \vec{p}_q^2 + E_{\bar{q}}^2 - \vec{p}_{\bar{q}}^2 + 2 \cdot E_q \cdot E_{\bar{q}} - 2\vec{p}_q \cdot \vec{p}_{\bar{q}}$$

Using $E^2 = m^2 + \vec{p}^2$, $m_q = m_{\bar{q}}$, and the fact that in the CM system $\vec{p}_q = -\vec{p}_{\bar{q}}$, results in

$$\hat{s}_{\gamma g} = 2 \cdot m_q^2 + 2 \cdot \vec{p}_q^2 + 2 \cdot (m_q^2 + \vec{p}_q^2)$$

and thus:

$$\hat{s} = 4 \cdot (m_q^2 + \vec{p}_q^2).$$

Since the scale μ_F should describe the hard interaction, the component of \vec{p} which is of interest here is the transverse momentum p_t , whereas p_L does not contribute to the 'hardness' of the scale. Additionally, the transverse component of the quark

momentum is independent of the boost along the z-axis. Therefore, as the hard scale,

$$\mu_F = \hat{s}_{\gamma g} = 2\sqrt{m_q^2 + p_{tq}^2} \quad (1.5)$$

is chosen.

The contributions to the cross section which are from long time scale physics, such as the distributions of quarks and gluons in hadrons, the parton density functions, can not be calculated perturbatively and have to be extracted from measurements. Parton density distributions are parametrized at some energy scale μ_0 and then evolved to higher values of the factorization scale μ_F using the Altarelli Parisi evolution equation or DGLAP (Dokshitzer-Gribov-Lipatov-Altarelli-Parisi) equation [6].

In reactions where no hard scale is present α_s is too large for perturbative expansion. The factorization theorem can not be applied and thus the cross section can not be calculated using perturbative QCD.

Physics analysis in this long time scale kinematical range includes the measurement of the total photoproduction cross section, which has been measured at a γp -center of mass energy of 200 GeV as $\sigma_{\gamma p, tot} = (165 \pm 2 \pm 11) \mu b$ [7], and of diffractive processes.

Diffractive processes are characterized by the exchange of a colourless object between the two colliding particles. The signature of such an event is a large rapidity gap in the final state.

Several different processes are characterized as diffractive: In quasi-elastic interactions, the proton remains intact while the photon is transformed into a vector meson, e.g. ρ, ω, ϕ or J/ψ , or either the photon or the proton breaks up into several hadrons, but no colour is exchanged between the two systems.

A successful theoretical concept of describing these 'soft' interactions is Regge theory. In Regge theory, the amplitude T for a high energy t-channel elastic scattering process at a center of mass energy \sqrt{s} and a momentum transfer t can be written as [8]

$$T(s, t) \sim \beta(t)\xi_a(t)\left(\frac{s}{s_0}\right)^{\alpha(t)},$$

where $\beta(t)$ is a real function of t and $\xi_a(t)$ is a definite phase calculated from the Regge trajectory $\alpha(t)$. The total cross section can be calculated from the elastic scattering amplitude by using the optical theorem:

$$\sigma_{tot} = \frac{1}{s} \cdot Im|T(s, t=0)| \sim \left(\frac{s}{s_0}\right)^{\alpha(t=0)-1} \quad (1.6)$$

and

$$\frac{d\sigma(elastic)}{dt} = f(t) \cdot \left(\frac{s}{s_0}\right)^{2\alpha(t)-2}, \quad (1.7)$$

where $f(t)$ is a function of t . A fit to the total γp -cross section data of the form of

$$\sigma_{tot} \sim Y \cdot s^{\alpha_{IR}(0)-1} + X \cdot s^{\alpha_{IP}(0)-1} \quad (1.8)$$

gives for the parameters $\alpha_{IR}(0) \approx 0.54$ and $\alpha_{IP}(0) \approx 1.08$. Here the first term arises from the exchange of light mesons, describing the low energy behaviour. The high energy features are due to pomeron exchange.

These two parameters are found to be universal for all hadron-hadron interactions [9].

An interesting kinematical region is the intermediate region between 'soft' and 'hard' physics. In this transition region perturbative QCD and Regge theory give different predictions, which can be compared to measurements. For example, two of the questions arising are whether the transition between 'hard' and 'soft' physics is abrupt or smooth, and what constitutes a 'hard' scale. A second question of interest is the W dependence of different processes.

Because of the possibility of measuring in high Q^2 as well as in low Q^2 ranges, HERA provides ideal means to investigate this interesting physics region. For further discussion the reader is referenced to chapter 3.7.

1.4 The H1 Detector

The H1 experimental program covers a wide range of different physics processes. Therefore a hermetic multi-purpose detector was designed and built, where tracks of charged particles can be measured with good precision and the energies of particles can be determined with good accuracy.

Since the proton at HERA carries a much higher momentum than the electron, there is a boost of the final state particles into the forward direction. To take this into account, the H1 detector is built asymmetrically. Fig.1.5 shows a 3-dimensional picture of the H1 detector as it was in 1994. A detailed description of this detector including all subsystems is given in [10].

The interaction region is surrounded by the central tracking chambers, which cover an angular range in theta of $25^\circ < \theta < 155^\circ$ and 360° in ϕ . These chambers are able to measure the tracks of particles both in the $r\phi$ - and z -coordinate and, as they are in a magnetic field, give a measurement with the accuracy σ_{p_t} of the transverse momentum p_t of about $\sigma_{p_t} \approx 1\% \cdot p_t^2$.

During the winter shutdown from 1994 to 1995 a central silicon tracker [11] was installed with the purpose of providing a very good space resolution in order to resolve secondary vertices. This detector is the subject of the second part of this thesis.

The central trackers are enclosed by the electromagnetic and the hadronic liquid argon calorimeters, respectively. The energy resolution of these calorimeters has been measured in test beams to be $12\%/\sqrt{E_e} \oplus 1\%$ for the electromagnetic part and $50\%/\sqrt{E_h} \oplus 2\%$ for the hadronic part.

The inner trackers and calorimeters are surrounded by a superconducting coil, which produces a uniform magnetic field in the central region of 1.15 Tesla directed towards

the positive z-axis.

Finally the iron magnet return yoke and the muon chambers, which are partly interleaved in it, surround the detector.

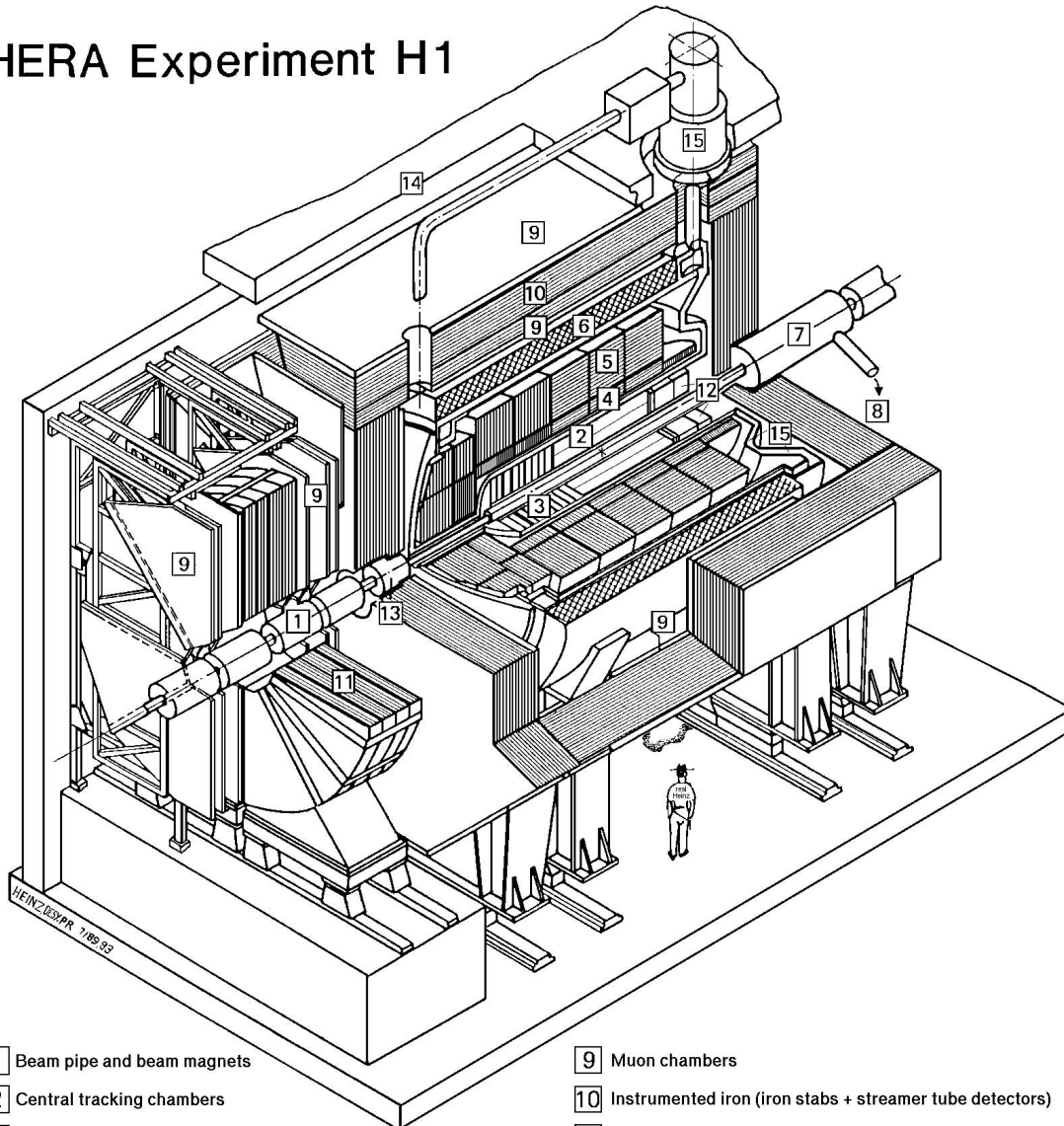
The asymmetric construction of the detector is apparent when comparing the forward and backward regions. The forward region is equipped with additional tracking chambers, with an angular acceptance of $7^\circ < \theta < 25^\circ$, to measure the momentum of particles boosted into the forward direction. The outer part of the forward region also has an additional muon spectrometer which consists of 6 layers of muon chambers surrounding an iron magnet with a toroidal field.

In the backward region, the backward multiwire proportional chamber (BPC) and the backward electromagnetic calorimeter (BEMC) were replaced in the winter shutdown of 1994 to 1995 by two new detectors, the BDC (Backward Drift Chamber) and the electromagnetic and hadronic SPACAL (Spaghetti Calorimeter) [12], [13]. These two new detectors, along with a new backward silicon tracker (BST) [14], give a much improved measurement of the energy and angle of the scattered electron.

The complete new central region with CST, BST, BDC and SPACAL as used since 1995 can be seen in Fig.1.8.

In the following, those components of the detector which play an important rôle in this thesis are described in detail.

HERA Experiment H1



- | | |
|--|--|
| 1 Beam pipe and beam magnets | 9 Muon chambers |
| 2 Central tracking chambers | 10 Instrumented iron (iron stabs + streamer tube detectors) |
| 3 Forward tracking and Transition radiators | 11 Muon toroid magnet |
| 4 Electromagnetic calorimeter (lead) | 12 Warm electromagnetic calorimeter |
| 5 Hadronic calorimeter (stainless steel) | 13 Plug calorimeter (Cu, Si) |
| 6 Superconducting coil (1.2T) | 14 Concrete shielding |
| 7 Compensating magnet | 15 Liquid Argon cryostat |
| 8 Helium cryogenics | |
- } Liquid Argon

Figure 1.5: Three dimensional picture of all detector components in the main H1 detector as of 1994. H1 components situated in the HERA tunnel down (backwards) the beam lines are shown in a separate picture.

1.4.1 The Luminosity System

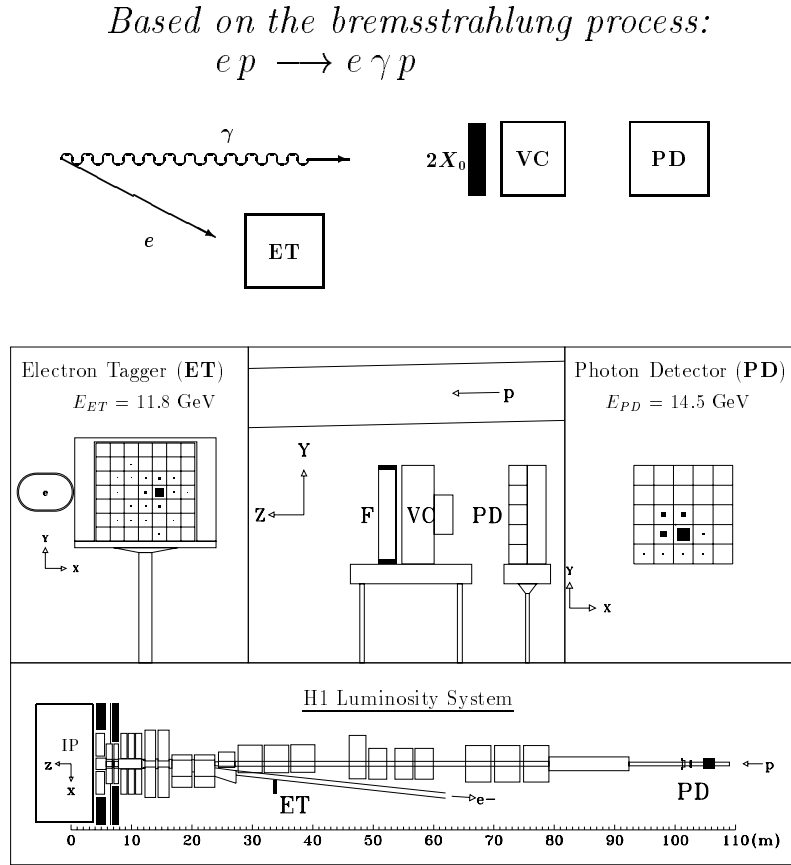


Figure 1.6: *Layout of the luminosity system downstream (backward) of the H1 experiment.*

The instantaneous luminosity is proportional to the instantaneous rate of Bethe-Heitler events: $ep \rightarrow e\gamma p$ (see ref [15]). This measurement can then be used to define the time integrated luminosity which is needed for the determination of the cross-section of any other process measured with the H1 detector. Therefore one of the most important measurements in H1 is the luminosity.

The outgoing e and γ are detected in coincidence by two Čerenkov detectors, situated at 103 m (photon counter) and 33 m (electron tagger) (see fig 1.6). This coincidence rate is then used to calculate the instantaneous luminosity, taking into account the acceptance of these detectors and the background rate, which is estimated using electron pilot bunches

The total luminosity accumulated during one year is the integrated luminosity for all relevant runs where the H1 detector is fully operational. There are several corrections that have to be applied to the total integrated luminosity, which compensate for various beam and detector features.

1. Satellite-bunch correction:

Although protons are bundled together in bunches during injection and acceleration, some protons escape the main bunches, but show up in smaller, so called satellite bunches before and after the main bunches. Since the interaction vertex of protons from satellite bunches with the electron bunches lies about 75 cm outside the nominal interaction point, these interactions are not used to extract physics results, and are therefore actively vetoed. The luminosity system can not distinguish between hits as close as 20 ns in time to the main bunch. The satellite bunches therefore contribute to the luminosity measurement and so a measurement is needed of the Bethe-Heitler rate from satellite interactions.

With the tracking chambers, using an un-biased trigger, a z-vertex distribution is measured. From this distribution the ratio of Bethe-Heitler events from the main bunches to the events from the satellite bunches for each luminosity fill can be calculated. Unfortunately the late satellite bunch vertex, which is the interaction vertex between electrons and those protons, which are behind in time of the main bunch, is outside the acceptance of the central tracking chambers. To be able to correct for the late satellite bunch as well, the assumption is made, that the loss rate is the same for the early and the late satellites. Then the FTOF time distribution is used to estimate the late satellite contribution.

2. High Voltage corrections:

It is possible that single detector components were not active during parts of runs. Physics analysis includes all events, where the detectors required for the analysis were switched on. The luminosity is always being measured during ep luminosity runs regardless of the state of detector high voltage, thus making a correction necessary.

The corrections are of the order of several percent of the total luminosity and depend on run ranges and sub-detector systems required.

3. Deadtime corrections:

Deadtime is the fraction of the total run time in which the detector is not ready to take data. The non ideal trigger and data acquisition chain make this correction necessary. Deadtime occurs at several steps of the data taking. Some reasons are the limitation of the data input rate due to event processing or the time between the triggering of one event and the initialisation of the experiment for triggering the next. Out of these different deadtime factors an overall correction is calculated for each run.

The actual correction factor depends strongly on beam conditions and ranges from few percent to 15 - 20 percent.

4. Corrections due to prescale factors:

The H1 detector is able to record events of different types within the same run. One trigger, called subtrigger, is composed out of several trigger elements. These trigger elements present logical statements, which are created with different hardware components. In order to take into account the various goals in physics analysis, different subtriggers are composed out of different trigger elements. So the trigger rate of each subtrigger is strongly dependent on its subtrigger elements,

on luminosity, on beam- and background conditions. If the rate of a subtrigger is too high and causes additional downtime, this subtrigger is prescaled, which means that only a predefined fraction of the events triggered are read out and stored.

1.4.2 The Electron Tagger at 44 m

The electron tagger at $-z = 44\text{ m}$ (ET44) [16] was installed in the winter shutdown from 1994 to 1995. Together with the electron tagger at 33 m (ET33, see fig. 1.6), which is part of the luminosity system, it provides very good means to detect, or tag, the scattered electrons. Both electron taggers are positioned downstream of an electron dipole bending magnet. The magnet deflects scattered electrons into the two taggers. Since the electron taggers are built very close to the beam line, they can measure electrons which are bent under very small angles, less than 5 mrad (ET33) or 3.5 mrad (ET44) with respect to the beam axis. Thus the energy acceptance range is $5.5 < E_{e'} < 22\text{ GeV}$ for the ET33 and for the ET44 centers at 24 GeV with a width of 1.5 GeV. This corresponds to an upper limit in Q^2 of 0.01 GeV^2 for the ET33 and of 0.009 GeV^2 for the ET44. A further description of the ET33 can be found in [10].

The acceptance of both taggers is strongly dependent on the electron beam position and tilt at the interaction point. For periods of constant beam position, the acceptance A is calculated with a precision of 6 %. Fig. 1.7 shows the acceptance curve for the ET44 for periods of different beam parameters as a function of y .

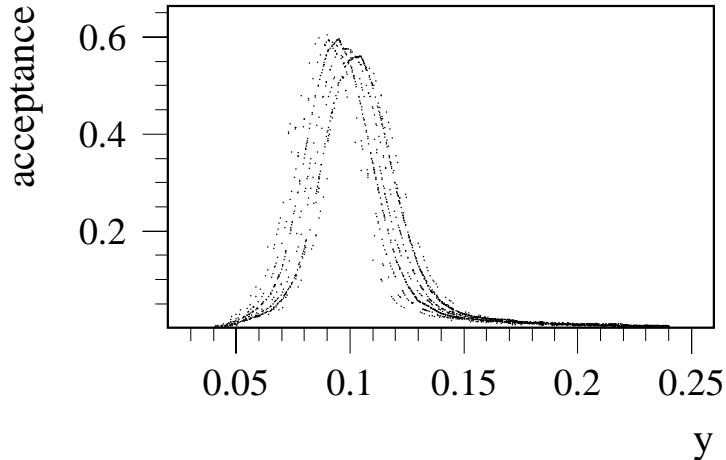


Figure 1.7: *Acceptance of the electron tagger at 44 m. The different curves represent different run ranges with different electron beam tilts.*

For E_e' above 12 GeV, the efficiency of the ET44 is about 98 %. However, there are problems in measuring the exact electron energy and therefore y . The reason for this lies in the detector design: The ET44 is a similar design to the ET33, it is built out of 2x3 crystal-blocks (78% TlCl / 22% TlBr), and situated very close to

the beam. So electrons which were deflected by a small angle hit the crystals very close to the detector edges. This results in a loss of electromagnetic showers, which are leaking out of the detector edges. Thus it is not possible to calculate the energy of the deflected electron in about 50 % of all cases. This leads to a large uncertainty in the calculation of y . Thus it is not possible to correct the acceptance on an event by event basis due to the large error in y .

A mean acceptance value of 11.44 % is used. This value is obtained by integrating the acceptance over the full y range of $0.04 < y < 0.24$, and varies by less than 2 % for different run ranges.

The ET33 detector is situated less closely to the beam and thus a precise measurement can be taken. Since an exact knowledge of the electron energy as measured by the ET33 is, too, needed for the luminosity calculation, this has been taken care of by using the outer crystal ring to veto hits with a too large leakage of electromagnetic showers.

1.4.3 The Central Tracking Chambers

Particle tracks are reconstructed with the information from the central tracking chambers. The central tracking system consists of 6 separate chambers which are shown in fig.1.8. Two multiwire proportional chambers (MWPC), namely the the central inner proportional chamber (CIP) and the central outer proportional chamber (COP), respectively, are thin, comparably low material density chambers whose main purpose is to provide signals for a fast first-level track trigger.

The purpose of the CIZ (central inner z-chamber) and the COZ (central outer z-chamber) is to measure the z coordinate to a high precision. Resolutions up to about 300 μm for the CIZ and between 200 to 500 μm for the COZ, depending on the track angle θ , have been measured. The CJC1 and CJC2 are the central inner- and outer jet chambers, respectively, and give a 3-dimensional track position.

Fig.1.9 shows a more detailed picture of a section of the central tracking system, viewed from the z-axis. An ionizing particle traversing the detector creates electrical signals in the readout electronics, which are interpreted as hits. The time of signal creation can be measured to a precision of about 4 ns, thus giving a space resolution in the $R\phi$ coordinate of about 200 μm . The anode wires are connected to preamplifiers on both (+z and -z) ends. The resolution in z is determined by comparing the signal heights from both ends of the anode wires. The resolution obtained by this measurement amounts to about 2 cm.

To compensate for the effect of the axial magnetic field on the drift direction of the electrons, the drift cells of the CJC are tilted in $R\phi$ by about 30° (see fig. 1.9). For each chamber, hits are grouped together forming a track candidate through the detector. Then all track pieces from the different trackers are connected to form track hypotheses. To each track candidate a helix is fitted and the 5 track parameters are calculated:

$$x(s) = \left(d_{ca} - \frac{1}{\kappa}\right) \cdot \sin\phi_{dca} + \frac{1}{\kappa} \cdot \sin(\phi_{dca} + \kappa \cdot s)$$

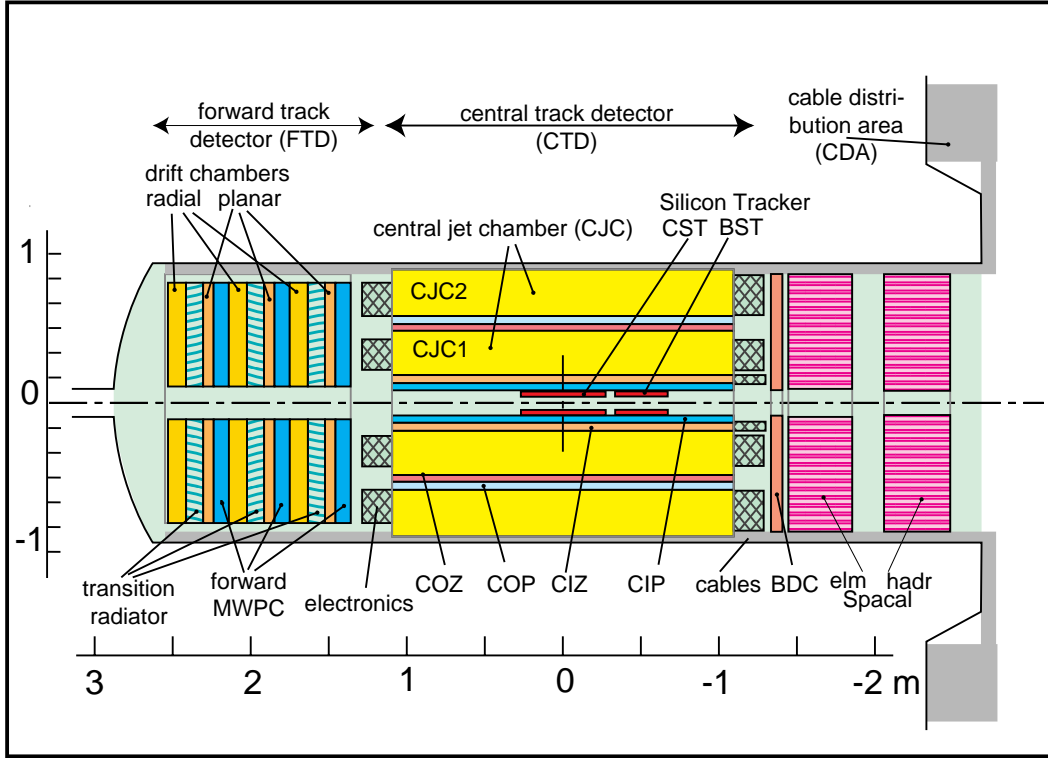


Figure 1.8: Side view of the central tracking of H1.

$$y(s) = -(d_{ca} - \frac{1}{\kappa}) \cdot \cos\phi_{dca} + \frac{1}{\kappa} \cdot \cos(\phi_{dca} + \kappa \cdot s)$$

$$z(s) = z_{dca} + \frac{1}{\tan\theta} \cdot s$$

Here s denotes the distance of a point from the d_{ca} point, measured along the projection of the track in the $R\phi$ plane. The parameters which determine the track of each particle are:

κ	κ is the inverse of the track curvature
d_{ca}	d_{ca} , distance of closest approach, is the closest distance of the track to the origin.
ϕ_{dca}	azimuth angle at the point of the distance of closest approach
z_{dca}	z-coordinate of the track at the point of the d_{ca}
θ	polar angle of the track.

The variable κ is negative for tracks from positively charged particles and positive for negative particles. The definition on the sign of the dca point is slightly more complicated, but has the advantage to be independent of the sign of κ : It is positive when the d_{ca} vector, the momentum vector and the positive z direction show a right handed system.

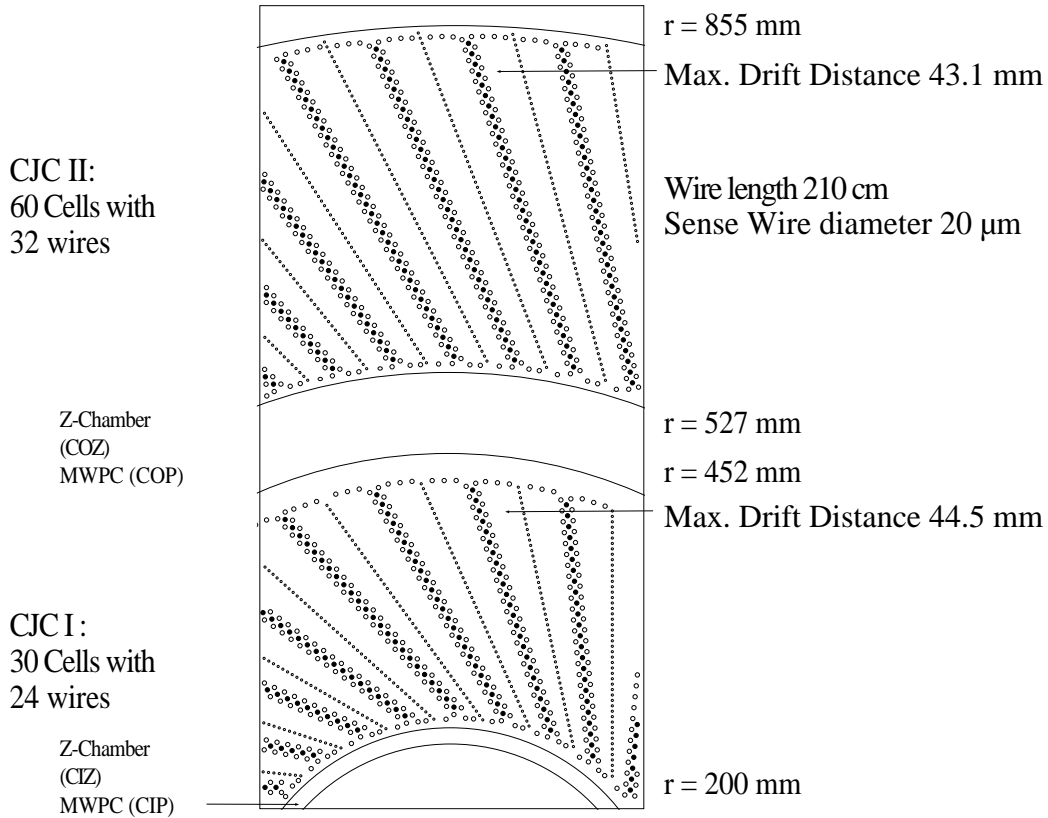


Figure 1.9: x - y view of a ϕ -section of the central jet chamber.

The run vertex is measured by fitting all tracks from the interaction region to a common vertex. These tracks are then called vertex fitted tracks. The track reconstruction efficiency is very well reproduced by the Monte Carlo simulation of the detector. A detailed analysis can be found in [17].

1.5 The Trigger System and Calculation of Trigger Efficiencies

The task of a trigger system is to select out of the huge rate of events those for permanent recording, that originate from an ep -interaction of physics interest, and to reject background events.

H1 has 5 different trigger levels:

Most subdetectors produce signals that can be used as first level (L1) triggers. The outputs of these L1 triggers are called trigger elements (TE). These TE are combined to make various subtriggers (ST) [18]. Out of 191 different TE, 121 ST are formed. All data of the subdetectors are stored in a pipeline of length $2.5 \mu\text{s}$, the decision time of the first level triggers. A positive decision of at least one of the ST stops the pipelines and therefore starts the deadtime, since no new event can be

recorded.

The level 2 trigger, which has a decision time of typically $20 \mu s$, evaluates a large number of detector correlations and uses, among others, topological correlations and neural networks. Only then, depending on the outcome of the level 2 (L2) decision, the detector readout is started, which takes of the order of $1 ms$, depending on the event.

Trigger level 3 (L3) is foreseen to further process the information available on L2. The raw data of the accepted event are then fed into the level 4 filter farm (L4). The filter farm is an asynchronous software trigger based on fast MIPS processor boards.

All events which survive the L4 are stored as raw data and are fully reconstructed. The level 5 (L5) reconstruction writes only those reconstructed events on disk, which fulfill certain minimum physics criteria, and flags the events for different physics classes.

To trigger photoproduction events with a low y the ET 44 has to be used. To suppress Bethe Heitler events and synchrotron radiation hits, no deposited energy greater than 1 GeV in the photon detector and greater than 200 MeV in the veto counter is required. Additionally, at least one track of a negatively charged particle with a transverse momentum above 450 MeV found in the CJs is required by using the $DCR\phi$ trigger element $DCR\phi_TNeg$ [19]. The z-vertex trigger element $zVtx_T0$ [20], which uses CIP and COP or CIP and forward tracker, requires at least one track which points to an interaction vertex ± 40 cm around the nominal vertex position which belongs to one ray. The subtrigger fulfilling all these requirements is subtrigger 84 (ST 84). The complete list of trigger elements forming the ST 84 is as follows:

- $ET44 \& Lu_PD \& Lu_Veto$
- $DCR\phi_TNeg$
- $zVtx_T0$
- $Btof_BG$
- $FTOF_IA \& !FTOF_BG$
- $Spcl_e_ATOF_e_tot$

The last three trigger elements are from veto scintillation counters. They use the time of flight systems. The $Btof_BG$ veto requires no deposited energy in the backward part around the beam pipe within the time window between two bunches, where no collisions of the main bunches take place (out of time). The same applies to the forward time of flight system: energy is requested to be deposited in the right timing or not in the wrong timing. The SPACAL time of flight system (TOF) is a time window set around the interaction time. The TOF veto of the electromagnetic SPACAL requires, that less than 50 % of the energy seen in the out of time window (ATOF) should have been seen in the TOF (ep -interaction time window).

The SPACAL veto trigger element which is used in the ST 84 is called *Spcl_e_ATOF_e_tot* and requires the total energy deposited in the TOF window to be above a certain threshold value.

Since the composition of the ST 84 changed during 1995, run ranges have to be defined and the luminosity has to be calculated accordingly.

For the trigger elements *DCRφ_TNeg* and *Spcl_e_ATOF_e_tot*, the efficiency has been calculated using each two different subtriggers. Since the two subtriggers only differ in one trigger element, the efficiency ϵ can be calculated simply by counting:

$$\epsilon_{DCR\phi_TNeg} = \frac{N_{ST_A} \& N_{ST_A \& DCR\phi_TNeg}}{N_{ST_A}}$$

$$\epsilon_{Spcl_e_ATOF_e_tot} = \frac{N_{ST_B} \& N_{ST_B \& Spcl_e_ATOF_e_tot}}{N_{ST_B}}$$

where '&' means a logical 'and' condition and ST_A and ST_B denote two different subtriggers. The efficiency of the trigger element *zVtx_T0* has been calculated using events generated by Monte Carlo simulation.

The timing veto trigger elements veto only events which lie outside the ep interaction time window. These triggers veto only background, and no data coming from events which result in the collision of two ep bunches. The error given for those trigger elements includes the error due to the possibility of accidental coincidences. It is assumed that in first order the trigger elements are independent and so the total efficiency of the ST 84 can be estimated as the product of the efficiencies of the trigger elements.

run range	trigger elements	trigger efficiency [%]	luminosity [nb^{-1}]
116859-117224 117601-121503	<i>DCRϕ_Tneg</i> <i>zVtx_T0</i> <i>ET44&Lu_PD&Lu_Veto</i> <i>Btof_BG</i>	99.8% $\pm_{2.4}^{0.2}$ % 99.7% $\pm_{5.2}^{0.3}$ % included in acc. corr. 100% \pm_1^0 %	468.2
121970-131045 (shifted vertex runs excluded)	<i>DCRϕ_Tneg</i> <i>zVtx_T0</i> <i>ET44&Lu_PD&Lu_Veto</i> <i>Btof_BG</i> <i>FTOF_IA&FTOF_BG</i> <i>Spcl_e_ATOF_E_tot</i>	99.0% $\pm_{1.7}^{1.0}$ % 99.7% $\pm_{5.2}^{0.3}$ % included in acc. corr. 100% \pm_1^0 % 100% \pm_1^0 % 96.5% ± 1.6 %	792.4

Table 1.1: Run ranges with corresponding trigger efficiency and integrated, satellite bunch, high voltage and deadtime corrected luminosity.

Chapter 2

The Photoproduction of Charm Quarks

To be able to calculate photoproduction of quarks with the help of perturbative QCD, the process has to be characterized by a hard scale. The masses of light quarks (u,d,s) are not big enough to serve as a hard scale. So for light quarks, perturbative QCD can only be used for processes where the transverse momentum can serve as a hard scale. For heavy quarks(b,t), the masses of the quarks are big enough to provide a scale.

For HERA energies, charm photoproduction presents an intermediate state: A complete NLO QCD calculation [21] shows the distribution of the transverse momentum of the charm quarks at HERA energies ($E_p = 820 \text{ GeV}$, $W_{\gamma p} = 200 \text{ GeV}$). Although the distribution falls exponentially towards high p_t , due to a cut on the transverse momentum of 1.8 GeV for the D^* (see chapter 3.2), most charm quarks are analysed with a transverse momentum of the same order of magnitude as their mass. As shown in chapter 1.3, $\mu_F = 2\sqrt{m_q^2 + p_{tq}^2}$ is chosen for the process of boson-gluon fusion ($\gamma p \rightarrow c\bar{c}X$). For the QCD calculations which are quoted in this work [21], $\mu_F = 2\mu_0 = 2m_c$ for the factorisation scale and $\mu_R = \mu_0 = m_c$ for the renormalisation scale is chosen [23], with $\mu_0 = \sqrt{p_{tc}^2 + m_c^2}$. The renormalisation scale is then varied between $0.5 m_c < \mu_R < 2 m_c$ to estimate the impact of the choice of scale on the result of the cross section. Further discussion on this subject can be found in chapter 3.5.

2.1 Production Processes

In photoproduction, quark pairs can be produced by direct and resolved processes.

Direct process:

In leading order (LO) photoproduction, the only process where quark pairs can be produced is the boson gluon fusion. A quasi real photon is emitted by the electron and generates, together with a gluon from the proton, a $c\bar{c}$ pair.

Using $y = \frac{E_\gamma}{E_e}$, the square of the center of mass energy in the γg -system can then

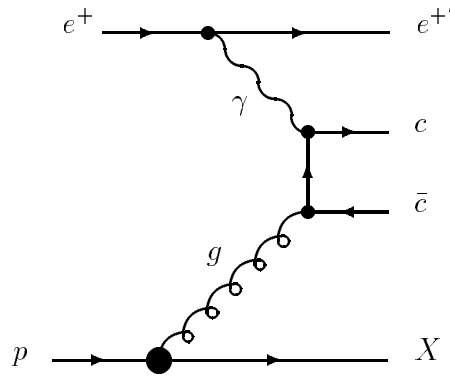


Figure 2.1: *Feynman diagram of the boson gluon fusion, producing a $c\bar{c}$ pair.*

be described as:

$$\hat{s} = s_{\gamma g} = y x_g s_{ep} = 4y x_g E_e E_p.$$

To produce a $c\bar{c}$ pair, the γg -center of mass energy $\sqrt{\hat{s}}$ has to be above $2m_c$. This leads with $y(ET44) < 0.24$ and a charm mass of 1.5 GeV to a limit on x_g of $x_g \geq 1.4 \cdot 10^{-4}$.

The total charm photoproduction cross section $\gamma + g \rightarrow (c + \bar{c}) X$ is given by:

$$\sigma_{\gamma p}(y) = \sigma(\gamma p \rightarrow c\bar{c}X) = \int g(x_g, \mu_F^2) \hat{\sigma}_{\gamma g}(\hat{s}) dx_g. \quad (2.1)$$

Here $\hat{\sigma}_{\gamma g}$ is the photon gluon cross section at the γg -center of mass energy $\sqrt{\hat{s}}$ and $g(x_g, \mu_F^2)$ the function which describes the gluon density in the proton, given at the factorisation scale μ_F .

The Weizsäcker Williams Approximation (WWA) [24] is used to calculate the photonflux $f_{\gamma/e}$ [25]:

$$f_{\gamma/e}(y) = \frac{\alpha_{em}}{2\pi} \left\{ \frac{1 + (1-y)^2}{y} \cdot \ln \frac{Q_{max}^2}{Q_{min}^2} - 2 \frac{1-y}{y} \right\} \quad (2.2)$$

with

$$Q_{max}^2 = E_e^2 (1-y) \cdot \theta_{min}^2 \quad Q_{min}^2 = \frac{(y \cdot m_e)^2}{1-y}.$$

Here $\theta_{min}^2 = 3.5 \text{ mrad}$ for the ET44 and $\theta_{min}^2 = 5 \text{ mrad}$ for the ET33 .

Using eq. 2.2, the ep -cross section can be calculated to:

$$\sigma_{ep} = \sigma(ep \rightarrow ec\bar{c}X) = \int f_{\gamma/e}(y) \sigma_{\gamma p}(y) dy. \quad (2.3)$$

resolved process:

Besides the direct boson-gluon process, there is the possibility of a fluctuation of

the photon into a hadronic state. This possibility is described with parton density functions as well. One important process is the fluctuation of a photon into a $q\bar{q}$ pair which radiates a gluon. This gluon undergoes a reaction with a gluon from the proton to form a $c\bar{c}$ pair ($g + g \rightarrow c\bar{c}$). The cross section is proportional to the gluon density in the photon (see fig 2.2).

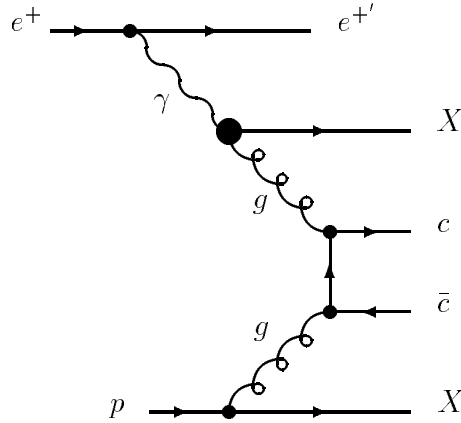


Figure 2.2: Example of a Feynman diagram of the hadronic component of the boson gluon fusion producing a $c\bar{c}$ pair in lowest order.

For the hadronic process, only a fraction of the photon energy (x_γ) is used in the charm photoproduction process. On average, the $c\bar{c}$ system moves more in the proton direction than in the direct process, the transverse momenta of the produced charm quarks are smaller and the rapidity is larger. The fraction of the hadronic, or resolved component of the total cross section is calculated to be about 20 %, and can be further reduced with cuts on momentum and rapidity [17]. For this calculation, the GRV-G-HO [26] parametrisation of the gluon density in the photon has been used, which agrees reasonably well with H1 data. A complete next to leading order calculation for HERA kinematics can be found in [27].

According to the LAC1 parametrisation [28] this fraction is even similar in size to the direct component, although recent measurements of the gluon density at H1 rule out the LAC1 parametrisation [29].

Theoretical calculations have large errors due to several uncertainties: One of them is the mass of the charm quark. Variation of the charm mass leads to large variation in the total cross section [30]. In the following, a charm mass of $1.5 \text{ GeV}/c$ is used, since, among others, the results of fixed target experiments are in good agreement with this mass.

The choice of the factorisation scale μ_F and the renormalisation scale μ_R are not clear cut, and depend on mass and transverse momenta of the particles participating in the hard process. To estimate the influence of the scaling variables μ_F and μ_R on the cross section, the calculations are done for $\mu = 2m_c$ and for $\mu = 0.5m_c$ (see fig. 3.3). However, both calculations seem to agree with the experimental results within their errors.

2.2 The Reconstruction of D^*

One way to verify the production of charm quarks is to reconstruct a hadron with charm. The decay

$$D^{*\pm} \rightarrow D^0 \pi_s^\pm \rightarrow (K^\mp \pi^\pm) \pi_s^\pm$$

provides a good possibility. Together with its isospin partner D^\pm , the D^0 is the lightest hadron with charm. It is the $J^P = 0^-$ state of a c and a \bar{u} quark and can only decay through the weak interaction. The difference between the vector mesons D^{*+} and D^{*0} and the pseudoscalars D^+ and D^0 is the spin configuration of the quarks.

For the present analysis, the lifetime of the D^* is of no significance, and for the track linking and vertex fitting the D^* are assumed to come from the main event vertex. The mass difference between D^* and D^0 has been measured [31] to

$$\Delta m = m_{D^*} - m_{D^0} = (145.42 \pm 0.05) \text{ MeV}.$$

Since this is a little more than the mass of a pion, the strong decay of a D^* into a D^0 is possible:

$$D^* \rightarrow D^0 \pi_s.$$

The branching ratio has been measured to $BR = (68.3 \pm 1.4) \%$ [31].

When reconstructing the decay chain, the small mass difference $m_{D^*} - (m_{D^0} + m_\pi) = 5.93 \text{ MeV}$ is of great advantage because it gives only small phase space for accidental combinatorics. This pion is often called 'slow' pion because of its low momentum in the D^* rest frame.

At HERA many of the pions which are belonging to the D^* decay are just recognizable because of their low momenta. Therefore it is important to quantify the reconstruction efficiency of particles with low transverse momentum. This has been studied in detail in [17]: The difference in track reconstruction efficiency between Monte Carlo simulation and data was calculated to be less than 3 %. So for the decay of a D^* particle, where three tracks in the central region are required, the upper limit on the resulting inefficiency is 9 %. To take this into account, for the analysis an systematic error of $\pm_0^9 \%$ is quoted. Out of several possible decay channels, the decay $D^0 \rightarrow K^\mp \pi^\pm$ ($Br(D^0 \rightarrow K\pi) = (3.83 \pm 0.12) \%$ [31]) has been chosen because of its low track multiplicity and thus lower combinatorial background.

In the H1 detector particles can be identified using the specific ionization in the tracking chambers. Since K/π identification is only possible for momenta lower than 500 MeV, this can not be used in case of the D^0 decay products, since many particles carry higher momenta. Thus to find the D^0 decay, each reconstructed track is assigned both hypotheses of a kaon and a pion. It is checked whether the invariant mass of the track pair lies close to the D^0 mass of 1.865 GeV:

$$m_{K\pi} = \sqrt{m_K^2 + m_\pi^2 + 2(E_K E_\pi - \vec{p}_K \vec{p}_\pi)}.$$

The third track is assigned the rôle of the slow pion, thus the three tracks together form the whole decay. The invariant mass of the three candidates can be calculated, assuming m_K, m_π as referenced in [31]:

$$m_{(K\pi)\pi_s} = \sqrt{m_{K\pi}^2 + m_{\pi_s}^2 + 2((E_K + E_\pi)E_{\pi_s} - (\vec{p}_K + \vec{p}_\pi)\vec{p}_{\pi_s})}.$$

When the reconstructed decay shows a real D^* , then $m_{(K\pi)\pi_s}$ and $m_{K\pi}$ are strongly correlated. Therefore the mass difference Δm between D^* hypothesis and D^0 hypothesis will give a narrower signal peak than the D^* signal peak alone [32], where Δm is defined as

$$\Delta m = m_{(K\pi)\pi_s} - m_{K\pi}.$$

The fragmentation of a charm quark into a D^* meson has been measured in e^+e^- experiments $B_c(c \rightarrow D^*) = 0.2604$. In [33] the total decay fraction has been measured to:

$$B_{DF}(c \rightarrow K\pi\pi) = B_c(c \rightarrow D^*) \cdot Br(D^* \rightarrow D^0\pi_s) \cdot Br(D^0 \rightarrow K\pi) = (7.1 \pm 0.5) \cdot 10^{-3}.$$

2.3 Simulation

To simulate events, the Monte Carlo generators PYTHIA [34] and AROMA [35] have been used.

PYTHIA is an event generator designed to generate hard or soft processes in collisions between leptons, hadrons and photons. An interface in the PYTHIA generator, called IJRAY, uses the Weizsäcker Williams approximation to generate a virtual photon. The hadronic component of the photon is modeled by the GRV-G-LO [26] parametrisation and the angle and energy of the deflected electron is given. The kinematics of photon and proton are then used as input to PYTHIA. For the proton structure functions, the GRV-LO [36] parametrisation is taken. Initial state parton showers are built up from each of the initiator partons from the two beams. In the following hard process, partons are produced which may branch to built up final state hadrons. The outgoing quarks and gluons are then fragmented to colour neutral hadrons using the Lund string fragmentation model [37].

AROMA is a package to simulate the production of heavy quarks through the boson gluon process in ep -collisions. The complete matrix elements to order $\alpha^2\alpha_s$ for the boson-gluon process are calculated. Higher order radiation is treated using initial state and final state parton showers. For the proton structure function, the MRS-H parametrisation has been taken [38]. Hadronisation is performed using Lund string fragmentation. For both generators, hadrons with a lifetime $\tau < 0.8 \cdot 10^{-8}$ s are decayed at the nominal interaction vertex.

The generated events, which contain as kinematical information the four momenta of the particles, are then used as input for GEANT [39].

GEANT is a detector simulation package which performs two tasks: first, a simulation of all those physics processes is done which take place when a particle

traverses the detector, e.g. multiple scattering, dE/dx , bremsstrahlung and hadronic interactions.

Second, in a so called digitization step, the detector response is simulated.

The output of the detector simulation program contains raw data banks. These simulated events are treated like data and further processed using the level 5 reconstruction.

Chapter 3

The Cross Section

In this chapter, the determination of the total $\gamma p \rightarrow c\bar{c}$ cross section in the y -range $0.04 < y < 0.24$ is described. First, a brief introduction of the method and then basic formulas needed are given.

For the data selection, two different sets of cuts are introduced and explained: Selection cuts to obtain a D^* candidate sample from the data taken during 1995, and analysis cuts to restrict the sample and allow for a D^* selection with less background. Here the possible sources of background to the process are discussed. Then the number of D^* s is calculated with a fit to the data, subtracting the contribution of the combinatorial background.

The ep-cross section is given in the visible range, which is defined as the kinematical range in which cross sections can actually be measured and which is limited by the acceptance of the detector. The cross section for the visible range presented in this analysis is thus measured without extrapolation in $p_t(D^*)$ and $\eta(D^*)$. Extrapolating from the visible range to the total kinematical range and taking into account the photon flux and the fragmentation ratio, the total γp -cross section at $\bar{W} = 95$ GeV is determined and the contributing systematic errors are then discussed.

The result on the visible ep -cross section in the y -range of $0.04 < y < 0.24$ (ET44) is used together with σ_{ep} obtained for three different ranges in y using 1994 data [40] to estimate the W and the y dependence respectively, of $\sigma_{\gamma p}$. This result is then compared to results of other processes, where a W dependence on the cross section has been evaluated.

3.1 Determination of the Cross Section

From the number of D^* s measured, the visible cross section can be calculated:

$$\sigma_{vis}(ep \rightarrow D^* X) = \frac{N(D^* \rightarrow K\pi\pi)_{measured}}{Br(D^* \rightarrow K\pi\pi) \cdot \epsilon_{trig} \cdot L_{cor} \cdot (\epsilon A)_{etag44} \cdot (\epsilon A)_{rec}} \quad (3.1)$$

where :

- $N(D^* \rightarrow K\pi\pi)_{measured}$: number of D^* 's measured with subtrigger 84 (ST84) in 1995
(here D^* stands for both the positive and the negative particles).
- branching ratio: $Br(D^* \rightarrow K\pi\pi) = 0.0262$
- L : deadtime, satellite bunch and HV corrected integrated luminosity
- $(\epsilon \cdot A)_{rec}$: reconstruction efficiency \cdot detector acceptance for events with at least one D^* in the given p_t, η, Q^2, y range
- $(\epsilon \cdot A)_{etag44}$: efficiency \cdot acceptance of the electron tagger at 44m, averaged over the given y -range
- ϵ_{trig} : total trigger efficiency of all remaining components of ST84

Since the definition of the ST84 changed during the year, the data taking period is split into two parts (A and B). For both parts, the luminosity is corrected for the corresponding trigger efficiency. Therefore $L \cdot \epsilon_{trig}$ has to be replaced by:

$$L_{cor} = \epsilon_{trig,A} \cdot L_A + \epsilon_{trig,B} \cdot L_B = 1.223 pb^{-1}. \quad (3.2)$$

The product of acceptance and reconstruction efficiency is different whether the process is direct or resolved. Taking into account a mean γp center of mass energy of 95 GeV, the relative contributions of direct and resolved components to the total γp cross section are:

$$\frac{\sigma_{dir}}{\sigma_{tot}} = 80.3 \% \quad \frac{\sigma_{res}}{\sigma_{tot}} = 19.7 \%.$$

For this calculation, the MRS-H [38] parametrisation for the proton structure function, the GRV-G-H0 [26] parametrisation for the photon structure function and $\lambda_{QCD} = 152 MeV$ were used.

This yields for the reconstruction efficiency:

$$(\epsilon \cdot A)_{rec} = \epsilon_{dir} \cdot A_{dir} \cdot \frac{\sigma_{dir}}{\sigma_{tot}} + \epsilon_{res} \cdot A_{res} \cdot \frac{\sigma_{res}}{\sigma_{tot}}. \quad (3.3)$$

Using

- EF: extrapolation factor from visible ($p_t(D^*), \eta(D^*)$) range to complete range
- Fl: Photonflux for $0.04 < y < 0.24$
- total decay fraction: $B_{DF}(c \rightarrow K\pi\pi) = 0.0071$

to extrapolate from the visible cross section, the total γp charm cross section $\sigma(\gamma p \rightarrow c\bar{c})$ can be calculated under the assumption, that the γp cross section does not depend strongly on y .

$$\sigma_{ep} = \int_{y_1}^{y_2} \sigma_{\gamma p}(y) \cdot f_{\gamma/e}(y) \cdot dy \approx \sigma_{\gamma p}(\bar{y}) \int_{y_1}^{y_2} f_{\gamma/e}(y) \cdot dy \quad (3.4)$$

The γp cross section then is approximated by calculating $\sigma_{\gamma p}(\bar{y})$, using a mean value \bar{y} .

$$\sigma_{\gamma p}(\bar{y}) = \frac{\sigma_{vis} \cdot EF \cdot Br(D^* \rightarrow K\pi\pi)}{2 \cdot B_{DF}(c \rightarrow K\pi\pi) \cdot Fl}. \quad (3.5)$$

The photon flux is calculated using the WWA, with the assumption to have a constant γp cross section over the given y range:

Thus for $0.04 < y < 0.24$ the photon flux gives

$$Fl = \int_{y_1}^{y_2} f_{\gamma/e}(y) \cdot dy = 5.09 \cdot 10^{-2}.$$

3.2 D^* Selection

All runs were used where the mean interaction vertex was at the nominal vertex position (center of the H1 detector). The **level 5 cuts** to select D^* candidates from the data stream were very loose:

- interaction vertex within 30 cm of the nominal vertex

- transverse momentum:

$$\begin{aligned} p_t(K, \pi) &\geq 250 \text{ MeV} \\ p_t(\pi_s) &\geq 100 \text{ MeV} \\ p_t(D^*) &\geq 1.5 \text{ GeV} \end{aligned}$$

- invariant masses:

Signal	$M_{K\pi} - M_{D^0}$ < 400 MeV	for	$0.0 < \Delta m < 155 \text{ MeV}$
	$M_{K\pi} - M_{D^0}$ < 100 MeV	for	$155 < \Delta m < 170 \text{ MeV}$
Background	$M_{K\pi} - M_{D^0}$ < 100 MeV	for	$0.0 < \Delta m < 170 \text{ MeV}$

The above mentioned selection cuts are not strong enough to yield a reasonable signal to noise ratio. Thus it is necessary to tighten the selection cuts. The final **analysis cuts** are as follows:

$$\begin{aligned} |m_{K\pi} - m_{D^0}| &< 80 \text{ MeV} \\ p_t(D^*) &> 1.8 \text{ GeV} \\ p_t(\pi, K) &> 350 \text{ MeV} \\ p_t(\pi_s) &> 120 \text{ MeV} \\ |\eta(D^*)| &< 1.5 \end{aligned}$$

The cut on $p_t(\pi_s)$ was chosen as low as possible, but such that the track reconstruction efficiency is above 90 %. The cut in η restricts the data sample to the acceptance region of the central tracking chambers. Furthermore it improves the signal to background ratio and gives a clear definition for the Monte Carlo simulation.

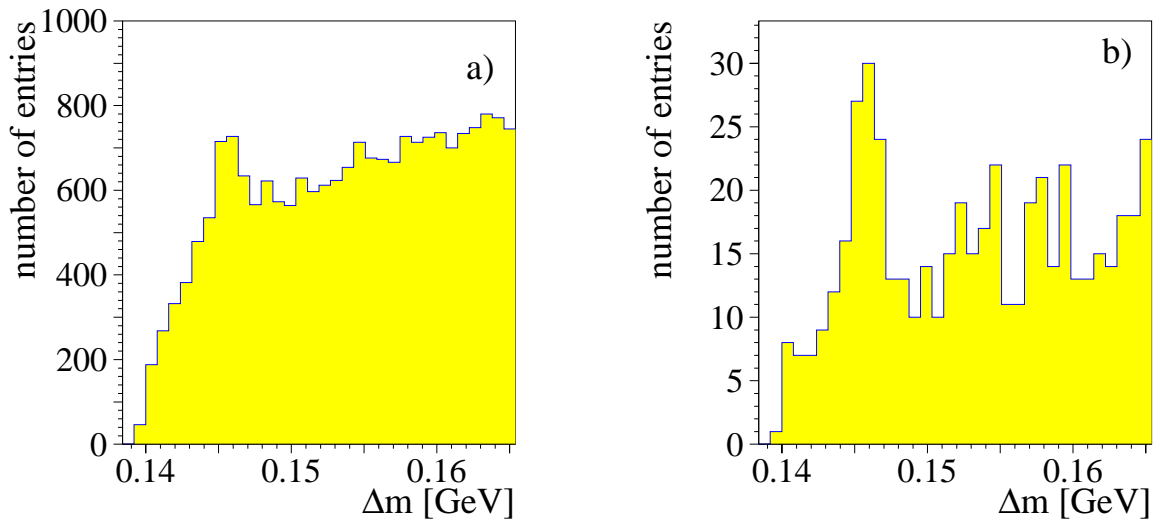


Figure 3.1: Δm distribution, for D^* s from all subtriggers (a) and for D^* s triggered by subtrigger 84 (b), both pictures after applying the analysis cuts.

Fig. 3.1 shows the distribution of the mass difference Δm for all D^* where the reconstructed D^0 has a mass within ± 80 MeV of the nominal value of 1.86 GeV. Part a) shows the distribution with all subtriggers, part b) only with D^* s triggered by the ST 84. As can be seen, the D^* signal sits on top of a combinatorial background. To obtain a number on D^* , the background has to be subtracted: For the peak region, it is not possible to distinguish whether a certain event is a D^* decay or not on purely kinematical knowledge. In this analysis, it is chosen to calculate the shape of the combinatorial background by analysing the wrong charge combinations. The wrong combinations that can be used are:

- $(K^+ \pi^+) \pi^-$ instead of $(K^+ \pi^-) \pi^-$
- $(K^- \pi^-) \pi^+$ instead of $(K^- \pi^+) \pi^+$.

Those wrong charge combinations where the slow pion carries the wrong charge can not be used. If a correct D^0 gets assigned correctly, but the particle masses of K and π are permuted, it is again in the correct mass window, and shows up in the Δm plot as a peak. In these cases, the peak is smaller, since some of the D^0 migrate out of the peak region.

The distributions for right sign and wrong sign combinations do not in general have the same number of entries. The reason is the unequal number of possible combinations for each case: To take this into account, the normalisation of the background distribution is left as a free parameter.

The form of the distribution near threshold is determined by the phase space for the combinatorics. The pions, which form together with a D^0 candidate a Δm

value in the correct mass window, occupy a very limited phase space. Thus the pion density in this phase space can be assumed to be approximately constant. The number of accidental combinations of a D^* candidate with an invariant mass between m and $m + dm$, can be estimated to be

$$dn \sim \sqrt{\Delta m - m_\pi} \cdot dm.$$

This can be generalized to

$$\left(\frac{dn}{dm}\right)_{BG} = P_4 \cdot \left(\Delta m - m_\pi\right)^{P_3}. \quad (3.6)$$

Thus the function to fit the data has the form:

$$\frac{dn}{dm} = P_1 \cdot e^{-0.5 \cdot \frac{(\Delta m - 0.1454)^2}{\sigma^2}} + P_2 \cdot (\Delta m - m_\pi)^{P_3}. \quad (3.7)$$

The number of D^* s is obtained by using equation 3.7 to fit background and data simultaneously and applying the method of maximum Likelihood. In order to allow for different absolute numbers in the right sign and wrong sign combinatorial backgrounds, the amplitude is left as a free parameter (P_2, P_4), whereas the form of the distribution (P_3) is assumed to be the same. N is then obtained from the area under the gaussian distribution, background subtracted. The fit in fig. 3.2 yields a width of $\sigma = 0.9 \pm 0.2 \text{ MeV}$. The number of events obtained is:

$$N = 56 \pm 10.$$

A variation of the width of the distribution of $\pm 1\sigma$ leads to a systematic error of 9 % on the number of events in the gaussian distribution. Fig.3.2 shows the D^* distribution (points) with the wrong sign combinations (histogram) and the fit (solid line).

3.3 Determination of Reconstruction Efficiency and Acceptance

The detector efficiency ϵ and the detector acceptance A are obtained using a Monte Carlo simulation.

The product $(A \cdot \epsilon)_{rec}$ is determined each from direct and resolved Monte Carlo using the following expression:

$$(\epsilon \cdot A)_{dir/res}^{rec} = \frac{N_{MC_{dir/res}}^{rec} \left(p_t(D^*), |\eta(D^*)|, p_t(\pi, K, \pi_s), Q^2, y, \theta(tracks) \right)}{N_{MC_{dir/res}}^{gen} \left(p_t(D^*), |\eta(D^*)|, Q^2, y \right)}$$

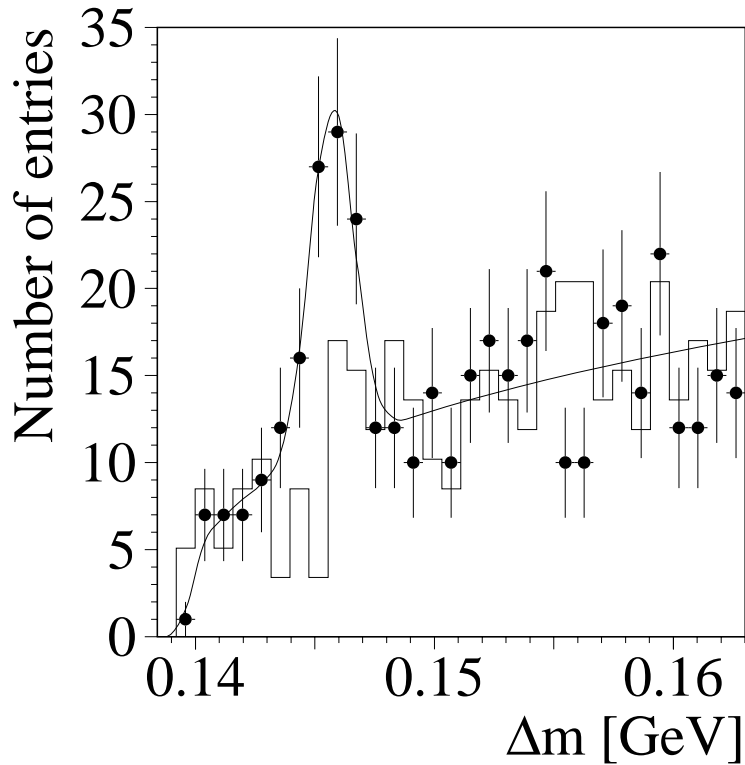


Figure 3.2: Δm distribution, for events triggered by ST 84. The solid line represents the wrong sign combinatorial background, the fitted curve is obtained using eq. 3.7.

where $0.04 < y < 0.24$ and $Q^2 < 0.009 \text{ GeV}^2$. This number includes both reconstruction efficiency and acceptance. For the Monte Carlo simulation, assumptions on the mass of the charm quark, the fragmentation functions, the proton structure functions and, for the resolved part, the photon structure functions have to be made.

The Monte Carlo simulations used here assume a charm mass of 1.5 GeV. For the direct process the MRS-H parametrisation for the proton structure function is used. The GRV-G-HO parametrisation is taken to describe the photon structure function. Both parametrisations are well suited to describe HERA results in deep inelastic scattering and describe as well the rise of the gluon density for small x_g . For the visible range, $\epsilon \cdot A$ was estimated to be 0.48 using the direct and 0.58 using the resolved Monte Carlo. So according to eq. 3.3

$$(\epsilon \cdot A)_{rec} = 0.50$$

for the visible range. The extrapolation factor from the visible range to the complete range in η and p_t of the D^* has been calculated to be

$$EF = 5.8.$$

systematic uncertainties for $\sigma_{\gamma p}$	
<i>syst</i> ₁	
Trigger elements of ST84	5.8 %
Luminosity	1.1 %
ET44 acceptance and efficiency	6 %
signal width	9 %
total:	12.3 %
<i>syst</i> ₂	
Track reconstruction	$\pm_{0}^{9\%}$
$c \rightarrow D^* \rightarrow K\pi\pi$ total decay fraction	7 %
total:	$\pm_{7}^{11.4\%}$
D^*, D^0 branching ratio	4 %
theoretical uncertainties	
charm mass	30 %
proton structure function	15 %
total:	33.5 %

Table 3.1: *Compilation of systematic errors contributing to $\sigma_{\gamma p}$.*

3.4 Systematic Errors

Table 3.1 shows the systematic errors which contributed to the measurement of the visible ep cross section and the calculation of the total γp cross section. The systematic errors are subdivided into those common to the analysis using the ET33 and the one using the ET44 (*syst*₂), and those who contribute only to this analysis (*syst*₁).

Common systematic errors include:

- Track reconstruction
- Branching ratio and fragmentation
- Theoretical error: Proton structure function, charm quark mass and uncertainties in parton densities.

The theoretical error was obtained by calculating the acceptance using different proton structure functions [17]. The error on the measurement of the D^*/D^0 branching ratio is only included in the error on the result of σ_{ep}^{vis} , whereas for the calculation of $\sigma_{\gamma p}$ the error on the total decay fraction is used.

3.5 Results

Using eq. 3.1 the visible ep-cross section is

$$\sigma_{vis}(ep \rightarrow D^*X) = (30.55 \pm 5.46_{stat} \pm_{3.96}^{4.82}_{syst}) nb$$

for: $p_t(D^*) > 1.8 GeV$

$$|\eta(D^*)| < 1.5$$

$$Q^2 < 0.009 GeV^2$$

$$0.04 < y < 0.24, \text{ which corresponds to: } 60 GeV < W_{\gamma p} < 147 GeV.$$

According to formula 3.5 the total γp cross section can be calculated to:

$$\sigma_{\gamma p \rightarrow c\bar{c}} = (6.42 \pm 1.15_{stat} \pm 0.79_{syst,1} \pm_{0.45}^{0.73}_{syst,2} \pm 2.15_{theor}) \mu b$$

for: $0.04 < y < 0.24 \Rightarrow \bar{y} = 0.1 \Rightarrow \bar{W} = 95 GeV$, and $Q^2 < 0.009 GeV^2$

Here *stat*, *syst*₁ (systematic errors only contributing to this analysis) and *syst*₂ (systematic errors common to this analysis and the analysis using the ET 33) denote statistical and systematic errors, respectively, and *theor* shows the error resulting from theoretical uncertainties. This result is in good agreement with a result, where the γp -cross section is calculated at a γp center of mass energy of 200 GeV [40] (see fig.3.3). The other points in this figure include results from H1 and ZEUS using untagged data at high center of mass energies, and results from several fixed target experiments at low γp -center of mass energies. The measurements agree well with theoretical NLO perturbative calculations, using MRS-G [41] or MRS-H [38] for the proton structure function and GRV-G-HO [26] for the photon structure function. However, due to the large errors the measurements are not sensitive enough to rule out different underlying gluon densities.

For the lower and upper curve, the renormalisation scale was varied between $\mu_R = m_c/2$ and $\mu_R = 2m_c$. The calculations suggest, that a smaller scale, which implies a smaller charm mass in the calculation, seems more appropriate. This leads to the suggestion, that the charm is not as 'massive' as expected.

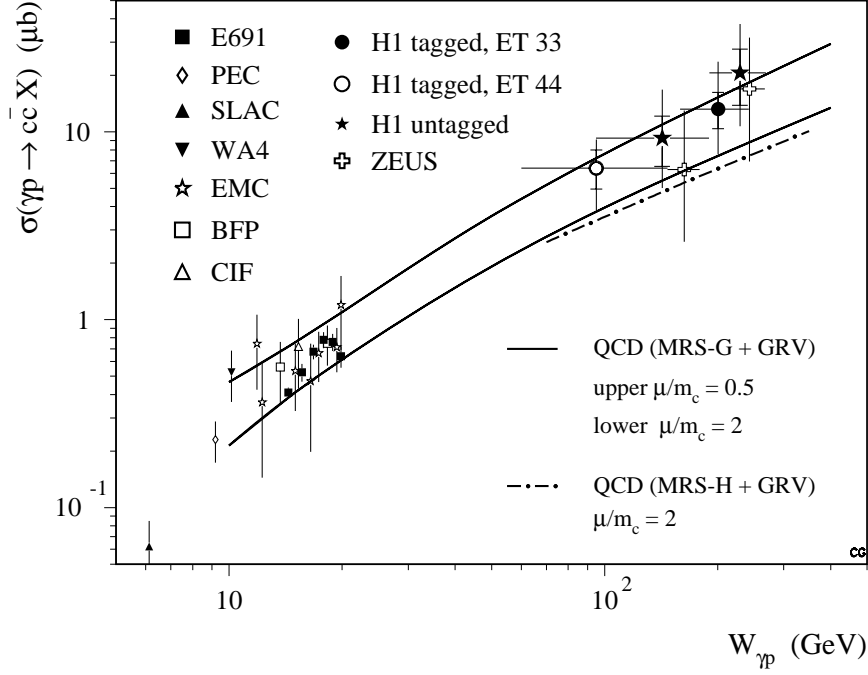


Figure 3.3: The total γp cross section as a function of W . Shown are results from H1 and ZEUS in the high W region and results from fixed target experiments covering the low W range.

3.6 Differential cross sections in $p_t(D^*)$ and $\eta(D^*)$

The differential cross sections are obtained for the visible range. Thus uncertainties in extrapolation due to different models are excluded. The efficiencies are determined bin by bin, separately for the p_t and the η distributions. In the visible range, the hadronic contribution to the cross sections is of the order of less than 10 %. The reason are cuts in p_t and η of the D^* particles. Therefore, for the calculation of the reconstruction efficiency, only the direct component is taken into account.

The Δm distributions in different bins of p_t are shown in fig. 3.5. The differential cross section in p_t is calculated according to eq. 3.8 for 3 different bins in p_t . The results are shown in table 3.2 and contain statistical errors and systematical errors. Not included are theoretical errors.

$$\left. \frac{d\sigma^{vis}}{dp_t}(\gamma p \rightarrow c\bar{c}X) \right|_{-1.5 < \eta < 1.5; p_1 < p_t < p_2} = \frac{N(D^* \rightarrow K\pi\pi)_{p_1 < p_t < p_2}}{2 \cdot B_{DF}(c \rightarrow K\pi\pi) \cdot Fl \cdot L_{cor} \cdot (\epsilon A)_{\text{tag44}} \cdot (\epsilon A)_{\text{rec}} \cdot \Delta p_t} \quad (3.8)$$

$p_t(D^*)[\text{GeV}]$	$N_{rec.,vis range}^{D^*}$	$(\epsilon A)_{rec}$	$\frac{d\sigma}{dp_t}[\mu\text{b}/\text{GeV}c]$
$1.8 < p_t < 2.5$	33.6 ± 8.4	0.435 ± 0.038	$1.09 \pm 0.273_{stat} \pm 0.179_{syst}$ 0.152_{syst}
$2.5 < p_t < 3.5$	9.6 ± 4.8	0.561 ± 0.059	$0.169 \pm 0.085_{stat} \pm 0.029_{syst}$ 0.026_{syst}
$3.5 < p_t < 6.0$	10.6 ± 3.7	0.695 ± 0.1	$0.06 \pm 0.021_{stat} \pm 0.011_{syst}$ 0.012_{syst}

Table 3.2: Results on the differential cross sections in p_t . The results are given with statistical errors and all systematical errors. Not included are errors due to theoretical uncertainties.

in eq. 3.8, Fl denotes the photon flux, L_{cor} the corrected luminosity according to eq. 3.2 and Δp_t the width of the interval in p_t . The reconstruction efficiency has been calculated for the visible range using Monte Carlo simulation, the error on the efficiency includes the statistical error. For the systematical errors, the errors on reconstruction efficiency (bin dependent), trigger efficiency, luminosity, ET 44 acceptance, track reconstruction and decay fraction have been added in quadrature. Results of the calculation are given in table 3.2. Fig3.4 shows the resulting

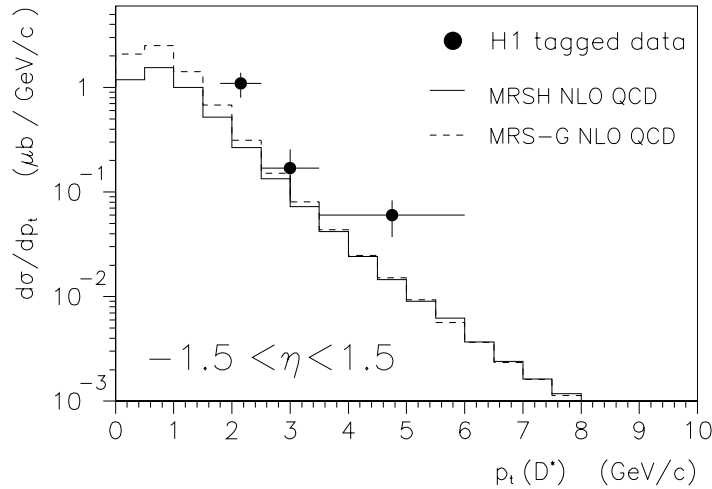


Figure 3.4: Distribution of the transverse momentum of the D^* -mesons from photoproduction events. Shown is the visible differential cross section $d\sigma^{vis}(\gamma p \rightarrow c\bar{c}X)/dp_t$ for $-1.5 < \eta < 1.5$ and $0.04 < y < 0.24$ in bins of p_t . The results are given with statistical errors and those systematical errors which depend on p_t . Not included are $\pm 14.2/10.9\%$ common systematical errors and errors due to theoretical uncertainties. The solid histogram shows the NLO QCD prediction [21], using the MRS-H proton parton density parametrisation (MRS-G : dotted histogram line) with a charm mass of 1.5 GeV , calculated at $W_{\gamma p} = 95 \text{ GeV}$.

differential cross sections in p_t together with two NLO QCD calculations [21], where the MRS-H and the MRS-G parametrisation for the proton structure were used. The data are described reasonably well by the NLO QCD calculation although the data points are higher than the theoretical values, given the uncertainty in the normalisation of the theoretical calculations.

A similar effect was observed in [40]. The two results can not be overlaid directly, since they use different ranges in Q^2 and W and different cuts in η and p_t to define the visible range.

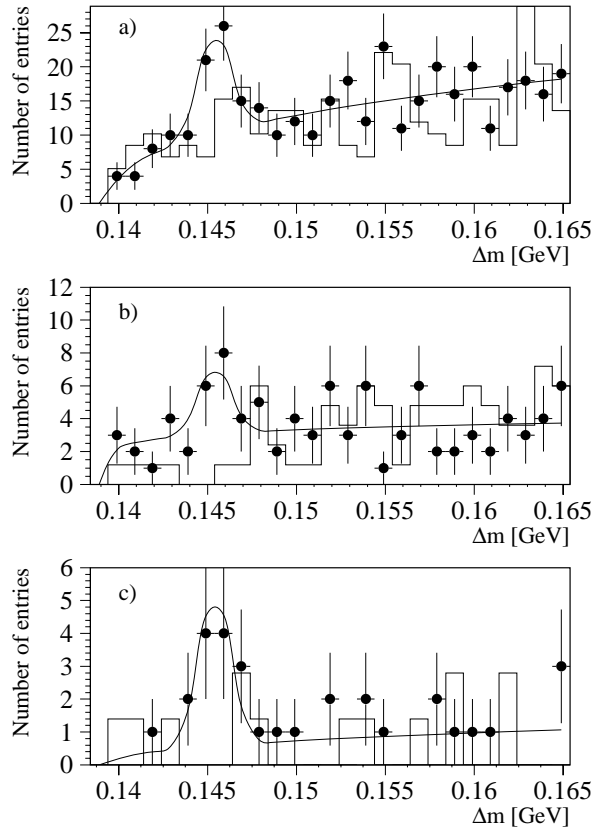


Figure 3.5: Δm distributions for different bins in p_t . The points show the data, the histogram shows the wrong sign combinatorial background. The fit (solid line) was obtained the same way as for the total Δm distribution, with a fixed width of 0.9 MeV. The statistical errors include the error due to variations in the width of the Δm distribution. Fig. a) to c) show the distributions for the three different bins: a) $1.8 < p_t < 2.5$, b) $2.5 < p_t < 3.5$, c) $3.5 < p_t < 6.0$ GeV.

According to the same procedure, the differential cross sections are calculated in bins of η . Fig. 3.6 shows the differential cross section $d\sigma^{vis}(\gamma p \rightarrow c\bar{c}X)/d\eta$ for $p_t > 1.8$ GeV and $0.04 < y < 0.24$. The lines represent NLO QCD calculations [21], using two different parametrisations for the proton structure function. Whereas the shape of the measurement is consistent with the calculated differential cross sections, there is a shift of the data points towards higher values. However, if all systematical

errors are included ($\pm_{10.9}^{14.2}\%$ common systematical errors), the data points describe the predictions within their errors. The slight shift can be explained by an overall normalisation of the theoretical calculations. By comparing this results with the

$\eta(D^*)$	$N_{rec.,vis}^{D^*}$	$(\epsilon A)_{rec}$	$\frac{d\sigma}{d\eta} [\mu b]$
$1.5 > \eta > 1.0$	7 ± 3.9	0.51 ± 0.076	$0.271 \pm 0.151_{stat} \pm_{0.05}^{0.055}_{syst}$
$1.0 > \eta > 0.5$	19 ± 4.5	0.58 ± 0.074	$0.648 \pm 0.153_{stat} \pm_{0.109}^{0.121}_{syst}$
$0.5 > \eta > 0.0$	20 ± 5.8	0.61 ± 0.077	$0.648 \pm 0.188_{stat} \pm_{0.108}^{0.122}_{syst}$
$0.0 > \eta > -0.5$	6.0 ± 4.1	0.62 ± 0.077	$0.191 \pm 0.131_{stat} \pm_{0.032}^{0.036}_{syst}$

Table 3.3: Results on the differential cross sections in η . The results are given with statistical errors and all systematical errors. Not included are errors due to theoretical uncertainties.

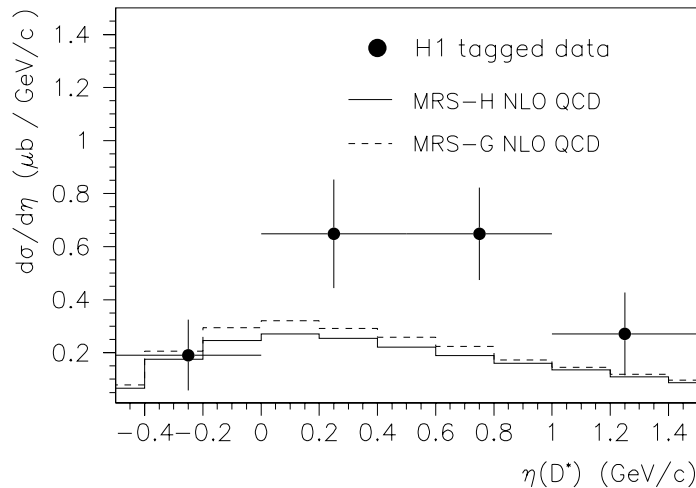


Figure 3.6: η distribution of the D^* -mesons from photoproduction events. Shown is the visible differential cross section $d\sigma(\gamma p \rightarrow c\bar{c}X)/d\eta$ for $p_t > 1.8 \text{ GeV}$ and $0.04 < y < 0.24$. The error bars show the statistical errors and those systematical errors which depend on η . Not included are $\pm_{10.9}^{14.2}\%$ common systematical errors and errors due to theoretical uncertainties. The solid histogram shows the NLO QCD prediction, using the MRS-H proton parton density parametrisation (MRS-G : dotted histogram line) with a charm mass of 1.5 GeV , calculated at $W_{\gamma p} = 95 \text{ GeV}$.

differential cross sections published in [40] one has to take into account the different ranges in Q^2 and y and the different cuts in $p_t(D^*)$. If the cross sections in fig. 3.6 are scaled by the ratio of the integral of the total γp -cross section in the range

$1.8 < p_t < 2.5$ to $\sigma_{\gamma p}$ for the total range, both measurements are in agreement with each other within the experimental errors. The experimental errors are dominated by the low number of D^* candidates. A more exact measurement can be expected using additional data from 1996 and 1997 and thus increased statistics.

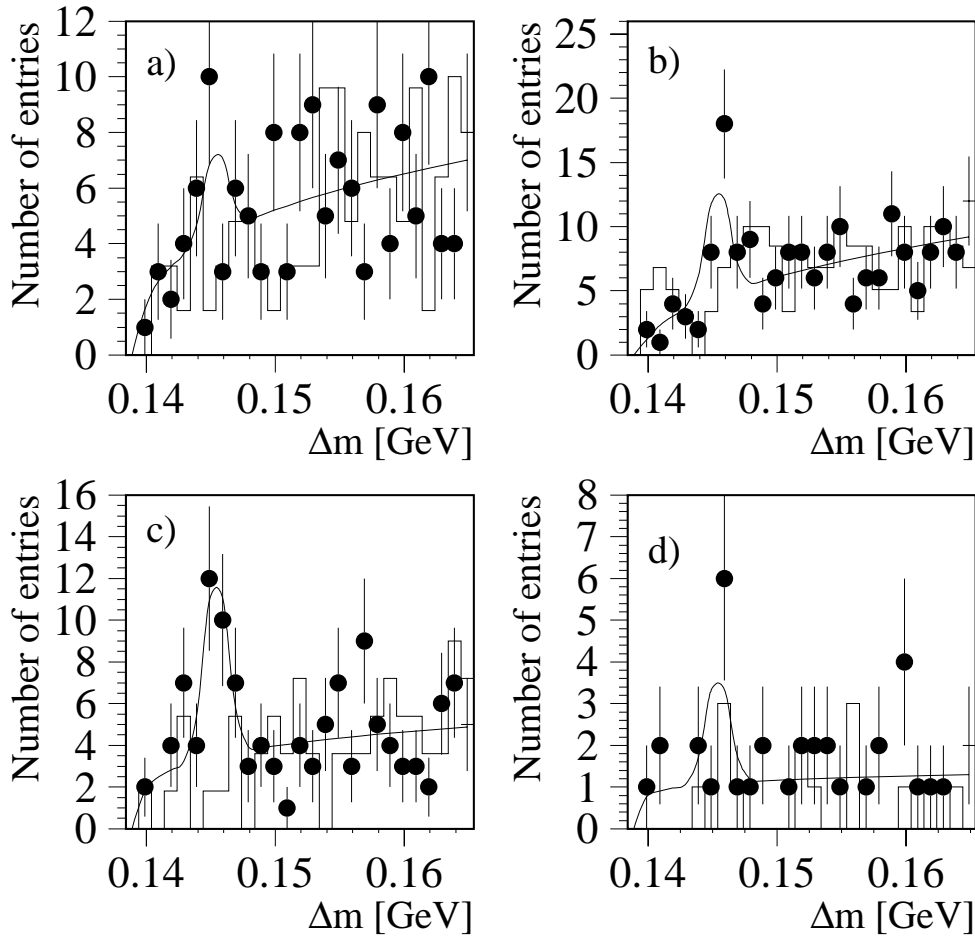


Figure 3.7: Δm distributions for different bins in η . The points show the data, the histogram shows the wrong sign combinatorial background. The fit (solid line) was obtained the same way as for the total Δm distribution. The statistical errors include the error due to variations in the width of the Δm distribution. Fig. a) to d) show the distributions for the four different bins: a: $1.5 > \eta > 1.0$, b: $1.0 > \eta > 0.5$, c: $0.5 > \eta > 0.0$, d: $0.0 > \eta > -0.5$.

3.7 The W Dependence of the γp -Cross Section

For photoproduction processes, where $Q^2 \approx 0$, $W^2 = y \cdot s$. Motivated by eq. 1.8, the W dependence at high W^2 of the γp -cross section into $c\bar{c}$ is parametrized as

$$\sigma_{\gamma p}(y) = \sigma_0 \cdot W^{2\lambda} = \sigma_0 \cdot \left(\frac{s}{s_0}\right)^\lambda \cdot y^\lambda. \quad (3.9)$$

To determine the slope parameter λ , a χ^2 minimisation is used. The ep -cross section is measured and the expectation value, the integral $F(\sigma_0, \lambda)$, is calculated for different values of the normalisation factor σ_0 and the slope parameter λ .

$$\sigma_{ep}^{\prime \text{measured}}(D^* \rightarrow K\pi\pi) = \frac{N_{rec}^{D^*}}{\epsilon \cdot L \cdot B_r} = F(\sigma_0, \lambda) = \int Fl_{\gamma/\epsilon}(y) \cdot A(y) \cdot \sigma_0 \cdot W^{2\lambda} \cdot dy \quad (3.10)$$

Here ϵ only includes the non y dependent part of the total efficiency. The y dependent efficiency and acceptance is included in the integral $F(\sigma_0, \lambda)$. Let

$$x_i - F_i(\sigma_0, \lambda) = \sigma_{ep}^i - \sigma_0 \cdot \left(\frac{s}{s_0}\right)^\lambda \cdot \int_{y_i^l}^{y_i^h} Fl_{\gamma/\epsilon}(y) \cdot A^i(y) \cdot y^\lambda \cdot dy, \quad (3.11)$$

where $s_0 = 1 \text{ GeV}^2$, $i = 1$ (ET33), 2 (ET44), 3 (untagged sample 1 (UT1)), 4 (untagged sample 2 (UT2)), and $Fl_{\gamma/\epsilon}(y)$ denotes the photon flux according to the WWA and the $A^i(y)$ are the acceptance functions for the different ranges in y (see table 3.4).

The function to be minimized, $\chi^2(\sigma_0, \lambda)$, is then given as

$$\chi^2(\sigma_0, \lambda) = (\mathbf{x} - \mathbf{F}(\sigma_0, \lambda))^T \mathbf{M} (\mathbf{x} - \mathbf{F}(\sigma_0, \lambda)). \quad (3.12)$$

Here, \mathbf{M} denotes the inverse of the covariance matrix. The covariance matrix contains the statistical errors, squared, in the diagonal elements and the errors due to correlation between measured quantities in the off-diagonals:

$$\mathbf{M} = \begin{pmatrix} \sigma_{ET44}^2 & 0 & 0 & 0 \\ 0 & \sigma_{ET33}^2 & cov(ET33, UT1) & cov(ET33, UT2) \\ 0 & cov(ET33, UT1) & \sigma_{UT1}^2 & 0 \\ 0 & cov(ET33, UT2) & 0 & \sigma_{UT2}^2 \end{pmatrix}^{-1}$$

$$\Rightarrow \mathbf{M} = \begin{pmatrix} 0.5^2 & 0 & 0 & 0 \\ 0 & 0.46^2 & 0.016 & 0.0301 \\ 0 & 0.016 & 0.512^2 & 0 \\ 0 & 0.0301 & 0 & 1.15^2 \end{pmatrix}^{-1}.$$

An overlap of $N_{cor} = 11$ events between ET 33 and UT 1 and between ET 33 and UT 2 has been taken care of by calculating the correlation. The covariance elements have been calculated according to:

$$cov(ET33, UT 1/2) = \frac{N_{cor}}{L_{ET33}\epsilon_{ET33}Br} \cdot \frac{N_{cor}}{L_{UT1/2}\epsilon_{UT1/2}Br} \cdot \frac{\Delta N_{cor}^2}{N_{cor}^2}.$$

For the minimisation, only statistical errors are included. The reason is that all systematical errors except the error in the acceptance are 100 % correlated with each other. To estimate the impact of the error of the acceptances on the result on χ^2 , the σ_{ep}^i are varied 1 σ standard deviation of the systematical error of the acceptance up or down, respectively. The resulting difference in λ in the minimum of χ^2 is less than 6.5 %. This error has been added in quadrature to the error in λ obtained from minimisation.

Quantity	ET 44	ET 33	UT 1	UT 2
Range in y	$0.04 < y < 0.24$	$0.28 < y < 0.65$	$0.1 < y < 0.4$	$0.4 < y < 0.8$
Range in Q^2 [GeV^2]	< 0.006	< 0.01	< 4	< 4
$N_{rec}^{D^*}$	21 ± 8	119 ± 16	46 ± 9	51 ± 12
ϵ , not y dependent	0.5	0.48	0.52	0.31
Luminosity [pb^{-1}]	1.223	2.77	1.29	1.29
mean Acceptance	0.1144	0.6	0.21	0.56
Photon flux	0.0509	0.0141	0.0486	0.0155
σ_{ep} [nb]	1.31 ± 0.5	3.42 ± 0.46	2.62 ± 0.51	4.87 ± 1.15

Table 3.4: *Compilation of data necessary to calculate the visible ep and γp cross sections. The efficiency given in the table includes the trigger efficiency in the case of ET 33. For ET 44 the trigger efficiency is included in the number given for the luminosity. The numbers for $N_{rec}^{D^*}$ have been obtained for the visible range: $-1.5 < \eta < 1.0$ and $p_t(D^*) > 2.5 GeV$, and are not corrected for the acceptances of the electron taggers. The values for acceptance and photon flux given are average values.*

Because the visible ep -cross section for the ET 44 was calculated using a different range in p_t and η , the analysis for the ET 44 is done a second time, using cuts identical to the ones used for the calculation of the visible ep -cross section in the range $0.28 < y < 0.65$ for the ET 33. Table 3.4 gives a compilation of the various numbers necessary to calculate σ_{ep} and $\sigma_{\gamma p}$ for all four H1 data points.

The result of the χ^2 minimisation is shown in fig. 3.8. Each curve represents a calculation of χ^2 done for a different value of σ_0 over a range of λ of $0.0 < \lambda < 1.0$. The minimum in χ^2 is clearly visible at $\lambda = 0.61$.

The one sigma standard deviation values on σ_0 and λ are obtained by adding one unit to the minimum χ^2 , as illustrated in fig. 3.9. A detailed calculation gives

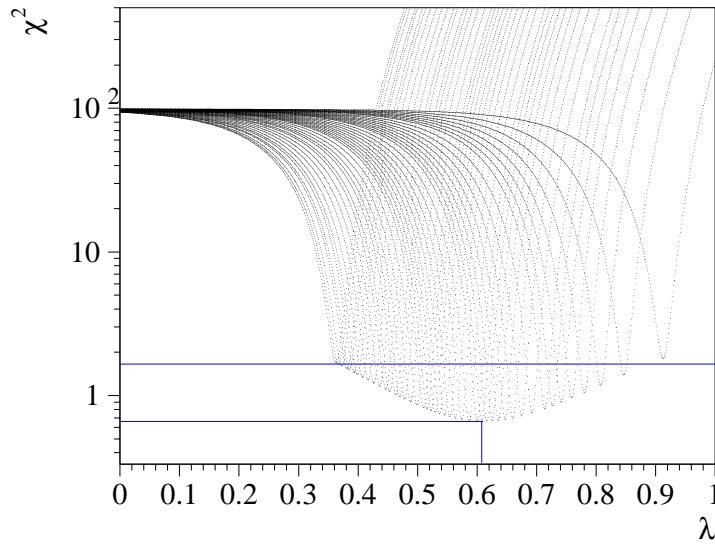


Figure 3.8: χ^2 , as given in eq. 3.12, calculated for different slope parameters λ . Each curve is calculated with one fixed value for the normalisation parameter σ_0 . For visibility reasons, not all calculated curves have been included in this plot.

as results on σ_0 and λ

$$\lambda = 0.61 \pm_{0.24}^{0.28} \quad \text{and} \quad \sigma_0 = (0.65 \pm_{0.615}^{7.05}) \text{ nb.}$$

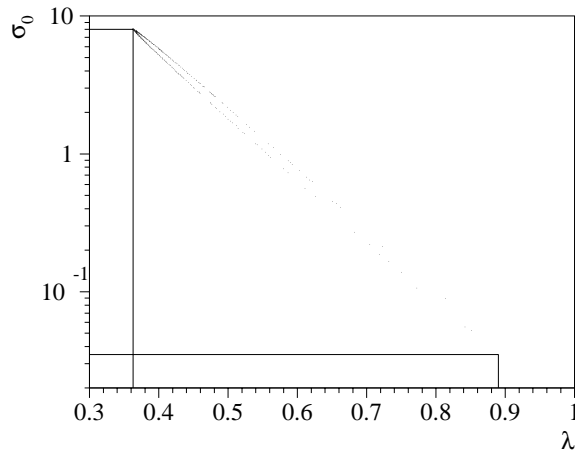


Figure 3.9: Covariance ellipse for σ_0 and λ as obtained from fig. 3.8. A calculated point enters this histogram, if $1.6 < \chi^2 < 1.72$.

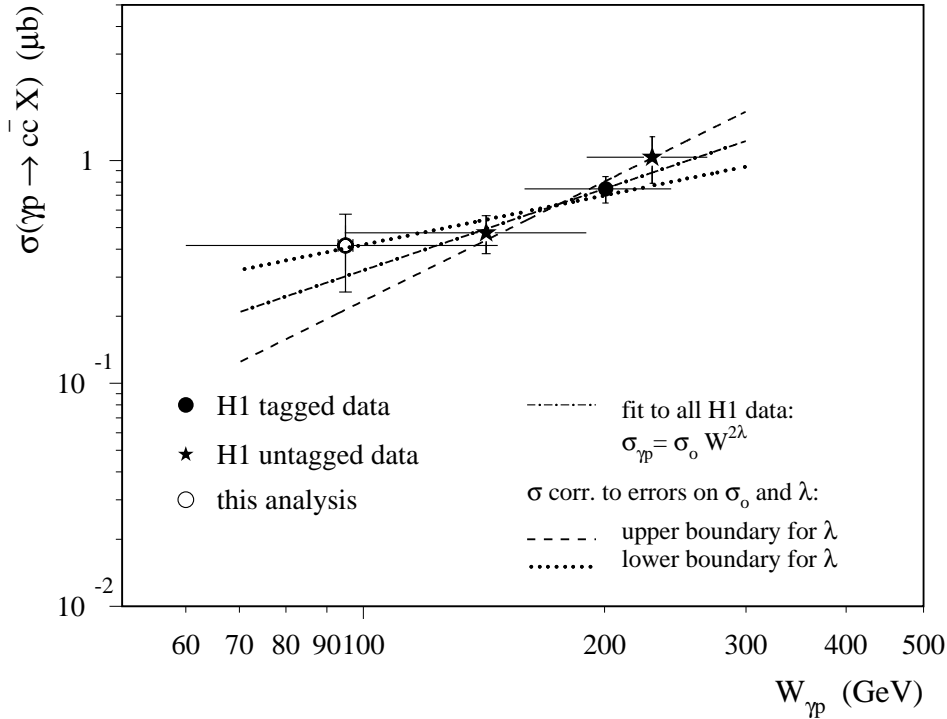


Figure 3.10: *H1* measurements of $\sigma_{\gamma p}$, together with the fit as calculated in this analysis. The data points show $\sigma_{\gamma p}(\gamma p \rightarrow c\bar{c})$ for $-1.5 < \eta < 1.0$ and $p_t > 2.5 \text{ GeV}$

Fig. 3.10 shows the visible γp -cross sections of the measurements which were used to obtain the fit result. The result on the fit is shown as well, together with the two curves which result from a 1σ deviation of the measured parameters σ_0 and λ .

The result on λ obtained in this analysis can now be compared to different measurements of λ for various processes. Fig. 3.11 shows λ as a function of the hard scattering scale μ as calculated in chapter 1.3, measured for different processes at H1. As discussed in chapter 1.3, for the total photoproduction cross section, where the final state is characterized by light mesons with low transverse momentum, λ is measured to be $\lambda = 0.08$ [42], in agreement with the fit to all total hadron-hadron cross sections.

The elastic production of ρ mesons [43], where $\frac{d\sigma}{dt} = W^{4\lambda}$ at high W^2 , has been measured for different Q^2 . Due to the low mass of the ρ and its low p_t , Q^2 serves here as the hard scale of the process, and for low Q^2 λ reaches the same soft limit of 0.08.

The same applies to the measurement of the cross section in deep inelastic scattering [44] [45]. Here $\sigma \sim x^{-\lambda}$ has been fitted, and thus for fixed $Q^2 = xys$ and at low x , $\sigma \sim W^{2\lambda}$.

To explain the measurement of the slope of the elastic J/ψ in photoproduction [46], two different approaches have been made:

Donnachie and Landshoff use a Regge theory based model to describe the underlying process as a soft pomeron exchange. Although the model has been successfully used to describe the production of light vector mesons, the prediction in this case, $4\lambda = 0.32$ gives a too shallow rise of the cross section with W .

This gives rise to the assumption, that due to its high mass, the J/ψ can be treated perturbatively, with $\mu = 2m_c$ as the hard scale.

For the inelastic measurement of J/ψ [47], the decision which scale to take is not as clear cut: To obtain λ , a cut on $p_t(J/\psi) > 1.0 \text{ GeV}$ has been used, so the mean value for \bar{p}_t^2 is calculated to be 3.6 GeV^2 . However, since this is the mean transverse momentum of the J/ψ , and $p_{tc} = 0.5p_{tJ/\psi}$, the scale μ^2 yields $\mu^2 = 4m_c^2 + p_{tc}^2 = 12.6 \text{ GeV}^2$. In [48] the scale dependence of the evolution

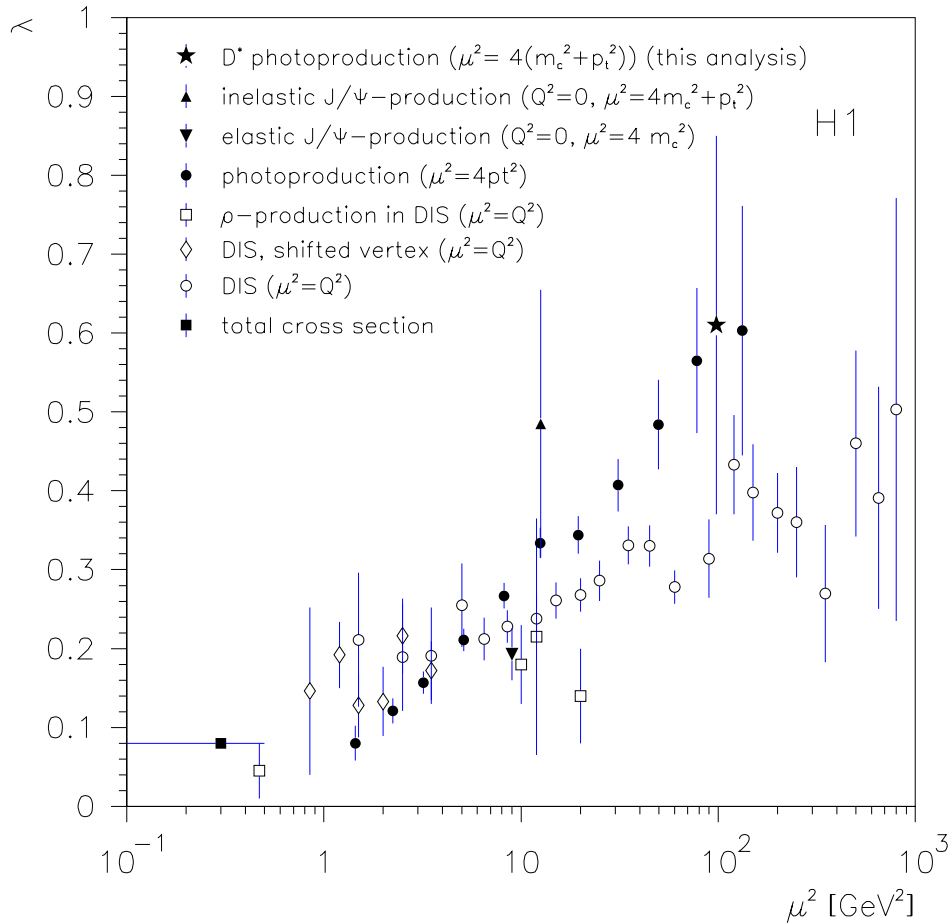


Figure 3.11: Slope parameter λ of the energy dependence $\sigma_{tot} \sim W^{2\lambda}$ or $\frac{d\sigma}{dt}(\text{elastic}) \sim W^{4\lambda}$ for different types of processes.

of photoproduction cross sections is studied. Since the final state is dominated by light mesons, the largest transverse momentum of a charged particle in the photon fragmentation region is used to define the hard scale of the process, namely

$$\mu^2 = 4p_{t\max}^2.$$

In D^* photoproduction, due to the choice of the analysis cuts, the momentum of the D^* is of the same order of magnitude as the mass of the c quark. Therefore, as mentioned in chapter 1.3, $\mu = 2 \cdot \sqrt{m_c^2 + p_t(c)^2}$ is the hard scale of the process. With a mean $p_t(D^*)$ of 3.3 GeV and the approximation that $p_t(D^*) \approx 0.7 \cdot p_t(c)$, $\mu^2 = 98 \text{ GeV}^2$.

However, it should be noted that in [48] the p_t of the final state is taken, since different photoproduction processes are included in the analysis, in contrast to this analysis.

Common to all the processes is a strong dependence of λ on the scale of the process. This is the case as well for photoproduction processes with $Q^2 = 0$ as well as for processes in DIS.

3.8 Summary

The photoproduction of D^* in the process of boson gluon fusion has been investigated at a γp center of mass energy of 95 GeV. The data used have been accumulated in 1995 with the H1 detector at HERA. As event selection criteria tracks in the central tracking detectors and a positive signal from the electron tagger at $-z = 44$ m are required.

The total data sample corresponds to an integrated corrected luminosity of 1.2 pb^{-1} . In the kinematical range of $p_t(D^*) > 1.8 \text{ GeV}$ and $-1.5 < \eta(D^*) < 1.5$, 56 ± 10 D^* candidates have been found.

The ep cross section for this visible range has been measured to be

$$\sigma_{vis}(ep \rightarrow D^* X) = (30.55 \pm 5.46_{stat} \pm 4.82_{3.96_{syst}}) \text{ nb}.$$

For the total kinematical range, the γp cross section has been calculated to be

$$\sigma_{\gamma p \rightarrow c\bar{c}} = (6.42 \pm 1.15_{stat} \pm 0.79_{syst,1} \pm 0.73_{0.45_{syst,2}} \pm 2.15_{theor}) \mu\text{b}.$$

This cross section can be reproduced by NLO perturbative QCD calculations. However, due to the interplay between large uncertainties in the choice of charm mass and different choices in the parametrisation of the parton densities in the proton prevent a conclusion, which parton density parametrisation is favoured.

The differential cross sections in $d\sigma/d\eta$ and $d\sigma/dp_t$ have been measured and have been found to agree with NLO QCD calculations within errors. However, in both cases the measurements are almost 1σ higher than the expectations. Two possible explanations are:

1. the possibility of a mere fluctuation due to very low statistics.
2. a possible rise of the resolved photon contribution towards higher values of η which is underestimated by the current calculations.

Using in total four measurements of $\sigma_{vis}(ep \rightarrow D^* X)$ for different ranges in y , under the assumption of a W dependence of the photoproduction cross section of the form $\sigma = \sigma_0 W^{2\lambda}$,

$$\lambda = 0.61 \pm 0.28_{0.24}$$

has been calculated. A comparison between the slope parameter λ as measured for different processes shows an universal dependence of λ on the scale which is used in the process. $\lambda = \lambda(\mu^2)$ is independent with regard to the actual scale used (p_t, Q^2 or mass). Furthermore, there is an indication, that the transition between 'soft' and 'hard' physics is smooth.

Chapter 4

The Central Silicon Tracker

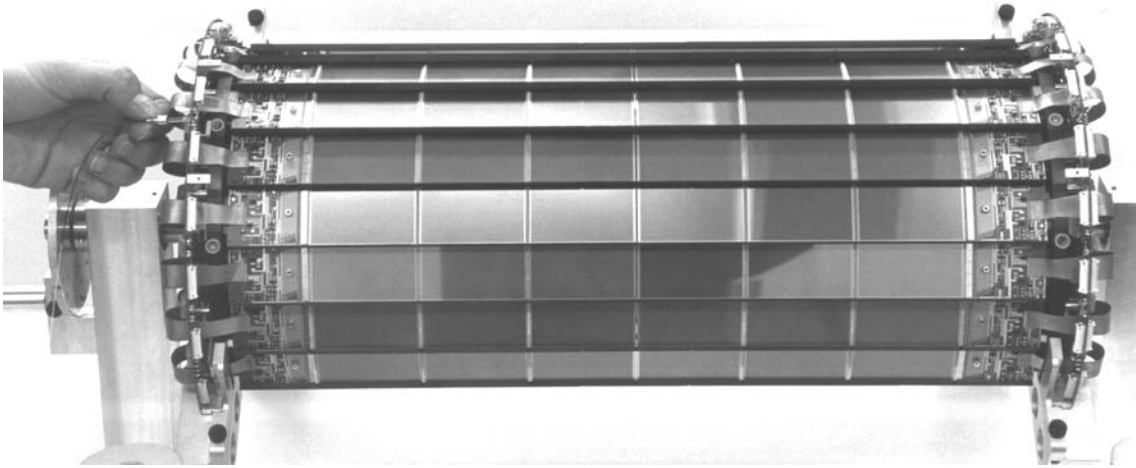


Figure 4.1: *Photo of the lower half of the Central Silicon Tracker.*

A proposal to build a Central Silicon Tracker (CST) was submitted in 1992 [11]. Its task is to measure interaction and decay vertices with very high precision. This is of great advantage in the analysis of events with heavy quark decays: The main improvement in charm physics of having a vertex detector will be a better signal to noise ratio in the D^* signal, which allows to relax some analysis cuts. Table 4.1 shows various reconstruction efficiencies for D^0 mesons in photoproduction calculated with and without a vertex detector [51]. A precise identification of the secondary vertex of the charm decay would suppress backgrounds considerably. Because of the short lifetime of charmed particles ($c\tau \approx 124 \mu\text{m}$ for D^0 , $317 \mu\text{m}$ for D^\pm), the vertex resolution needs to be in the order of $50 - 100 \mu\text{m}$.

For a two layer vertex detector, the vertex can be determined by using the curvature of the tracks as measured by the outer tracking chambers and the precise track hits from the CST.

To obtain a high vertex reconstruction efficiency by covering as many decay modes as possible, three dimensional hit information from the vertex detector is advantageous.

no vertex detector	acceptance $p_T > 2.5$ GeV	reconstr. efficiency	$c \rightarrow D^* \rightarrow D^0 \pi$	D^0 decay mode	total efficiency
$D^0 \rightarrow K^- \pi^+$	0.03	0.5	0.18	0.038	$1 \cdot 10^{-4}$
$D^0 \rightarrow K^- \pi^+ \pi^+ \pi^-$				0.075	
$D^0 \rightarrow K^- \mu^+ \nu$				0.032	
$D^0 \rightarrow K^0 \pi^+ \pi^- \rightarrow 4\pi$				0.019	
sum (D^0)	0.03	0.5	0.18	0.164	$4 \cdot 10^{-4}$
with vertex detector	acceptance $p_T > 1.0$ GeV $d/\sigma > 2.3$	reconstr. efficiency	$c \rightarrow D^0/D^+$	D^0/D^+ decay mode	total efficiency
$D^0 \rightarrow K^- \pi^+$	0.05	0.3	0.55	0.038	$3 \cdot 10^{-4}$
$D^0 \rightarrow K^- \pi^+ \pi^+ \pi^-$				0.075	
$D^0 \rightarrow K^- \mu^+ \nu$				0.032	
$D^0 \rightarrow K^0 \pi^+ \pi^- \rightarrow 4\pi$				0.019	
sum (D^0)	0.05	0.3	0.55	0.164	$1 \cdot 10^{-3}$
$D^+ \rightarrow K^0 \pi^+ \rightarrow 3\pi$	0.05	0.3	0.21	0.019	$6 \cdot 10^{-5}$
$D^+ \rightarrow K^- \pi^+ \pi^+$				0.091	
$D^+ \rightarrow K^0 \pi^+ \pi^+ \pi^- \rightarrow 5\pi$				0.024	
sum (D^\pm)	0.05	0.3	0.21	0.134	$4 \cdot 10^{-4}$
sum (all D -mesons)					$2 \cdot 10^{-3}$

Table 4.1: Summary of various reconstruction efficiencies for D^0 mesons in photoproduction with and without a vertex detector [51]. Charged particles have been confined to $|\eta| < 1.5$, and a vertex separation of $d/\sigma > 2.3$ has been required in the case of a vertex detector. Acceptance and reconstruction efficiencies depend on details of the analysis and only round numbers are given.

For cylindrically arranged detector layers, both the azimuthal ($r\phi$) as well as the longitudinal (z) coordinates have to be measured.

The CST and the beam pipe should have as little material as possible and therefore a small interaction length in order not to disturb too much the track measurement by multiple scattering. An example is given in fig. 4.2. Here the transverse impact parameter resolution is shown for three different scenarios.

Thin silicon wafers with a large number of implanted, strip-shaped segmentations in both $R\phi$ and z coordinate (see chapter 4.1), having all their individual read-out outside the active region (see chapter 4.3 + 4.4), are the best choice for a vertex detector. Six rectangular wafers (detectors) are placed in a row forming 'ladders', which in turn are arranged to make up cylindrical layers (see fig.4.1 and chapter 4.2).

Three detectors and a ceramic hybrid supporting the read-out electronics form a submodule, called half ladder (see fig.4.7). The read-out electronics is placed at the end of the modules in order to minimize the amount of material between the CST and the tracking chambers. All signals, digital control sequences as well as analog hit signals, are transmitted through optical fibers [52]. The read-out electronics is controlled by a special ASIC chip (see chapter 4.5) having only four input lines. Since the trigger decision time exceeds the time between bunch crossings, it becomes necessary to store data at the front end. This is done by an ASIC Analog Pipeline

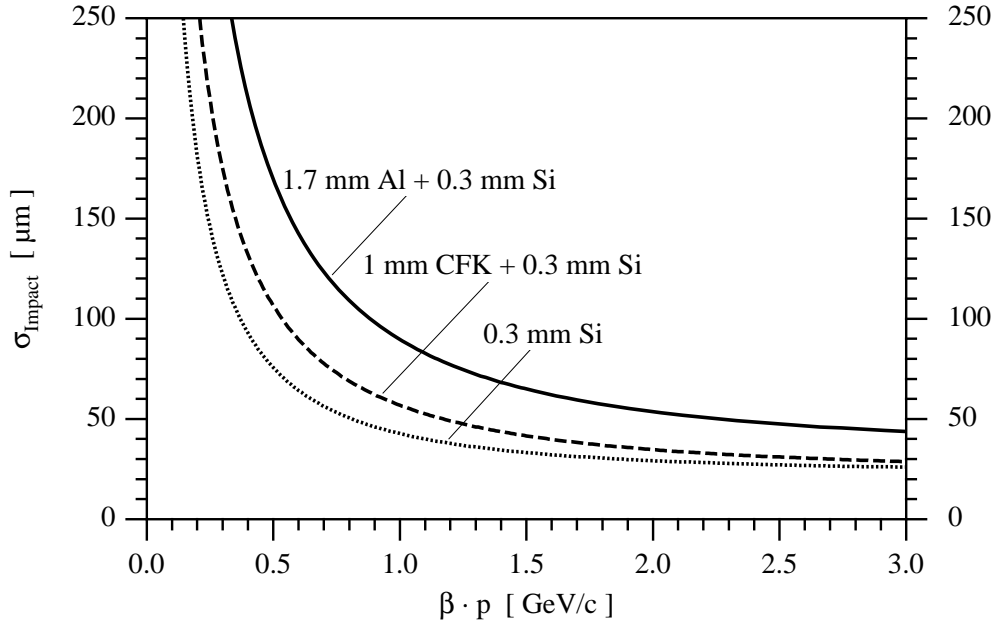


Figure 4.2: *Transverse impact parameter resolution of tracks extrapolated from the CST to the common event vertex as a function of material placed between the interaction vertex and the second layer of silicon detectors. For this calculation an intrinsic resolution of the CST detectors of $10 \mu\text{m}$ is assumed. The solid line refers to the beam pipe in 1995, which consisted of 2 mm thick aluminium and will be replaced by a 1 mm thick Carbon Fiber Composit beam pipe with a $100 \mu\text{m}$ thin aluminium layer (dashed line). The dotted line refers to no beam pipe at all, just the first layer of silicon detectors, which is situated at a radius of 57.5 mm .*

Chip (APC) with a storage depth of 32 buffers (see explanations in chapter 4.4, [59], and ref. [53] for the discussion of a 12 channel prototype).

In the following chapter a description of the CST detector is given. First, the principles of a silicon detector are explained, then the detector design and its implication on the performance is discussed.

In the next section, the mechanical construction of the detector is portrayed, starting from the assembly of single detectors into modules. Following this, an explanation of the read out concept is given, with the analog side as well as digital side of the silicon detector read-out described in detail.

4.1 Detectors

Fig.4.3 shows the basic layout of a double-sided silicon semiconductor detector: The bulk material consists of n-type silicon. On one side of the detector (referred to as the p-side) there are p^+ strip implants and on the other side (the n-side) the strip implants consist of n^+ type silicon. When applying a voltage between p-side

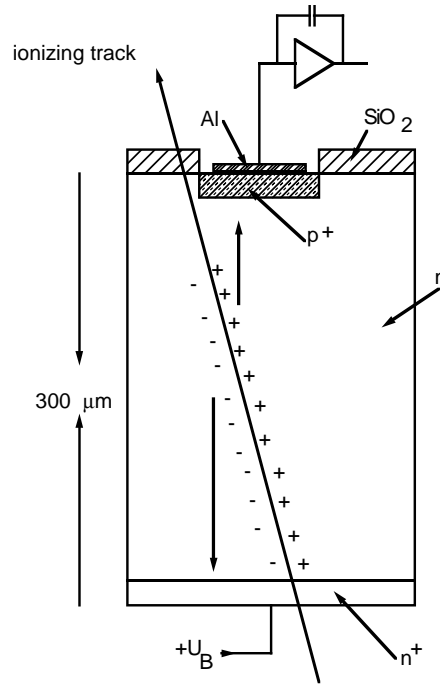


Figure 4.3: *The principle of a silicon detector.*

strips (0 V) and n-side strips (depletion voltage typically 30 - 60 V) a reverse biased p-n-junction is created. When the bulk is fully depleted, an electric field extends over the full thickness of the wafer from the p^+n junction to the n^+ strips. An ionizing particle creates electron-hole pairs in the silicon bulk material when passing through the detector. The produced holes and electrons drift along the electric field lines to the p-implant strips and to the n-side contact. From the implant strips the charge is transferred by implant-metal contacts and aluminium bonding wires to the preamplifier of the Analog Pipeline Chip (APC).

If one wants to read out strips on the n-side as well, one is faced with the following problem: The silicon bulk material is n-type, and the strips on the n-side are n^+ doped. The thin layer of SiO_2 covering the sensors contains an unavoidable positive space charge which comes from trapped holes and has been introduced during processing. This leads to an accumulation of negative charges underneath the silicon oxide layer between the strips, so there is a conductive layer between neighbouring strips. One possibility, which is used for the CST detectors, to separate the n^+ strips ohmically is by implanting p^+ strips between the n strips (see fig. 4.4). Once the detector is fully depleted, these so called p-blocking implants lead to an interruption of the negative charge layer and thus to an insulation between neighbouring strips.

The double sided, DC coupled silicon strip detectors have a sensitive area of 5.76 by 3.20 cm² and a thickness of 300 μm [54]. Fig.4.6 shows a photograph of the n-side of one of the detectors used to build the CST. There are 640 readout strips on each side. The read out pitch is 50 μm for the p-side ($R\phi$ coordinate), with

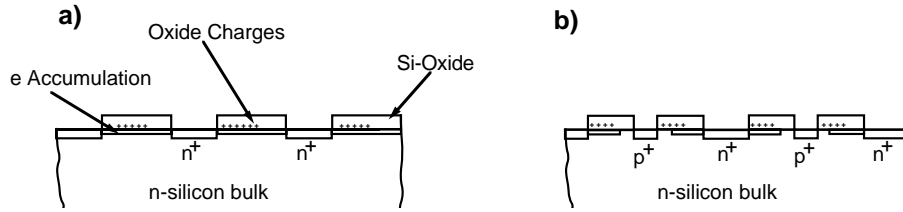


Figure 4.4: *The use of p-blocking implants for isolating n-side strips: a) shows the n-side of a depleted silicon detector with a conductive sheet due to trapped oxide charges between the strips, b) shows the ohmic charge separation of the strips by p-blocking implants.*

intermediate strips at $25 \mu\text{m}$. The charge reaching the intermediate strips induces signals on the read out strips by capacitive charge division.

On the n-side (z-coordinate) the strip pitch is $88 \mu\text{m}$, without intermediate strips. If the strip with the highest amount of deposited charge is taken as the hit-center, the expected resolution ($resolution = \frac{readout\ pitch}{\sqrt{12}}$) is $14 \mu\text{m}$ for the p-side and $25 \mu\text{m}$ for the n-side. By calculating the center of gravity the resolution is expected to improve. The increase in resolution due to refined algorithms is limited by the signal to noise ratio. The reconstruction of tracks from hits in both layers of the CST requires the knowledge of the relative position of each sensor, which will be determined from the data by an alignment procedure. With preliminary internal alignment, resolutions down to $12 \mu\text{m}$ for the p-side and $23 \mu\text{m}$ for the n-side have been measured [55].

Fig4.5 shows a model of the capacitive coupling in a silicon microstrip detector. Capacitors C_n and C_{n+1} are the capacitances to the next and over next strip, C_g is the capacitance of one strip to ground and C_M the Miller capacitance of the preamplifier [56]. The charge collected on one strip is distributed to the next and over next neighbours by capacitive coupling. Thus also the charge on the intermediate strips on the p-side is collected by the amplifier, which improves the position resolution without increasing the number of readout channels.

The p-implant (p-side) and n-implant strips (n-side) are in contact with the first layer of metallization (metal 1) over their full sensitive length. This is to decrease the resistivity for the signal path.

To allow for the n-side signals being read at the ends of the detector as well, there had to be added a second layer of metallization on the n-side (metal 2). The contact points between metal 1 and metal 2 can be seen in fig4.6.

For the n-side there are two contributions to the capacitive coupling: The strip to neighbouring strip coupling as already mentioned, and the coupling of one metal 1 strip to all 640 strips of metal 2, which run perpendicularly across the metal 1 strips over a $5 \mu\text{m}$ thick oxide layer.

The total capacitive load C_{ld} can be written as

$$C_{ld} = C_g + 2 \cdot C_n + 2 \cdot C_{n+1} + C_r,$$

where C_r is the capacitance of one strip to all other strips and C_g is the capacitance of one strip to ground (see fig. 4.5). This means that the charge collected by an n-side strip is not completely transferred to the preamplifier connected to this strip. Some fraction of the charge remains on the strip and induces mirror charges on all 640 metal 2 strips crossing it. Because of the spread the introduced charges are too small to be measurable. This mechanism reduces the signal to noise ratio on the n-side compared to the p-side.

Guard rings surround the sensitive detector areas. The guard rings are necessary to collect leakage currents produced by irregularities in the silicon structure at the detector edges, e.g. due to wafer sawing.

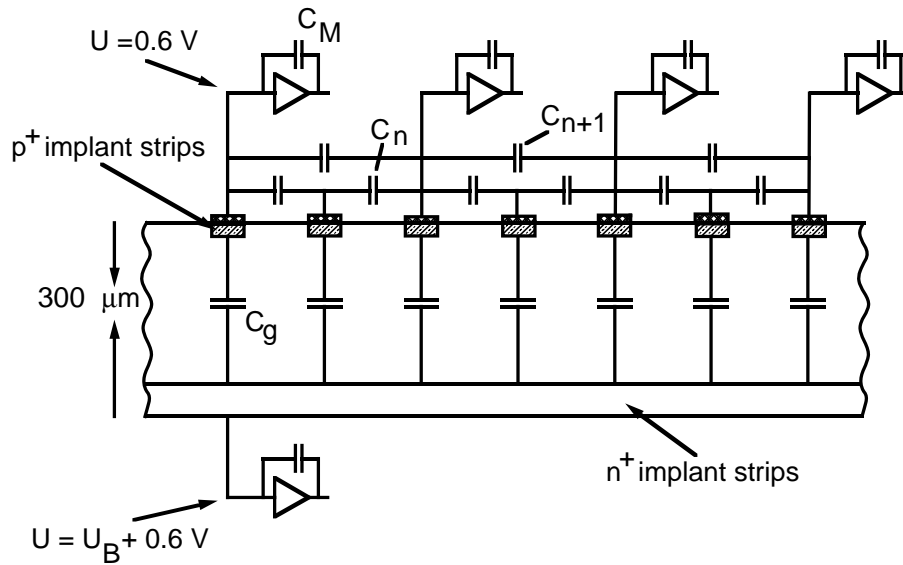


Figure 4.5: Model of capacitive coupling in a silicon detector with intermediate strips.

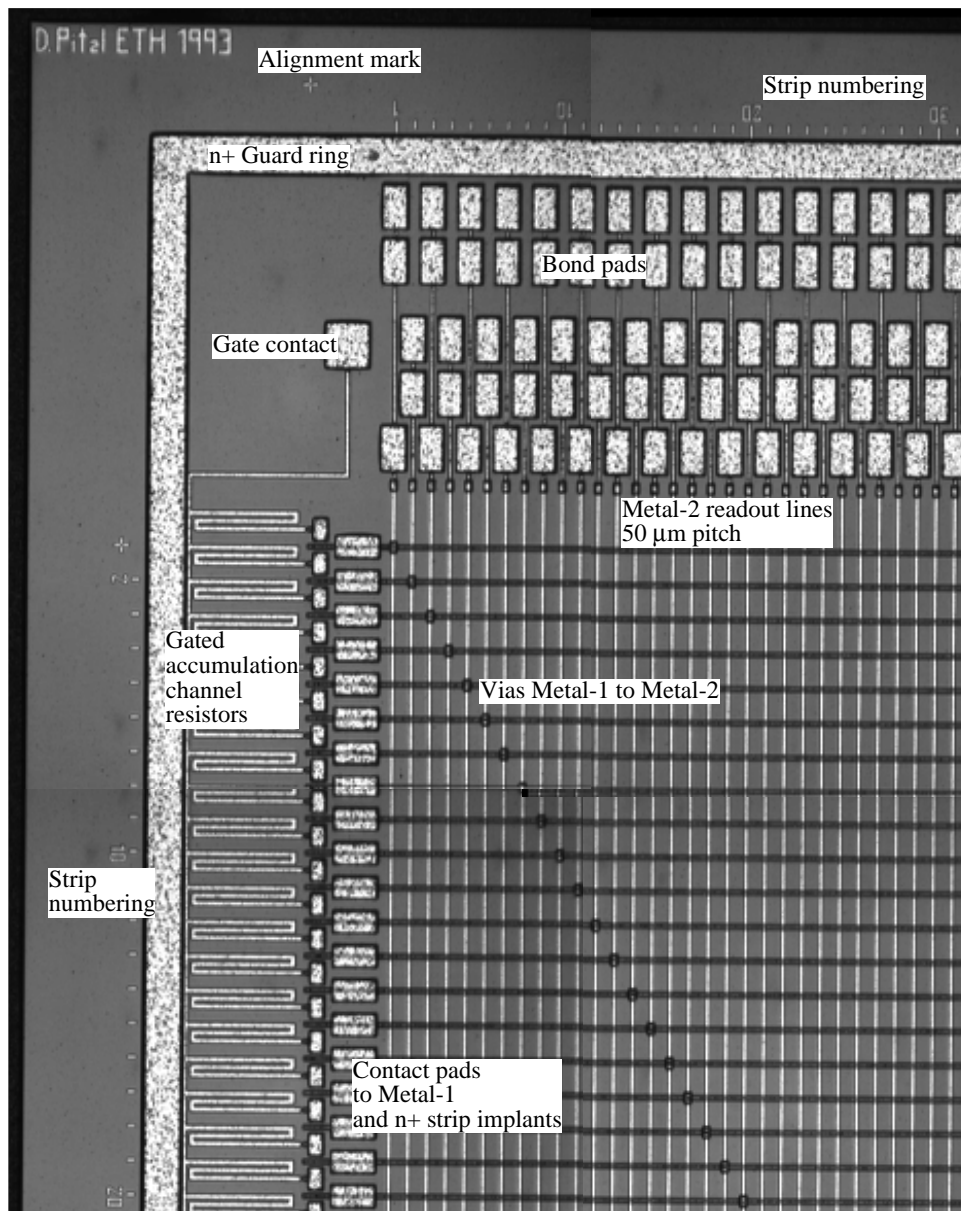


Figure 4.6: Photo of the n-side of one of the CST detectors, showing an area of about $2.5 \times 3.2 \text{ mm}^2$.

On the p-side a multiple ring structure grounds the strips by a punch through effect over $4\ \mu\text{m}$ gaps between p-side strips and the first guard ring. Since these rings are not grounded, there is a gradual increase of the voltage between strips and n-side potential at the detector edges.

This structure is called a multiple floating p^+ guard ring structure. The intermediate p-side strips float at a level of about 4 V. A FOX FET gate covering the gap is set to 0 V, but could be used to adjust the potential of the intermediate strips if required. This measure was not needed, since the potential between intermediate strips and bonded strips was low enough.

The first design of the CST was based on AC-coupled detectors, but could not be realized because of the high rate of defective coupling capacitors between the strip implants and the first metal layer on the n-side [54], and we had to resort to DC coupling. The disadvantage of DC-coupled detectors is that leakage currents from strips enter the preamplifier of the APC. This introduces a shift in the operation point of the preamplifier and, at very high leakage currents, eventually leads to saturation of the amplifier and to a loss of gain [56]. The shift in the operation point can partially be remedied by subtracting two pipeline buffers, one 'empty' one and one holding the signal. By accepting only detectors with a total leakage current below $6\ \mu\text{A}$ at full depletion the leakage current per strip entering the APC preamplifier should be small enough not to affect the signal height (leakage currents of more than 100 nA were found to decrease the gain). However single defective strips may have such high leakage currents that the preamplifier saturates. The quality criteria of accepting a detector for assembly were less than 1% defect strips.

4.2 Mechanical Construction

The CST consists of two cylindrical layers of silicon ladders and has a total length of 44.2 cm, the sensitive detector length extending over 35.6 cm. The length was chosen to cover the interaction region ($\sigma_z(\text{beam}) \cong 10\ \text{cm}$), but still to have an acceptable signal to noise ratio (longer detectors have a higher strip to strip capacitance).

Each ladder is built from two submodules, called half ladders. One half ladder contains three detectors with their strips daisy-chained by bonding wires. On one end a ceramic 'hybrid' containing the front end electronics is attached to the detectors and connected to the strips via bond wires.

The whole structure is mechanically supported by carbon fiber strips which are glued to the sides of the detectors and hybrids. Two half ladders are then glued together the same way forming a ladder. The carbon fiber strips, which have a thickness of $350\ \mu\text{m}$ and a height of 4.4 mm, are chosen such that the whole ladder does not sag more than $6\ \mu\text{m}$ in the vertical direction.

These self-supporting ladders with hybrids on both ends are then mounted on

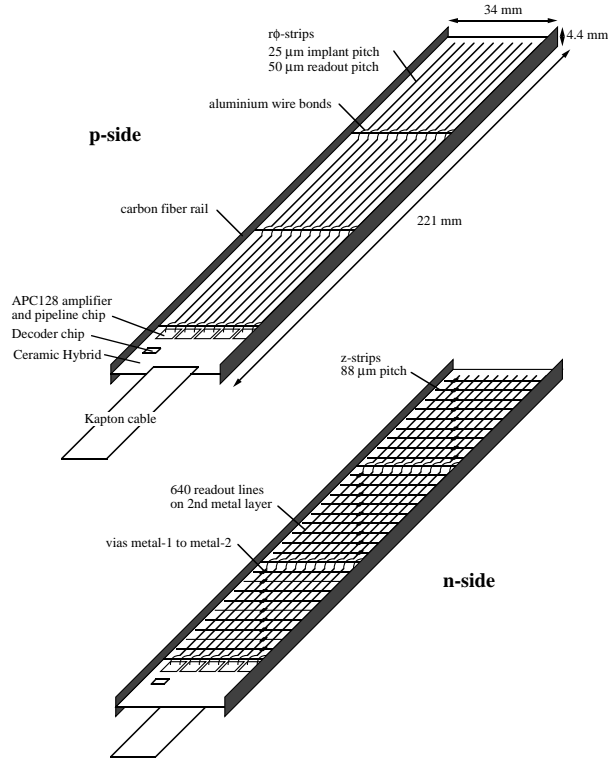


Figure 4.7: Schematic view of a half ladder. The upper part of the drawing shows the p-side, the lower part the n-side of one half ladder.

balconies of the carbon fiber endflanges [57] and fixed by two small screws. The ladders are mounted with an overlap of the active regions in the $r\phi$ projection. The inner layer, which consists of 12 such ladders, has a distance of closest approach (DCA) to the beam axis of 5.75 cm. The DCA of the outer layer, which is assembled out of 20 ladders, is 9.7 cm. The overlap of two ladders allows some tracks to pass through two modules of the inner layer or two modules of the outer layer. These tracks, which cause 3 or even 4 hits in different layers of the CST are expected to be very useful for alignment purposes [55]. The overlap amounts to 1.5 % out of 640 strips for the inner layer and 2.1 % for the outer layer.

The carbon fiber endflanges serve as a mechanical support structure as well as for integrating the water cooling: Since the front end electronics are situated on the hybrid and produce $\approx 40 W$ of heat, cooling is necessary. The whole CST is surrounded by a Rohacell cylinder. On both sides of the cylinder 50 μm thin aluminum foil is glued to provide a shielding against electromagnetic interference.

4.3 Read Out Concept

Fig. 4.9 shows the principle of the read-out concept of the CST:

Two neighbouring ladders (two half ladders on the $+z$ end and two half ladders on

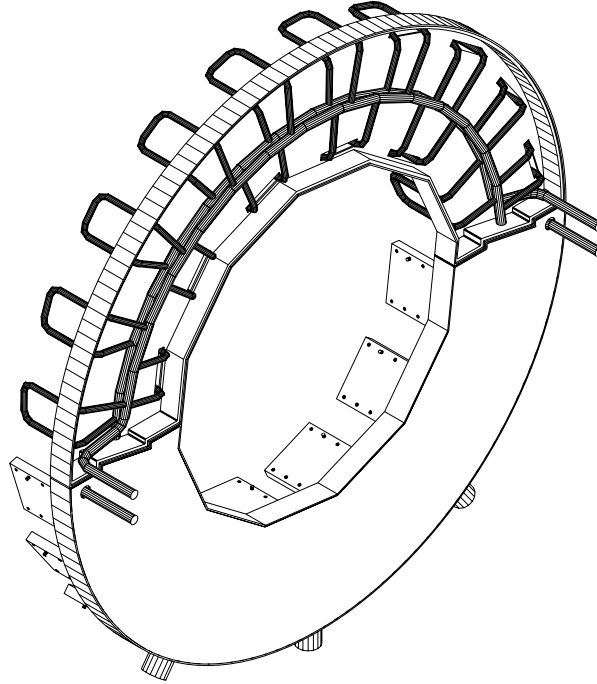


Figure 4.8: *Sketch of the carbon fiber end-flange with cooling pipes. The cooling pipes branch off into the balconies. On these balconies, ladders are mounted such that the hybrids are fixed on the balconies.*

the $-z$ end) form a read out unit, called a family: They share bias-, analog- and digital voltages. Double sided hybrids carry the front end electronics including the APC chips, decoder chip, LED driver and current source for the preamplifiers of the APCs. The side of the hybrid which controls the n-side of the detectors is operated at bias potential. This avoids putting capacitors between detector strips and APCs, which would have taken up too much space. So the same design could be used for front- (operating the p-side of the detector) and back side (operating the n-side of the detector) of the hybrid ¹. Thus the bias voltage for the n-side of the detectors serves as ground for the n-side of the hybrids and supply voltages are at the level $V_{bias} + V_{supply}$. The ground of the front side of the hybrid is at 0 V.

Since the APC chips are the biggest consumers of power on the hybrid, it is of great importance to have an efficient heat conduction from the front part of the hybrid where the chips are sitting to the back part, where the hybrid is fixed on the balcony and where the water cooling is situated. Aluminium Nitride was chosen in favour of Aluminium Oxide, because it has a much better heat conductivity ($\lambda_{Al_2O_3} = 25 W/mK$, $\lambda_{AlN} = 160 W/mK$).

One APC chip contains 128 channels, so there are 5 chips per side sitting on the

¹Here front side and back side are used with respect to the hybrid. For the CST, the hybrids are mounted such that in the inner layer the p-side faces the beampipe and in the outer layer the n-side faces the beam pipe.

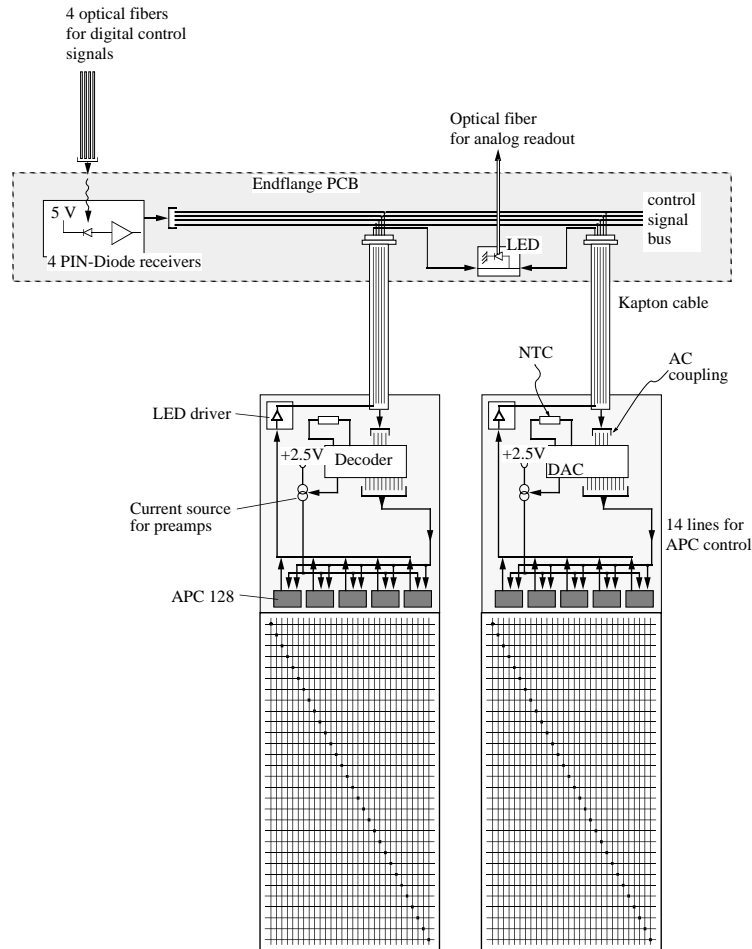


Figure 4.9: Sketch of part of the read out: two half ladders are connected to the end ring print. The end ring print serves as a distributor for power and control signals. Furthermore the electrical analog output signals are converted to optical signals. Outside the H1 detector, in the electronic trailer, the optical analog signals are converted back into electrical signals and digitized with fast analog to digital converters in the ONSIROC [58]. Additionally, the digital control signals from the sequencer module, which is situated on the ONSIROC, are converted into optical signals by converter cards.

front end of the hybrid.

Signals from the silicon detector are transmitted via bonding wires to the APC, amplified and stored in a 32 buffer deep switched-capacitor pipeline. During data taking the pipeline is operated continuously with the frequency of the HERA clock. After a delay of typically 24 bunch crossings since the time the event happened, a trigger signal arrives to keep the data. Then all channels of the chosen buffer, which means the analog signals of all detector strips of a certain time slice, are subsequently read out.

The multiplexed analog signals are brought to transimpedance by an output

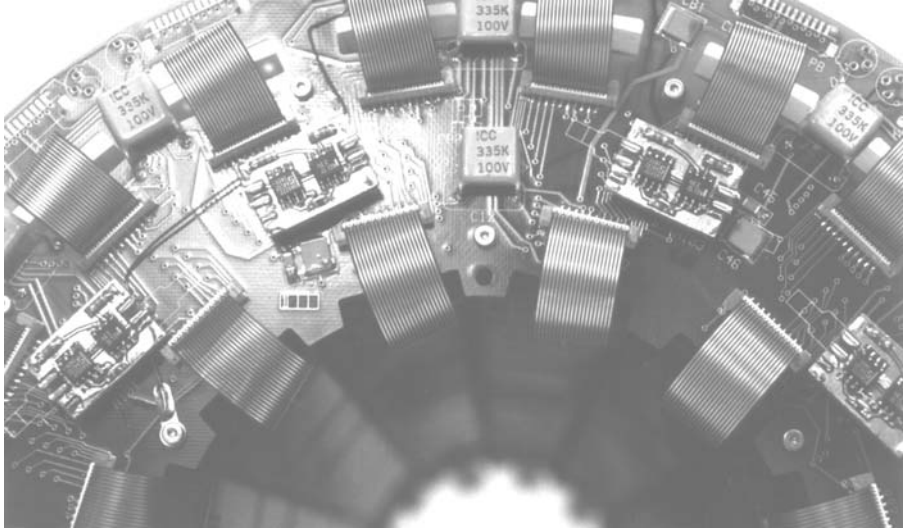


Figure 4.10: *Photo of part of Detector Endring Print.*

amplifier sitting on the hybrid (LED driver). From there they are transmitted via a 5 cm long Kapton cable to a printed circuit board, called detector endring-print (Endflange PCB). Here the electrical to optical conversion takes place using LEDs, and the analog signals are transferred to the electronic trailer of the H1 experiment. One optical fiber is used to read out both p-sides and another one to read out both n-sides of the half ladders belonging to one family. In the electronic trailer the optical signals are converted back to electrical analog pulses and, after being amplified and converted to differential signals on converter cards, fed into VME modules, called online silicon read out controller (ONSIROC [58]). One module gets the analog signals of one family on four input lines. Here the conversion of the analog signals into digital signals takes place.

The digital sequences which control the operation of the front end electronics are produced by a sequencer sitting on the ONSIROC. They are converted to optical pulses by digital to optical converter cards and reach the end ring print via optical fibers, 8 optical fibers being grouped together in one optical cable. The end flange print converts the four digital control signals from optical to electrical with PIN diode receivers and distributes them via bus lines to all Kapton cables. The control signals that come from the Endflange are brought onto the hybrid via Kapton cables and are AC-coupled to the decoder chip input lines. One Kapton cable contains all signals necessary to operate one half ladder: Two lines for analog hit signals (p- and n-side), eight power lines (V_{analog} , $V_{digital}$, V_{bias} , V_{ground}) and two times four lines for the differential digital control signals.

The endring-print is mounted on the carbon fiber support structure. The read out of one quarter of the CST is controlled by one ONSIROC.

4.4 The APC128

In this section, the APC is described, starting at the preamplifier. The operation of the APC under normal data taking conditions and the calibrating mechanism, a very important means of providing calibration of the complete read out chain, are described. Finally, the method used for testing all delivered APCs is explained.

The APC128 is an ASIC chip which is built in SACMOS 1 technique ($1.2 \mu\text{m}$ feature size). One chip contains 128 input channels, each followed by an analog pipeline. The design of this read out chip gives the possibility of storing for each input channel signals of up to 32 time slices (bunch crossings). One peculiarity is the re-reading architecture where the analog signal, being amplified and stored on the buffer capacitors, is re-read, using the pre-amplifier again, before being read out through the output amplifier [53].

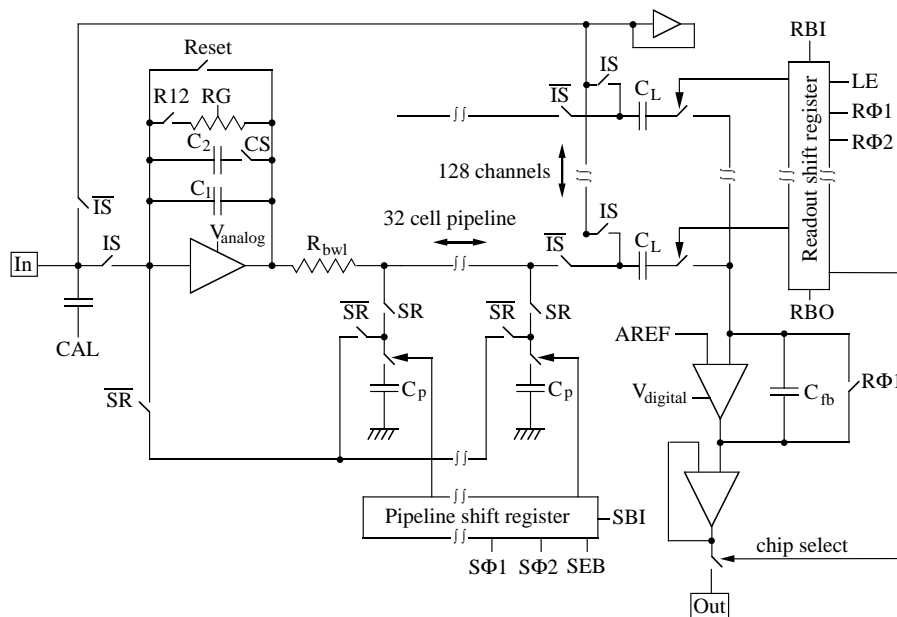


Figure 4.11: *Electrical diagram of one channel of the APC chip.*

Fig. 4.11 shows the electrical diagram of the APC chip. The following components are implemented for each channel, 128 channels per chip:

- analog preamplifier
- 32 cell pipeline with pipeline buffer capacitors C_p
- Latch capacitors C_L

Whereas these components are only there once for all 128 channels on one chip:

- Pipeline shift register (sample shift register)
- read out shift register with read-out amplifier

By using switch **IS** it is possible to connect or disconnect the detector strips from the chip input. The detector signal is collected on the feedback capacitor of the preamplifier and then stored on a pipeline buffer capacitor C_p . If a trigger decision is made to read out a certain buffer, switches **IS** and **SR** are opened and the detector strips are disconnected, thus closing **SR** and **IS**. The charge on capacitor C_p is then reread using the preamplifier again and stored on the latch capacitor C_L . Then the charges on all 128 latch capacitors are read out serially using the output amplifier. To be able to read out several chips consecutively, the bit which is clocked through the read-out shift register and which connects the latch capacitors to the output is fed from the output of one chip to the input of the next chip.

In the following, single components of the APC are described in more detail.

4.4.1 The Preamplifier

The input amplifier consists of a single push-pull inverter stage. This configuration was chosen because it gives lowest possible noise at small power consumption: Since the transconductance g_m is the sum of the transconductances $g_{m,n}$ and $g_{m,p}$ of the two transistors, the equivalent noise resistor is only about half the value of a single input transistor. Fig.4.12 shows a circuit diagram of the analog preamplifier of the APC128 with C_{Ld} as capacitive load on the input (detector strip capacitance), C_1 as feedback capacitance and C_P as buffer capacitance. R_{BWL} is a resistor which can be set in order to limit the bandwidth, its gate voltage being supplied via bond pad. For a given input charge Q_1 the output voltage depends on the feedback capacitance C_1 : $\Delta V_{out} = -\frac{Q_1}{C_1}$.

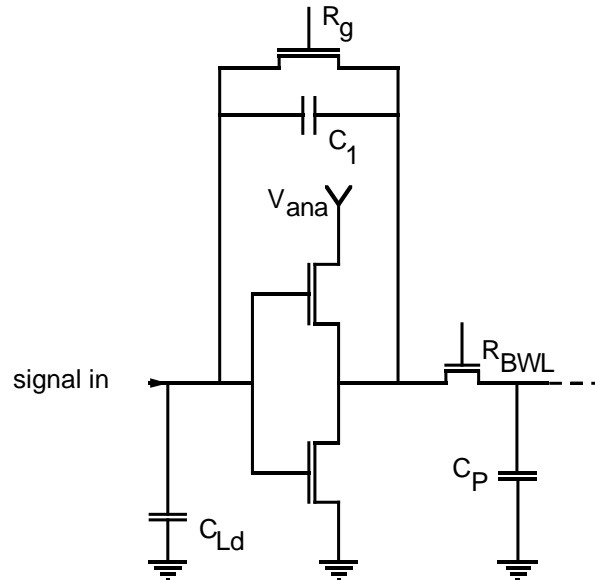


Figure 4.12: Circuit diagram of the analog preamplifier of the APC 128.

When operating the CST with the APC128, it has to be taken into account, that the input capacitance C_{Ld} is large due to the long strips (3 detectors daisy-chained gives 17cm long strips). As mentioned already, C_{Ld} is larger on the n-side than on the p-side. The total strip capacitance on p-side and on n-side are measured as 27 pF and 57 pF respectively. This means that the signal to noise ratio on the n-side is considerably smaller than on the p-side.

The amplification factor of a charge sensitive amplifier configuration can be calculated with the help of the Miller Capacitance C_M :

$$C_M = (Gain + 1)C_1. \quad (4.1)$$

With a measured open loop gain of about 200 the Miller Capacitance is about 90 pF. So only a part of the original charge collected by a strip is stored on the feedback capacitance:

$$Q_{Amp} = Q_{signal} \cdot \frac{C_M}{C_M + C_{Ld}}. \quad (4.2)$$

To calculate the signal to noise ratio for both p-side and n-side, the following equation is used (here the effect of the Miller capacitance cancels out, since it applies both to signal and to noise):

$$\frac{S}{N} = \frac{22000e}{700e + 50 \frac{e}{pF} \cdot C_{Ld}}, \quad (4.3)$$

Here 22000 e represent the charge of one minimum ionizing particle in 300 μm of silicon. The numbers for noise and noise per capacitive load have been measured in a test setup [59].

This gives a signal to noise ratio of $\approx 11 : 1$ for the p-side and $\approx 6 : 1$ on the n-side. The signal decay time can be changed by setting RG (done with bit 64 from the decoder chip and a voltage divider). For a capacitance C_1 of about 0.45 pF and a resistor R_g of about 1 M Ω , the signal decay time is $\tau \approx 450 ns$.

4.4.2 The Operation of the APC128

Fig.4.11 shows the circuit diagram of one channel of the APC: The operation of the APC128 can be divided into 4 phases, as shown in fig.4.13. At start of data taking the chip has to be prepared for sampling in an **initialisation phase**: The **RESET** and **R12** switches are closed and all buffers are reset to the level of the preamplifier. During this the opening of \bar{IS} disconnects the read out part of the chip and inhibits C_L from loading the preamplifier output. With **R ϕ 1**, **R ϕ 2** and **RBI** high the read out shift register is brought to a 'high' state. Now **LE** is closed and simultaneously the right side of all capacitors C_L are reset to the input level of the output amplifier. This is done to have stable conditions and to prevent the capacitors from charging up. The left side of C_L is connected to an extra amplifier in a feed back loop to

Figure 4.13: *Flowchart of control signals for operating the APC*

With the help of the sample clock the **SBI** is clocked to the buffer which is to be read out. Now the **RESET** switch is opened again. The charge sitting on a buffer is re-read by the preamplifier and stored on the capacitor C_1 by opening of **SEB** for a certain time, allowing for the rise time of the preamplifier. All switches connecting C_L to the read out amplifier are opened now simultaneously by setting **LE** to zero. The output charge of the preamplifier is now stored on the latch capacitors.

Now the analog preamplifier is reset again and the sample pipeline bit is clocked forward one step to the buffer where the signal is expected to be. The **RESET** switch is opened again and, with the opening of **SEB**, the charge coming from C_P is transferred to C_1 and kept there, waiting for the final read-out.

The difference between the potential on the right side of the latch capacitor and the working point of the read out amplifier corresponds to the charge difference of the two buffers read out. The signal created by a particle passing the detector and the rise time of the preamplifier is shorter than the bunch crossing time. This means, that one time slice, that is one buffer, carries the signal and the previous buffer only carries the pedestal value. By subtracting two buffers the offset, or pedestal is subtracted and the actual charge coming from the particle remains. This charge, waiting on C_L is read out as follows: In the fourth phase, the **read out phase**, by closing **LE** and clocking a read bit through the read out shift register the latch capacitors of all channels are subsequently connected to the output amplifier and to the optical read out.

As mentioned before two half ladders are read out through the same optical fibers. Because all ladders receive the same control sequence, a distinction has to be made. This is done by using two of the decoder chip bits as switch bits. On the so called ‘early’ half ladders one bit is bonded to the APC as chip select, on the ‘late’ half ladders the other bit is bonded. By switching these bits on and off both HL can be read out consecutively.

4.4.3 The Calibration Mechanism

The APC has implemented the possibility of calibration: For this purpose the chip is operated the same way as in normal data taking. As can be seen in fig. 4.11 there is in addition to the detector strip a calibration capacitor connected to the input of the analog preamplifier.

A calibration sequence can be given onto this capacitor via bond pad. This charge then is treated in exactly the same way as a normal detector input signal. To simplify recognition of single channels, there are four different sizes of capacitors for four neighbouring strips, so the output shows a step pattern which repeats itself after every fourth channels. This calibration mechanism provides an excellent method for testing and calibrating the whole read out chain, since the injected charge is well defined.

4.5 The Decoder Chip

The decoder chip is an ASIC specially designed for the APC and fabricated in SACMOS1 technology. The main feature of the chip is to perform a serial to parallel conversion of the incoming signals, thereby having four different functions:

- Providing the APC with control signals

- Sending a digital sequence of 32 bits as calibration signal to the APC to simulate the detector input
- Providing switches for slow control purposes, e.g. temperature measurement
- Regulating the analog current supply with a 7 bit DAC

The Decoder runs in two major modes of operation which are switched by the switch bit (OUT/SR). The first mode of operation is the downloading of a bit string containing up to 64 bits from the OnSiROC-sequencer into the decoder internal shift registers. The data bits are clocked in serially with the two clock signals with a speed of up to 10 MHz.

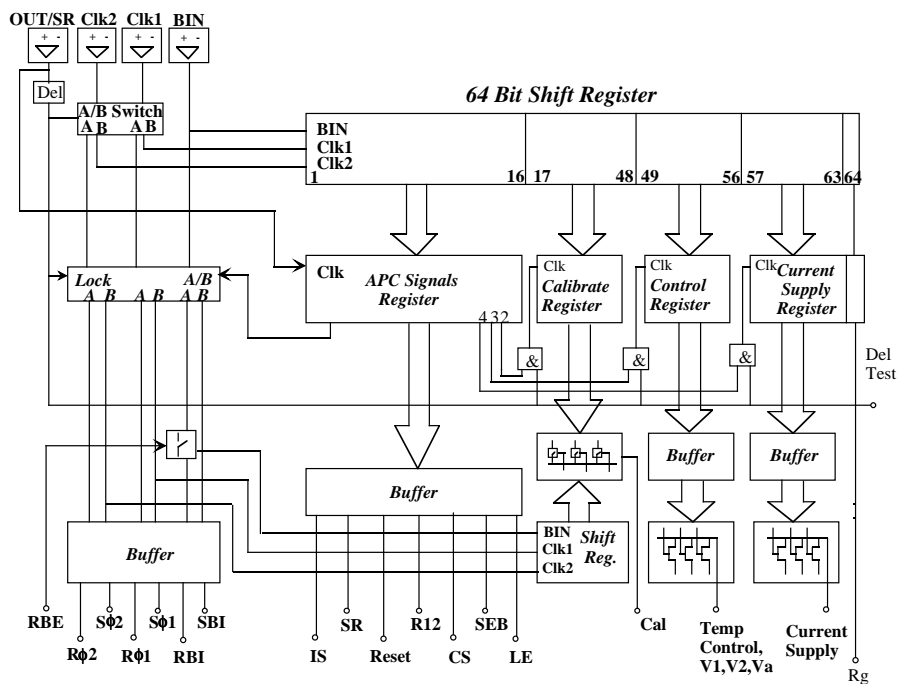


Figure 4.14: *Layout of the Decoder chip.*

For the second mode of operation, the OUT/SR bit has to switch: The two clock bits and the data bit are now directly connected to the output and serve as sample- or readout clocks for the APC. The distinction between those two possibilities is done by the first bit of the 64 bit shift register via the switch A/B. At the same time the bits stored in the decoder shift register are downloaded into buffers. Bit No. 5 to 16 are provided at the output of the decoder and are distributed via bus lines. They serve as control bits for the APC. If bit two is set then the bits in the calibration shift register can be clocked out sequentially using the sample clock. Buffer No.3, enabled by bit 3, provides switches for putting the voltage of the R_{NTC} as well as other control voltages on the analog signal read out line: With the digital voltage

as supply and some resistors, control voltages are created. Buffer No.4, enabled by bit 4, holds a pattern for a DAC that controls the current supplied to the analog part of the APC.

4.5.1 The Principle of the Clock Mechanism

The four control signals, which are the input to the decoder, consist of one select bit, one data bit and two clock bits. These four differential inputs can be used by applying a differential signal or only the positive input while grounding the negative one. The total difference should not exceed $5V$. A feature, which is used in our case, is the fact that the input receiver of the Decoder chip 'holds' the signal. Fig. 4.15 shows a circuit diagram of one of the four decoder input receiver. The change between the two digital states is done at the rising signal edge. As the digital signals reach the decoder chip via capacitive coupling, it is necessary for the input receiver to keep the signal and not to 'snap back'.

Fig.4.16 shows a triangular pulse given as input of the positive differential input line, while the negative line was set to zero. The Photo shows that at a certain level (here 34 mV) the input receiver of the chip switches and holds the signal.

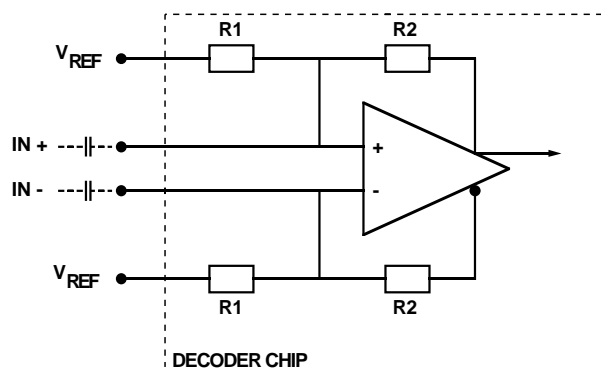


Figure 4.15: Schematic drawing of the differential input of the decoder chip.

The actual level which is needed to switch the input strongly depends on signal frequency and input condition (AC- or DC-coupled). The low value of 34 mV is observed for a DC signal and very low frequency. For realistic CST operating conditions (40 MHz clocks, AC-coupling with 15 pF capacitors) a minimum difference between positive and negative input signal of 220 mV is needed.

All shift registers for the Decoder chip as well as for the APC128 are operated according to the same principle.

Each shift register cell consists of two inverters with small inverters to 'hold' the signal. The switches which are opened and closed by the clock signals are minimal feature size transistors. In order to clock a bit into the shift register cells and supply it at the output of one cell, clock1 (CLK1) and clock2 (CLK2) have to be used as shown in fig.4.17.

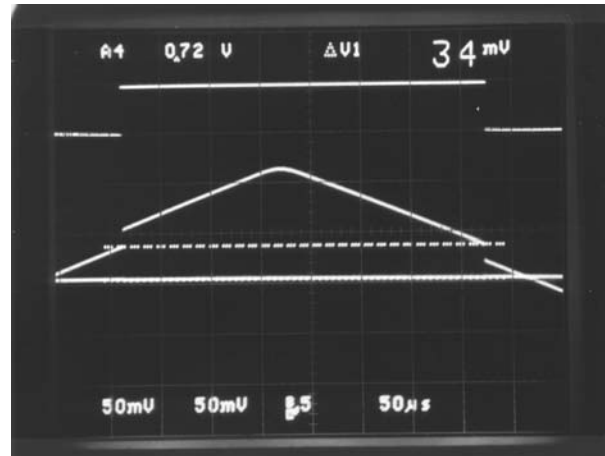


Figure 4.16: Oscilloscope photo of clock pulse entering- and leaving the Decoder chip. The two lower lines, the triangular clock pulse ($CLK +$) and the line at zero ($CLK -$) show the decoder input signals, the upper line shows the output pulse ($S\phi 1$).

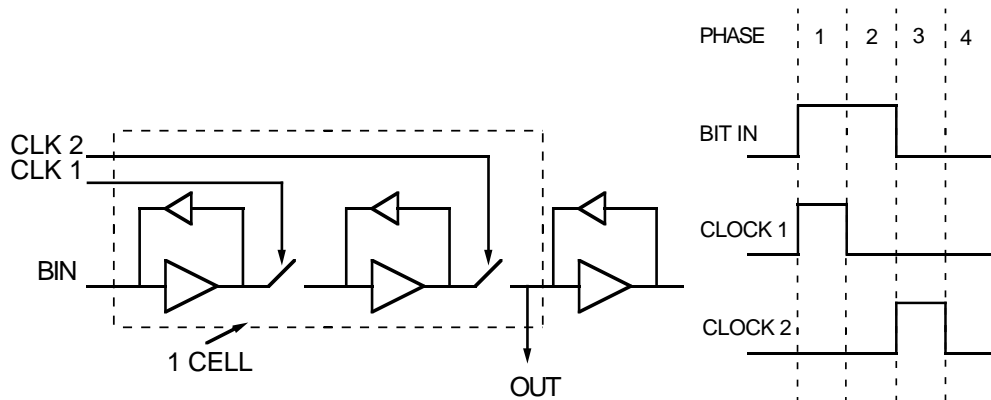


Figure 4.17: Sketch of one shift register cell and the corresponding clock cycle to operate the cell.

It is crucial that clock 1 returns to low while still applying the desired input signal on the bit-in line (BIN).

4.5.2 The Current Supply - DAC

With bits 57 to 63 of the Decoder chip the current of the analog voltage supply for the APC analog amplifier can be regulated (enabled by bit 4).

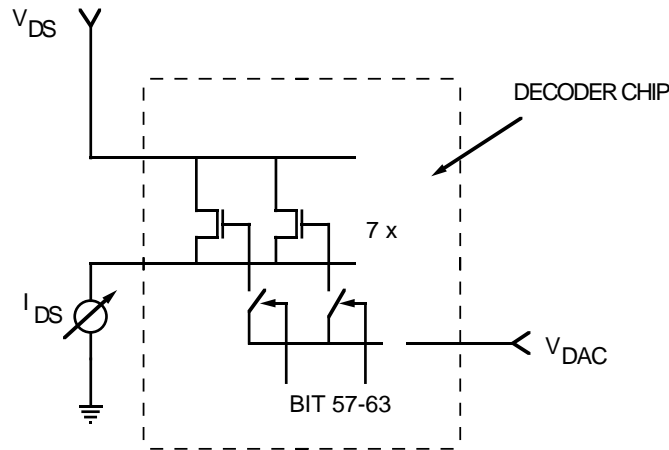
This is done by transistors on the Decoder chip. The voltage for the source of those transistors is supplied via bond pad. The drain is connected via bond pad as well to provide the output current.

With the help of a simple circuit, as shown in fig. 4.18, the characteristic of this current source can be measured: Keeping $V_{Ana} = 2.5$ V and $V_{DAC} = 2.0$ V

bit pattern	output current [mA]
0000001	1.55
0000010	0.803
0000100	0.409
0001000	0.201
0010000	0.103
0100000	0.052
1000000	0.026
0000000	0.0

Table 4.2: Relation between set DAC bits and output current

fixed, the relationship between bits set and current output can be measured (table 4.2). To illustrate the properties of the transistors used, fig.4.19 shows the output current I_{DS} as a function of V_{DS} with fixed V_{DAC} .

Figure 4.18: Sketch for measuring I/V characteristics of the DAC.

4.5.3 The Monitoring of Temperature and Supply Voltages

To calibrate the read out chain and to monitor hybrid temperature and detector supply voltages, so called special events are used. The 2×4 special events per hybrid are read out for each event following the data stream. Each special event displays a voltage, thus two times four voltages per half ladder are read out following the raw data flow.

Fig. 4.20 shows the electrical layout of one part of the hybrid. For the p-side the supply voltage for the analog preamplifier of the APC128 (V_{analog}), the reference Voltage (A_{ref}) and two control voltages (V_1 , V_2) are monitored. On the n-side V_{analog} , V_2 , V_1 , and V_{NTC} are monitored.

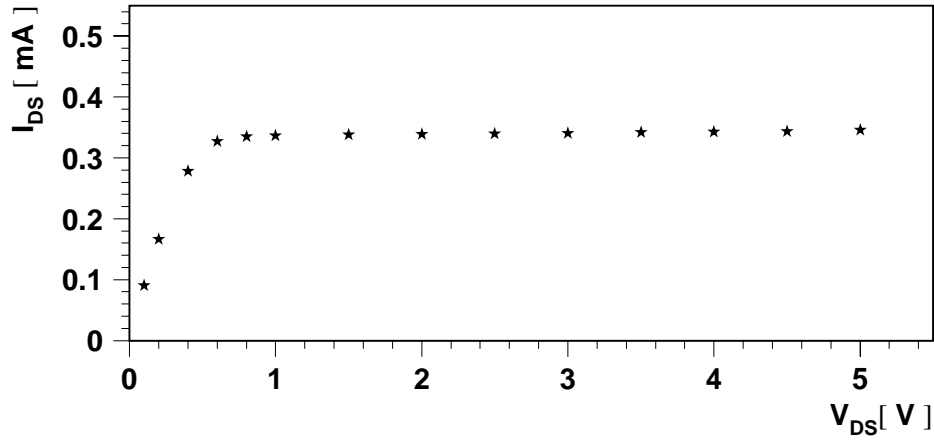


Figure 4.19: I/V characteristics of the transistor used for the current supply.

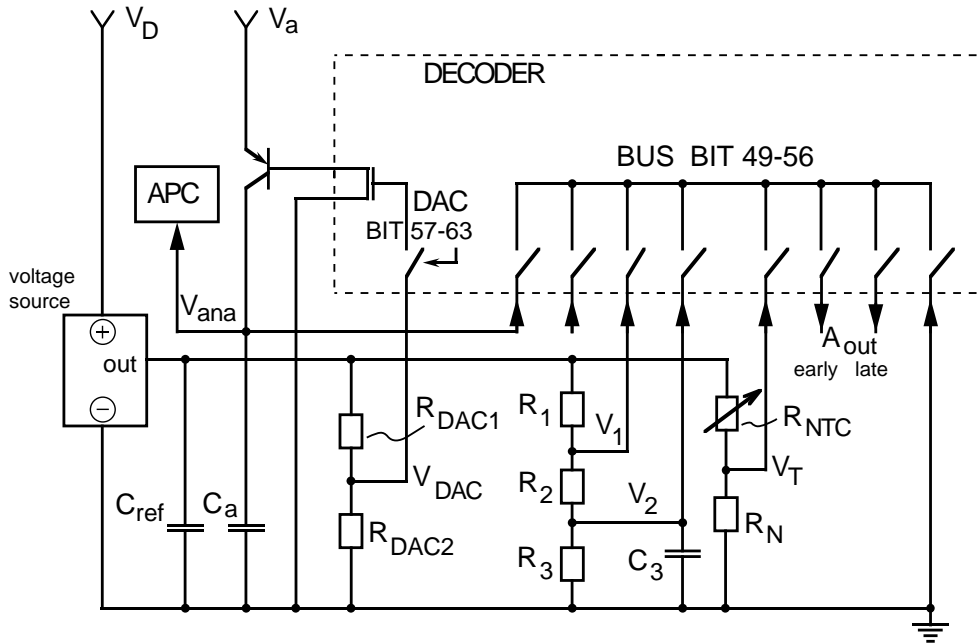


Figure 4.20: *Electrical circuit to measure the voltages of the special events on the hybrid. The special voltages can be connected to the analog output line using bits 49 - 56 of the decoder chip.*

Using the temperature dependent resistor R_{NTC} and two constant control voltages (V_1, V_2), the temperature on the hybrid and the value of the analog voltage can be calculated:

$$(V_i)^V = V_1^V - \epsilon * (V_1 - V_i)^{ADC} \quad , \quad (4.4)$$

with $\epsilon = \frac{(V_1 - V_2)^V}{(V_1 - V_2)^{ADC}}$.

Here the superscripts V and ADC denote whether the value is measured in volts (on the hybrid) or in ADC counts, and V_i stands for V_{Ana} or V_T . Once the value of V_{NTC} in Volts on the hybrid is known, the temperature in Kelvin can be calculated according to:

$$T = \left(\frac{1}{T_0} + \frac{1}{B} \cdot \ln \frac{R}{R_0} \right)^{-1}$$

where B is a constant, T_0 is the temperature at which the calibration of R_{NTC} took place, and $R = \frac{V_{ref} - V_T}{V_T} \cdot R_{NTC}$.

$$T[K] = \left\{ \frac{1}{T_0} + \frac{1}{B} * \ln \left[\left(\frac{V_{ref}}{V_T} - 1 \right) * \frac{R_{NTC}}{R_0} \right] \right\}^{-1}. \quad (4.5)$$

$$\Rightarrow T[^\circ C \text{ on hybrid}] = T[K] - 273.15K \quad (4.6)$$

with $V_{ref} = 2.5V$, R_{NTC} (at $20^\circ C$) = $6.8k\Omega$, $B = 3434K$ and $R_0 = 5k\Omega$.

4.5.4 Testing the APC and Decoder Chips

Both chips had to be tested before being assembled on the hybrid because of the delicate bonding procedure. For this purpose probe cards were produced. These cards consist of small epoxid based boards with a circular hole in the middle. Needles with their small tips bent downwards are assembled and fixed in the horizontal plane according to the bond pads on the chips. They can be contacted electrically by printed circuits leading to a connector. These probe cards are lowered onto a chip under a microscope. In two separate test set ups test sequences were applied with a pattern generator.

Fig. 4.21 and 4.22 show the bond pad layout of both APC and Decoder chip. To test the APC the function of the decoder chip was taken over by a pattern generator. On a small print the different supply voltages as well as the control signals were provided and given to the probecard. The test sequence of the APC was basically the same as described above. The only difference was that no subtraction was performed and the re-read sequence was repeated for each buffer. This way any variations from buffer to buffer, single broken capacitors C_P and defects in the read out or analog part could be detected. The selection criteria were strict (no defect channel and all buffers of one channel uniform), and the yield was of the order of 35 %.

For the decoder chip all different functions were tested individually to guarantee a perfect working. For this purpose a small board was designed simulating the demands. It contained an adjustable power supply for the DAC, eight input lines (+/-) for the digital control signals (the positive line switching between 0 and

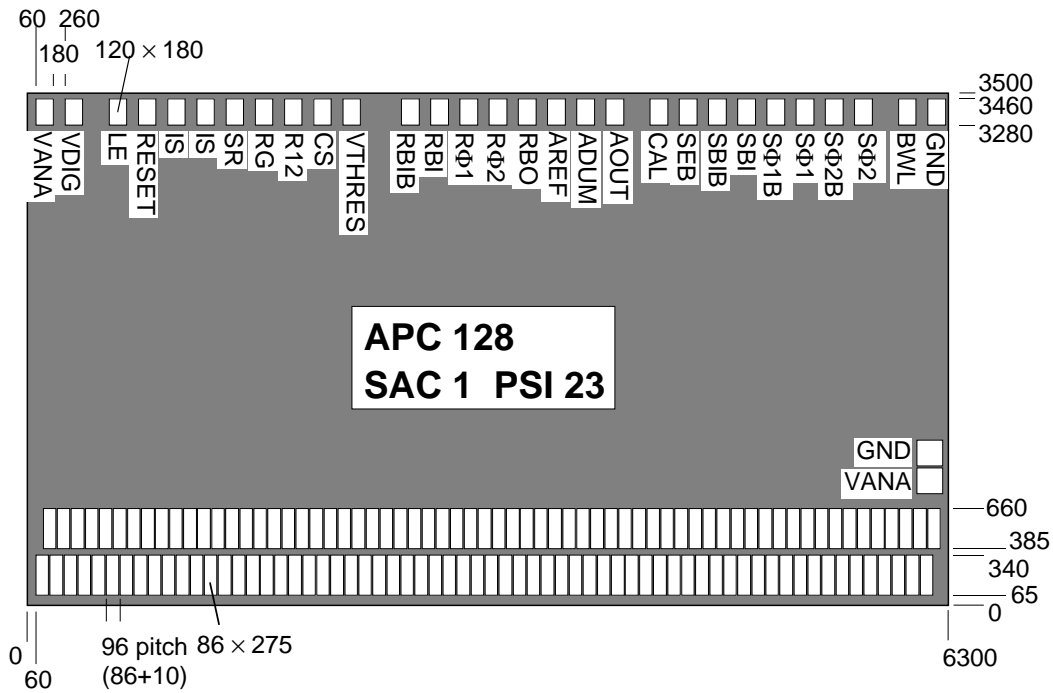


Figure 4.21: *APC 128 bond pad layout. The overall dimensions are $3.5 \times 6.3\text{mm}^2$, and the units given in the fig. are in μm .*

1 V, the ‘negative’ line at about 0.1 V). The bus lines of the decoder chip were connected to voltage dividers with a different size resistor for each bus line. Output bits 5 to 16, the bus lines, the clocks and the voltage output of the DAC were connected to a switch box. The output of the switch box could be viewed with an oscilloscope. Thirteen test sequences in total were programmed to test all possibilities. Each test sequence was running in an endless loop, producing the result of the test on the oscilloscope. To jump from one sequence to the next a trigger had to be applied. The Decoder chip proved to have a very good yield ($\approx 95\%$).

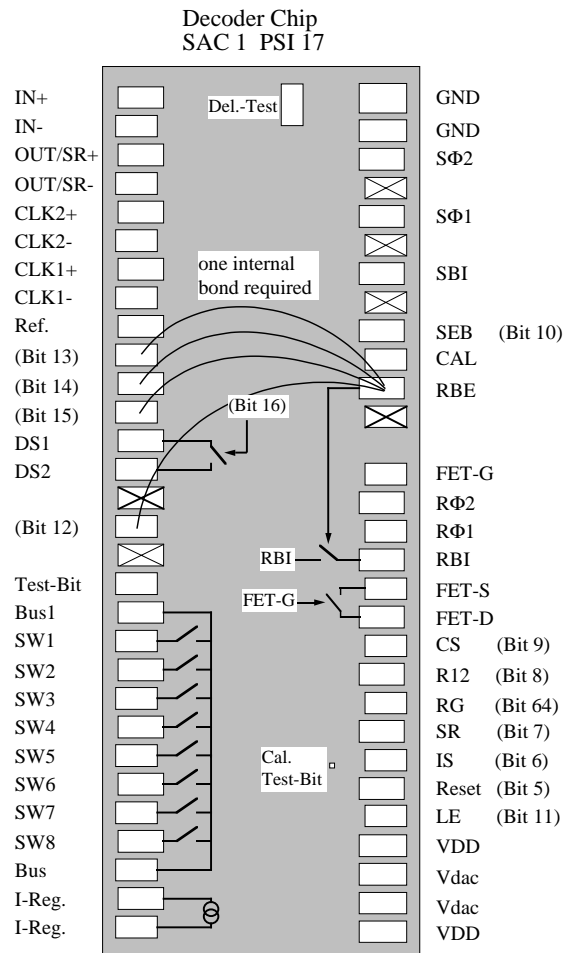


Figure 4.22: Decoder bond pad layout

Chapter 5

Analysis of CST Data

Due to several delays in the delivery of the detectors and APC chips it was not possible to finish all modules in time. During the shutdown in winter 94/95 the lower half of the CST was installed for test purposes.

Because of a leak in the water circuit in an inaccessible place cooling was not possible. When operating the lower half of the CST temperatures of up to 60 °C were reached. When keeping such high temperatures over longer time damage could be done to the detector. Also the leakage currents of the strips reached very high levels. Since the leakage currents enter the input of the preamplifier together with the signals the gain changes and the actual signal height which is read out can be considerably smaller [56]. Therefore only two families were operated, one in the inner layer and the family in the outer layer corresponding to the same sector in ϕ . During operation, most of the running period in 1995 was needed to debug the sequencer and to optimize the computer code for the control signals. Although it was not possible to fix all bugs, the problems became known and could be solved for the running period of 1996. The capacitance of the bus lines distributing the digital signals on the endring print proved to be an additional problem: The bus lines were not terminated properly and so the signals for the decoder chips were distorted. The bad signal quality on some positions led to occasional misinterpretations of the signals by the decoder chip. This led to corrupt data for some events.

The data used in this analysis were taken with the H1 detector under normal luminosity conditions. This means for each event data of all H1 subdetectors are available.

5.1 Raw Data

The data read out during the year 1995 are raw data (no online hit-finding and zero suppression). This means the ADC values of all channels are available and can be converted into signal height in mV with the help of calibration voltages (special events). The special events are read out following the strip data for each family for all events.

Fig. 5.1 shows raw data of two half ladders (p-side and n-side) for one event. The

bin numbers correspond to the strip numbers on the detectors.

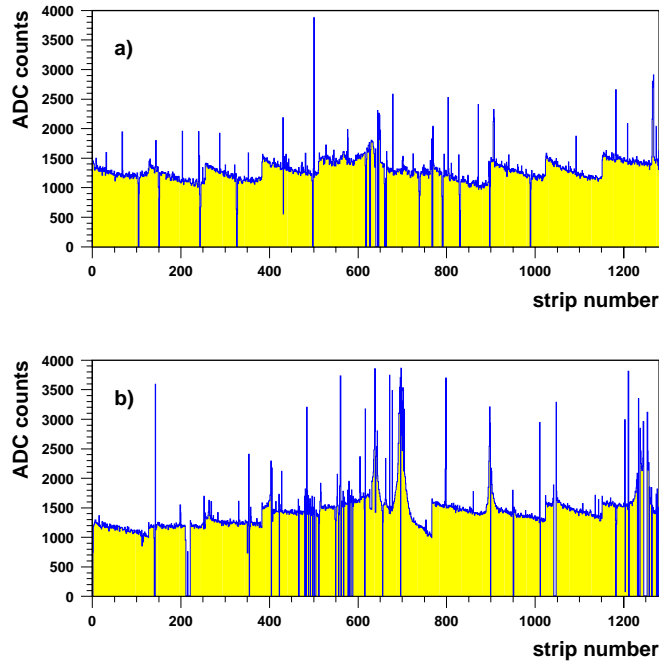


Figure 5.1: *Raw data pulse height distribution for one early and late HL-pair (a: p-side, b: n-side): Shown is the pulseheight of each strip for all 1280 strips of two neighbouring half ladders, which form one read out unit.*

Since the data displayed belong to two half-ladders (HL), strip numbers 0 to 639 represent the early HL, strip numbers 640 to 1279 the late HL. The offset is introduced in order not to cut off negative fluctuations in the data. The chip structure, which is clearly visible, is due to slightly different offsets per chip and different pedestals per channel. The pedestal variations are greater at the borders of the chips, which are expected from the chip design. Channels with underflows can be explained by too high leakage currents from detector strips. The number of saturated strips per HL (p/n side) is shown in table 5.1. Not included here are those strips which are in the right range for read out but insensitive to any signal due to saturation from leakage currents.

The ADC value of one strip is monitored over a certain number of events in Fig. 5.2. The Gaussian spread is due to different sources of noise.

In order to get a reliable number for the signal to noise ratio, it is important to investigate all of these different sources. Furthermore in order to detect a 'real' signal coming from a particle it is important to have all strips centered around the same offset value, preferably zero. It then becomes possible to recognize signals on individual strips or clusters. In the next section, noise effects due to data transmission are analyzed with the help of the special events, which are derived

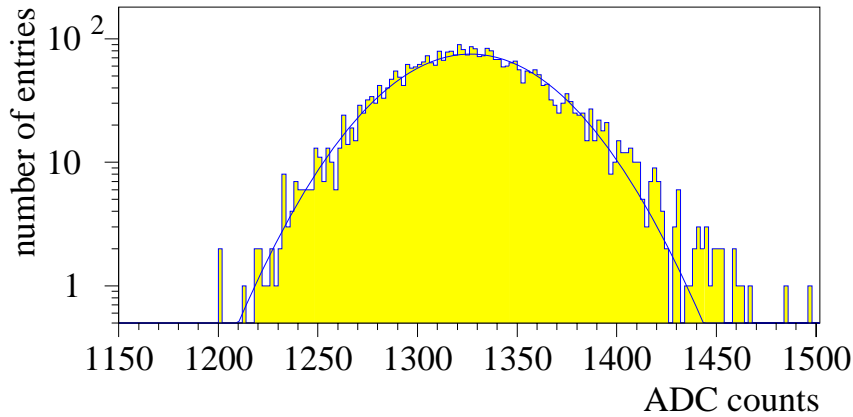


Figure 5.2: *Raw data pulseheight distribution of one strip over n events. A gaussian fit shows a width of about 37 ADC counts.*

HL	p-side	n-side
	%	
41 / 40	1.95	6.0
8 / 9	1.5	2.5
59 / 58	9.6	7.5
26 / 27	7.2	8.6

Table 5.1: *Number of saturated strips per half ladder for various half ladders.*

from a voltage reference on the hybrid. Then a method is discussed to subtract the offset from the strip pulseheight, which includes common mode subtraction and pedestal subtraction (section 5.3). With the pulseheight of each strip now centered around zero, a formula to calculate single strip noise is introduced and a technique for finding hits is briefly described. With the connection made between CST hits and H1 tracks in section 5.6 it then is possible to discuss in detail the performance of the CST in the year 1995.

5.2 Special Event Studies

The fluctuations that are due to variations in the optical readout and due to instabilities in the supply voltages can be evaluated with the help of the special events. As illustrated in chapter 4.5.3, the value of the analog voltage or the temperature on the hybrid can be calculated using eq. 4.4 and 4.5.

Fig. 5.3 shows V_{analog} , n-side. The plot indicates that the optical transmission produces very little noise (≈ 2.5 ADC counts) to be compared to the average signal width (30 ADC counts, see section 5.4). Although the distribution has a Gaussian core, there are however some entries beyond the gaussian tail. In these

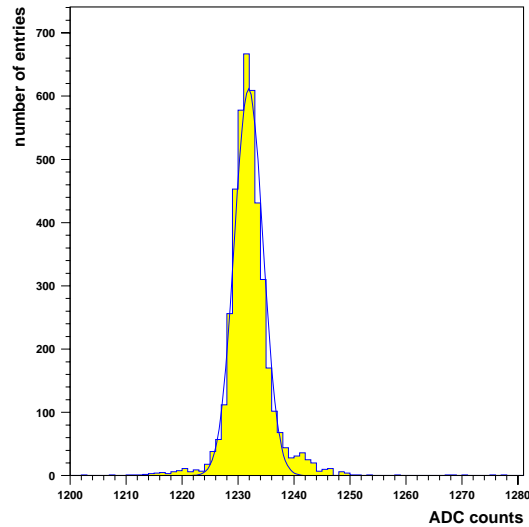


Figure 5.3: *Pulseheight distribution of special voltage V_{analog} . The small deviation from the gaussian fit on the left hand side of the distribution is due to read out errors. The width of the distribution is 2.5 ADC counts. This includes the noise from the read-out chain as well as the noise from the power supply.*

events the control sequences did not reach the decoder chip correctly and so wrong values were read out. Additionally, V_{Analog} was set wrong in some events due to this effect. Investigations show that for those events the readout of the strip data was corrupted, too, so these events are excluded from further analysis. For further raw data processing, raw data with a special event value outside four sigma of the mean value of the special events were excluded (see table 5.2).

The temperature on the hybrid varies with time. There is a warming up phase of $\approx 10 - 15$ min. after switching on the front-end electronics. There is a temperature difference between inner and outer layers of the CST due to the fact that the temperature of the inner layer was strongly correlated to the beam pipe temperature. The beam pipe is cooled by nitrogen flowing alongside it and this affects the inner layer more than the outer one. So in phases of low electron currents or when there were no beams the inner layer was $\approx 1^\circ C$ cooler than the outer layer. The average temperature measured on the hybrids in 1995 was about $45^\circ C$.

5.3 Subtraction of the Chip Offset

Each strip has an individual baseline, determined by the operating point of its preamplifier (which is influenced by detector leakage current), the serial readout

and the optical fiber readout. The noise fluctuation around the baseline shows a strong correlation between neighbouring strips. This correlated noise is called common mode and is subtracted first. The remaining offset, which is individual for each strip, is called pedestal. To subtract pedestal values for each strip separately, a mean strip value is calculated over a certain number of events. The pedestal value is therefore only sensitive to long time fluctuations. In the following two sections, common mode and pedestal subtraction are discussed in more detail.

5.3.1 Common Mode Calculation

Common mode is subtracted per APC for each event using a weight to suppress noisy channels:

$$strip_{CM\ sub}(n, i) = strip_{raw}(n, i) - \frac{\sum_{j=1}^{128} (strip_{raw}(n, j) - ped_{strip}(n-1, j)) \cdot W(n, j)}{\sum_{j=1}^{128} W(n, j)}, \quad (5.1)$$

where i = strip number, and n = event number. The common mode is calculated per APC in order to compensate gain and offset variations of the APC output amplifiers. The weight, $W(n, i) = \frac{1}{\sigma_{raw}^2(n, i)}$, and $\sigma_{raw}^2(n, i)$ is calculated to be

$$\sigma_{raw}^2(n, i) = \frac{\sum_{j=n-n_{events}}^n strip_{raw}^2(j, i)}{n_{events}^2} - \left(\frac{\sum_{j=n-n_{events}}^n strip_{raw}(j, i)}{n_{events}} \right)^2, \quad (5.2)$$

$ped_{strip}(n, i)$ is the pedestal value of strip i (see eq. 5.3), and n_{events} denotes the number of events used. All quantities are calculated for each strip.

Fig. 5.4 shows the distribution of the calculated baseline values. For the baseline distributions, like in Fig. 5.3, there are some values outside the gaussian distribution, but accumulating below and above the main distribution. For these events the distribution of the digital signals on the detector endring print did not work correctly and so the switches of the APC were not operated properly. So the number of events with readout errors depends on the position of the half ladder along the endring print. What happened was that in case for the too low values no buffers were connected to the read out ('quiet events'). The reason for the too high values ('noisy events') is not known exactly. Most probably there were two buffer connected to the read out. These events are cut out of further analysis. Table 5.2 shows the fraction of events lost due to cuts on baseline and special event.

By subtracting a common baseline, correlations between strips on the same half ladders are removed (see fig. 5.4) and a single strip monitored over many events

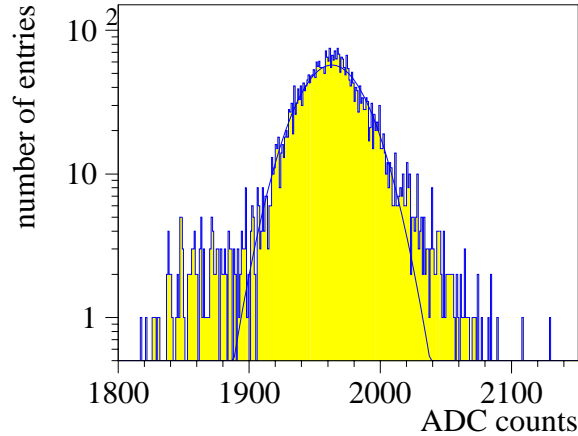


Figure 5.4: Distribution of the baseline values of all events, calculated from the n -side strip values of one APC. The gaussian fit shows a σ of 24 ADC counts. The events to the left and right side of the peak are due to faulty readout.

HL	baseline		special events	
	p-side [%]	n-side [%]	p-side [%]	n-side [%]
41 / 40	5.8	8.9	1.4	0
8 / 9	2.6	9.8	0	0.9
59 / 58	10.1	10.3	0	0
26 / 27	7.6	10.3	0	0

Table 5.2: Number of events rejected for analysis due to a 4σ cut on the baseline or on the special events for various half ladders.

shows a gaussian distribution with a 10 to 30 % reduction on the signal width, depending on the half ladder.

In the following, the possible sources of common mode are investigated in more detail.

Data are most sensitive to pick up before being amplified. This leaves the bias voltage and the analog supply voltage as most probable sources of common mode. Common mode is the same for all strips with the same supply voltages. This can be seen in Fig. 5.6, where the correlation of the chip-wise calculated common mode is shown for chips situated on two different half ladders.

Fluctuations of the bias voltage have a direct effect on the signal height: The fully depleted detector behaves like a capacitor, where fluctuations in the bias voltage induce charge which is collected on the strips and is read out. During the sample phase, where the preamplifier is connected to the detector-strips, fluctuations on the analog voltage result in a shift of the operation point of the preamplifier and translate into a shift at the input. During the re-read phase, the detector is disconnected from the analog input, and noise on the analog supply voltage translates directly to a shift

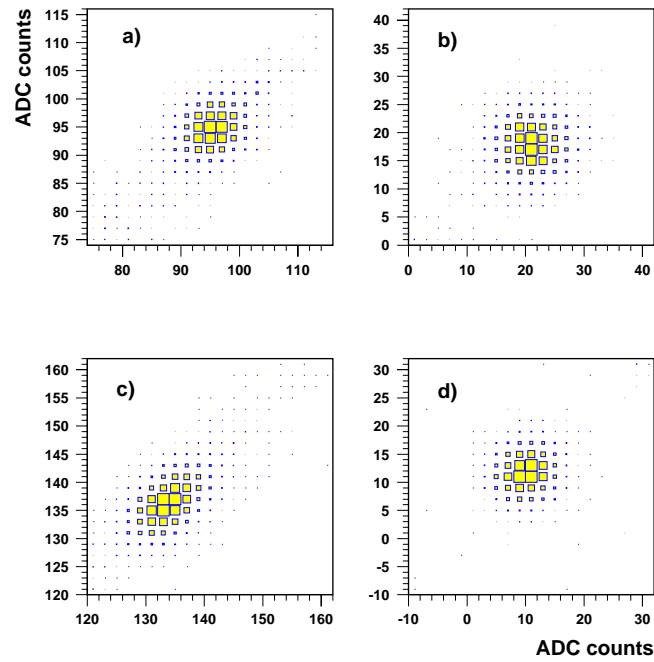


Figure 5.5: Correlation between neighbouring strips for p-side (a,b) and n-side (c,d). a) and c) show raw data, b) and d) show the data after subtraction of the common baseline. Subtraction of the baseline on an event by event basis removes the correlations between strips. Neighbouring strips show a slight anticorrelation.

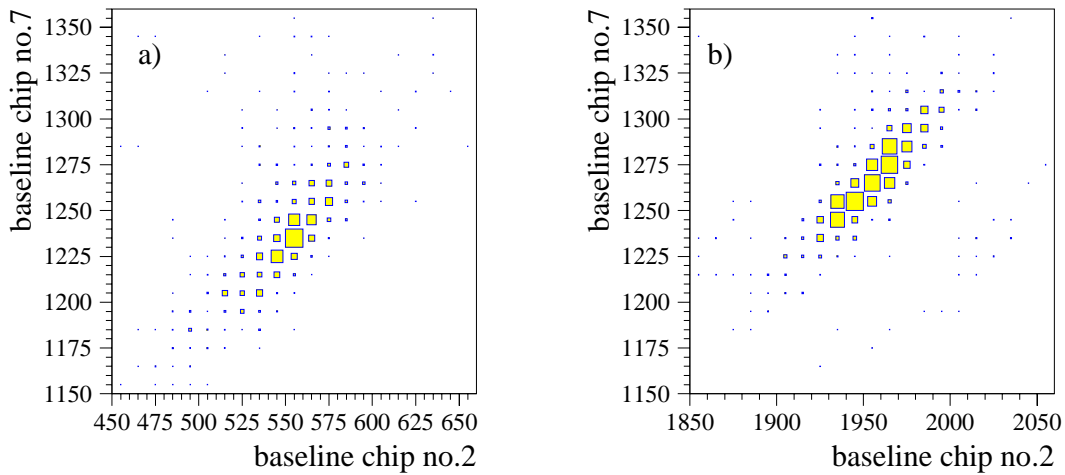


Figure 5.6: Correlation between two chips from neighbouring half-ladders for p-side (a) and n-side (b).

in the operation point and thus to a shift in the signal height. An upper limit on

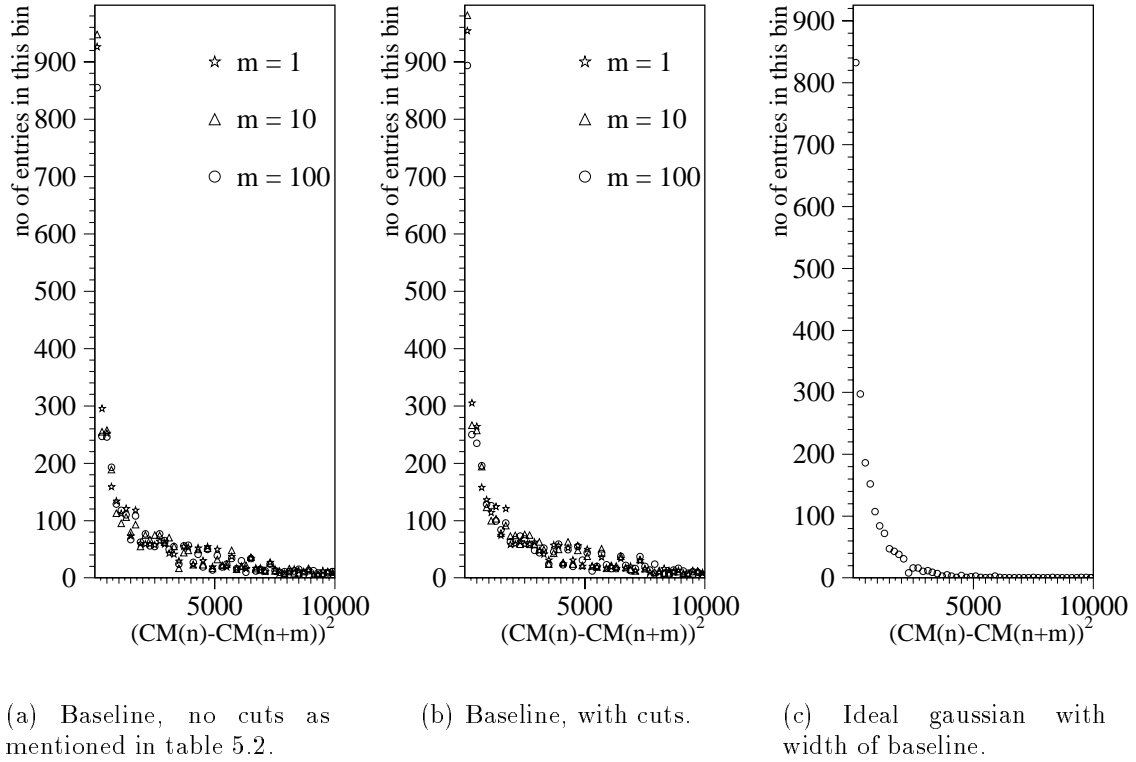


Figure 5.7: *Correlations between different events, calculated for one detector. There is shown the baseline of event $m+n$ subtracted from the baseline of event n , squared. In case of time dependent common mode, the form of the distributions should change with the time scale m . The form of the distribution can partially be explained by the Gaussian form of the baseline distribution. There is, however, a tail of the distribution seen in picture (b), which cannot be explained by the assumption of a Gaussian distribution.*

the effect of noise from the analog voltage on the analog signal can be estimated by using the width of the analog voltage as monitored by the special events readout. The equivalent noise charge then can be calculated as a shift of the working point of the preamplifier multiplied by the detector capacity to ground. With the analog voltage being monitored as $V_{ana} = 1.89 V \pm 0.4 mV$ (special event read out) and the capacity to ground being about 10 % of the total strip capacitance, the equivalent noise charge can be calculated to $ENC \approx 0.5 fC$. So, as an upper limit, noise on the analog supply voltage translates in a change of the signal height on the analog input which is in the order of 15 % of the signal height, where:

$$1 \text{ MIP (minimum ionizing particle) } \approx 22000 e = 3.5 fC.$$

During the re-read procedure, the detector is disconnected, and so noise on the analog voltage directly results into a change in signal height. In this case, the fluctuation on the signal is less than 5 % of the signal height for a *MIP*

($C_{preamplifier} \approx 0.5 \pm 0.05 \text{ pC}$).

Investigating the correlation between common mode of different events shows, that the difference $((baseline(n) - baseline(n+m))^2)$ is not depending on the time scale m . This means that the calculated baseline per event is not drifting with time (see fig. 5.7), which can be seen as well by looking at its time dependence directly.

5.3.2 Pedestal Subtraction

Each strip has its own offset value, called pedestal value. Slow fluctuations in time are not taken into account by common mode subtraction.

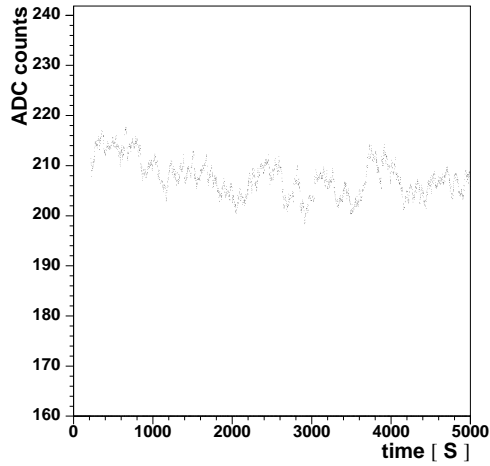


Figure 5.8: *Development for the pedestal values of one channel with time.*

Pedestal values can drift with time (see fig. 5.8), therefore it is important to have a continuous update of the pedestal subtraction:

$$\begin{aligned}
 PED(n, i) = (1 - \epsilon) \cdot \sum_{j=n-50}^{n-1} strip_{CM\ sub}(j, i) \\
 + \epsilon \cdot strip_{CM\ sub}(n, i) \quad (5.3)
 \end{aligned}$$

with $\epsilon = \frac{1}{n_{events}}$; $i = 1 \dots 1280$; n_{events} = last 50 events. The number of events used was varied between 30, 50 and 150, but more than 50 events proved to have no influence on σ or $PED(n, i)$.

5.4 Noise

The noise of each strip can be calculated according to formula 5.4.

$$\sigma(n, i) = \sqrt{\frac{\sum_{j=1}^{n_{events}} strip_{CMsub}^2(j, i)}{n_{events}^2} - \left(\frac{\sum_{j=1}^{n_{events}} strip_{CMsub}(j, i)}{n_{events}} \right)^2} \quad (5.4)$$

Fig. 5.9 shows the noise distribution for all strips read out in mV. The majority of strips has a noise value of 10 mV which corresponds to 30 ADC counts. However there is a large tail towards higher values of σ . To understand this, one has to look for the various contributions to noise separately.

Fig. 5.10 shows σ for each strip for three chips, both p- and n-side in units of ADC counts. With the help of the special events the equivalent noise in mV on the hybrid can be calculated.

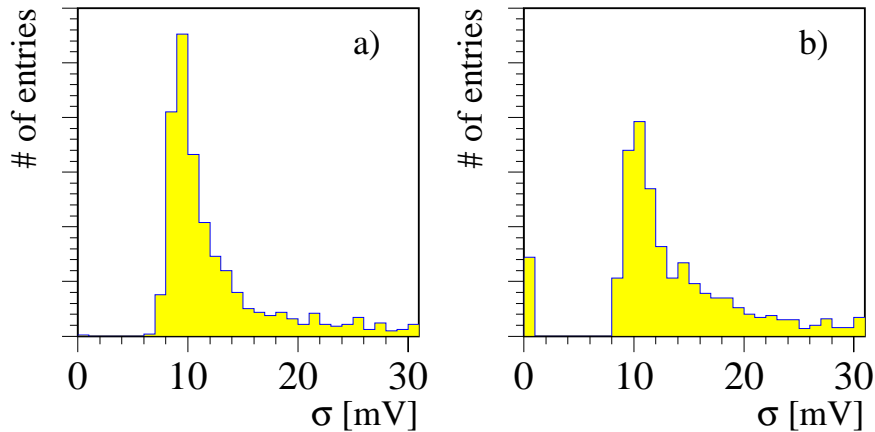


Figure 5.9: Noise (σ) distribution for all strips of one HL pair (1280 strips), p-side (a) and n-side (b). For both p-side and n-side the most probable value is ≈ 10 mV (30 ADC counts). The contributions at zero come from strips with overflow and from saturated strips.

Noise from the APC

First there is the noise coming from the various components of the APC, like preamplifier, switches and read out amplifier.

A non negligible factor for the '95 data analysis is the fact that it was not possible to calculate buffer dependent pedestals, since the number of the buffer read out was not stored with the event. Pedestal values for one strip had to be calculated as a mean over all buffers. So fluctuations within buffers of the same channel appear as

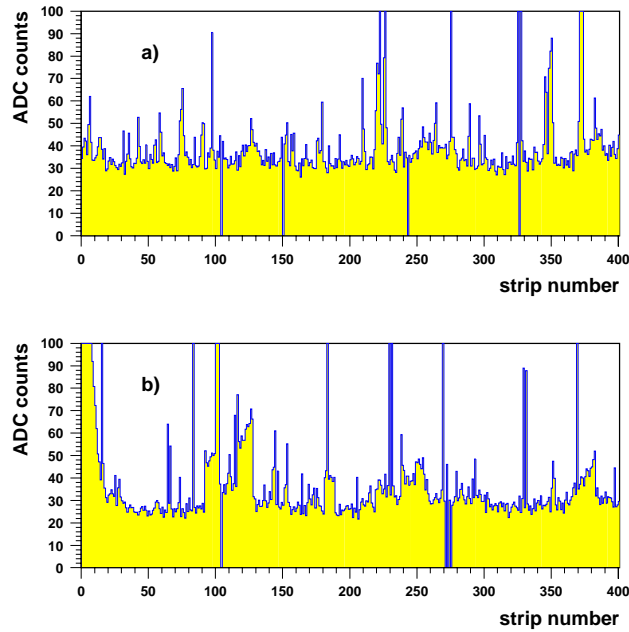


Figure 5.10: *Noise for each strip for one event, shown for p-side (a) and n-side (b) for the first 400 strips of one read out module.*

noise in the data. The buffer variations are worse for buffers at the chip borders. This shows up as a rise in the σ at the chip edges in the plot for the noise calculated for each channel (fig. 5.10) and leads to the tails in the distributions in fig. 5.9. For channels with overflow in the ADC no σ could be calculated. There are several strips with very high variations. These strips have very high, fluctuating leakage current, which creates instability. It is expected to become a much more uniform distribution once single buffer pedestals can be calculated and water cooling is available.

Noise from the Read-Out Chain

The fluctuations that are due to variations in the optical read out can be evaluated with the help of the special events. As shown in fig. 5.3 a fixed control voltage on the hybrid has a width of less than 3 ADC counts after read out through the optical chain.

The fluctuations due to variations in the digitisation inside the ONSIROC amount to less than 2.7 ADC counts [58].

It can be stated that the noise due to read out and digitisation has very little contribution compared to the noise of one channel, which is of the order of 30-40 ADC counts.

Noise from p-side and n-side by comparison

The noise distributions of p-side and n-side have 9.5 mV and 11 mV as most probable value, with the n-side distribution having a slightly larger width (see fig 5.9). According to eq. 4.3, a higher noise value for the n-side is expected due to the larger capacitive load C_{Ld} . The noise ratio $N(p)/N(n)$ can be calculated with the help of eq.4.3 to be

$$\frac{N(p)}{N(n)} = \frac{700 + 50 \cdot 27}{700 + 50 \cdot 57} \cdot \frac{90 + 57}{90 + 27} = 1.38$$

Here the second term in the equation is due to the influence of the Miller capacity on the input charge of p- and n-side, as given in eq. 4.2. Calculating the ratio with the help of fig. 5.9 yields a ratio of $N(p)/N(n) = 1.16$.

The result of the theoretical calculation is strongly influenced by the slope of the noise term. The measured result suggests this term to be slightly too high.

5.5 Hit Finding

Formula 5.5 calculates the common mode and pedestal subtracted strip contents:

$$PH(n, i) = strip_{(CM+PED)sub}(n, i) = strip_{CMsub}(n, i) - PED(n, i), \quad (5.5)$$

where CM is calculated according to 5.1 and $PED(n, i)$ as shown in 5.3. In the following the index n , indicating the event number, is omitted. Using 5.5, an event which is hardly visible in the raw data, becomes a nice peak in the common mode- and pedestal subtracted data (see fig. 5.11). Having achieved a uniform data sample where it is possible to recognise hits, a cluster finding algorithm has to be applied for hit-finding: The algorithm loops through all strip data of one event and compares the 'fluctuation' $F(i)$ of one strip to a strip-threshold:

$$F(i) = \frac{PH(i)}{\sigma(i)} = \frac{strip_{(CM+PED)sub}(i)}{\sigma(i)}, \quad i = 1 \dots 1280. \quad (5.6)$$

If one strip or several adjoining strips are above this strip threshold, they are recognized as a cluster. If the total pulseheight of this cluster is above a certain cluster-threshold, the cluster is acknowledged as a 'hit'. The thresholds for cluster finding are optimized in a tradeoff between efficiency and purity (see Chapter 5.7). Several combinations were tried, and because of the different signal heights for p-side and n-side the hit thresholds and the cluster thresholds were chosen differently for p- and n-side.

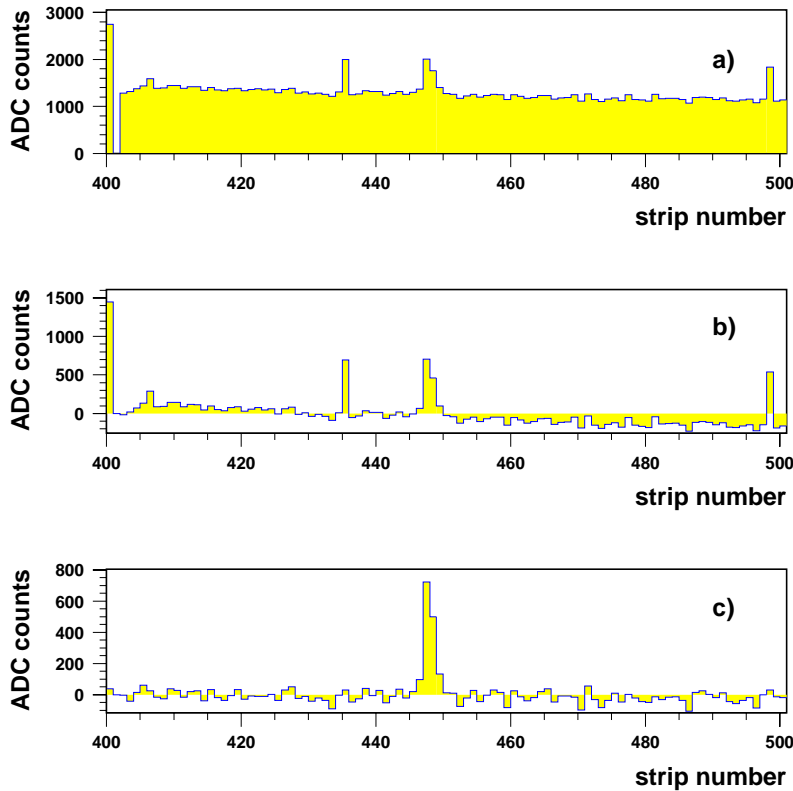


Figure 5.11: *Typical hit in raw data (a), common baseline subtracted data (b) and common baseline and pedestal subtracted data (c).*

5.6 Connection between CST Hits and H1 Tracks

Since the purpose of the CST is to increase the track resolution of the H1 tracking system, the ‘hits’ inside the CST have now to be linked to particle tracks recognized by the tracking chambers (see chapter 1). The tracks which are used in this case are tracks fitted to a common event vertex.

First of all it has to be proven that the hits found in the CST are hits caused by real particles traversing the detector and can be linked to tracks which represent the same traversing particle. This means it has to be shown that the linking which has to be done later will link real hits and not noise hits most of the time. This can be checked by producing a histogram where the distance between the position of *any* hit on a CST half ladder and the position of a particle track passing this half ladder is entered (see sketch in fig. 5.12). For this a good quality track, being recognized in the outer layer, is required. Then, for the inner layer, for all events where only one track is going through one half ladder, the histogram (fig. 5.13) is filled with as many entries as there are hits on this certain half ladder.

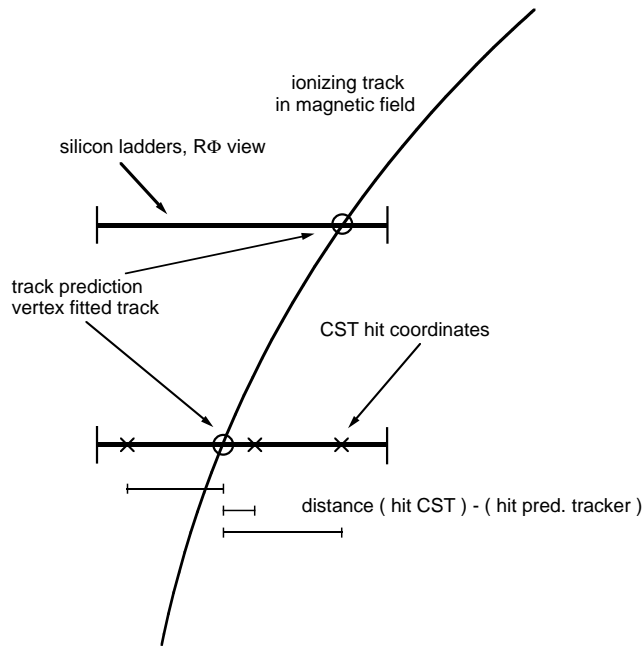


Figure 5.12: Sketch for producing a 'hit CST - hitprediction' distribution

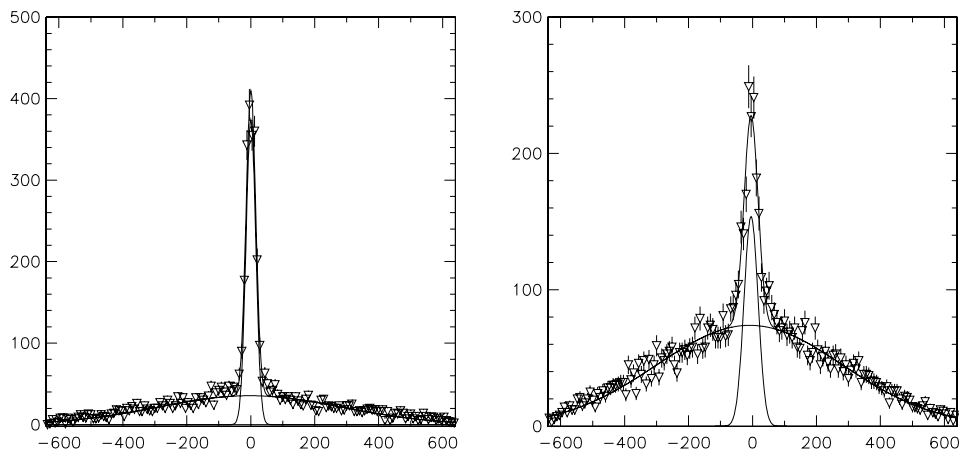


Figure 5.13: Distribution of the distance between any CST cluster and the track impact point for *p*-side (left) and *n*-side (right). The unit is in strip numbers, which gives $55 \mu\text{m}$ per unit for the *p*-side and $88 \mu\text{m}$ for the *n*-side. Thus the width of the distributions are 0.7 mm and 1.9 mm , respectively, which mirrors the resolution of the tracker. These resolutions were obtained using vertex fitted tracks. The combinatorial background on the *n*-side is higher due to a lower threshold for hit-finding.

To avoid assignments to the wrong half ladders, the track position is required to be inside the half ladder sensitive area within 2 units of the track error.

Most of the time there is among the hits on the half ladder one CST hit which

belongs to the track. The width of the distribution reflects the resolution of the trackers (the resolution of the CST is at least a factor of ten better: $\sigma_{r\phi}$ of the CJC being about $700 \mu m$). The displacement of the mean value from zero is given by the misalignment of the CST with respect to the tracking system. In the case of having only noise hits, there should be no distinct peak at zero, but a very broad peak with the mean value sitting at zero and declining to the end of the detectors. This is because the requirement of the track being well inside the sensitive volume gives a preference to hits in the center. Thus a triangular shape is expected (see fig. 5.14). The same shape of course is expected as background in case of having a real track going through the half ladder, because apart from the right combination there are noise hits, too.

Having thus verified the functioning of the detector, it is necessary to link the CST hits to those tracks which are produced by the tracking system and are fitted to the event vertex. This is done in a fit procedure using the method of the elastic arms [60].

When associating p-side hits with n-side hits, an additional difficulty arises due to the 3-fold ambiguity. As can be seen in fig. 4.7, one strip of the three detector each are bonded together and are read out by the same APC channel. This complicates the linking procedure, since there are always three possibilities where the track could have traversed the detector.

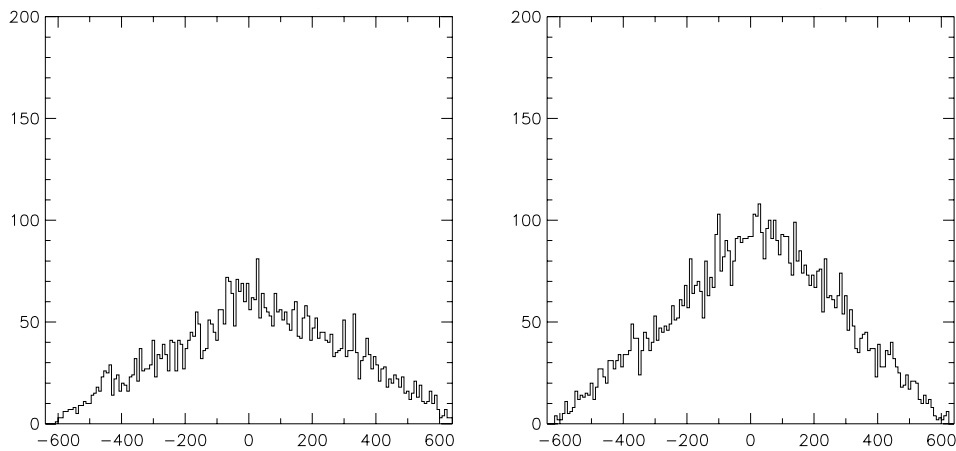


Figure 5.14: *Distribution of the distance between any CST cluster and the track impact point for both p-side (left) and n-side (right) for wrong combinations. An arbitrary track position is assumed in a half ladder with no track passing through. This arbitrary track position is then subtracted from the hits in the silicon in the same way as described above.*

5.7 Performance of the CST

One of the essential performance parameter of a detector is the signal to noise ratio. According to formula 4.3, the signal to noise ratio should be about 11 : 1 for the p-side ($C_{Ld} = 27 pF$) and about 6 : 1 on the n-side ($C_{Ld} = 57 pF$), provided there are no other sources of noise. A way of obtaining the signal to noise ratio is to enter the pulse heights of all linked CST hits into a histogram. The pulse height of the hits of particles going through the CST forms a distribution which corresponds to the energy loss of particles in thin layers of material. In case not only real linked hits are filled into this histogram, the distribution consists of two parts. The Landau distribution reflects the energy loss in matter, and an exponential distribution at lowest energies shows the pulse heights of the hits caused by noise in the CST. The lower part of the distribution is suppressed by cluster-threshold and hit-threshold cuts. The fit used to extract the most probable value uses a Landau distribution convoluted with a gaussian to take care of the variations in the pulse height of the single entries. The most probable values are found to be 110 mV (330 ADC counts) for the p-side and 42 mV (126 ADC counts) for the n-side.

With the help of the special events pulse height values have been converted from ADC counts in the OnSiROC into mV on the hybrid to get a realistic idea of the actual pulse heights.

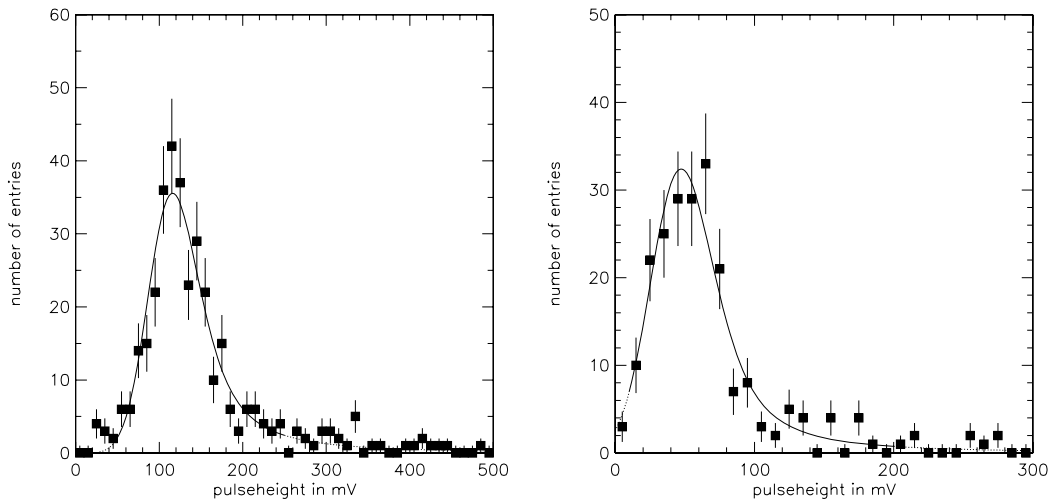


Figure 5.15: *Pulseheight distributions for all linked hits, for p-side (left) and n-side (right), corrected to $\theta = 90^\circ$ (normal incidence).*

With the help of the Landau- and the noise distribution, the signal to noise ratios for '95 data are calculated to be 11:1 for the p-side and 4:1 for the n-side. Both values are averages over all track impact angles θ , but corrected to $\theta = 90^\circ$. The value for the n-side is below the theoretically possible value. One possible explanation is, that on the n-side, the rise time of the signal is slower due to the larger input capacitance. This can lead to a reduction in the signal height, but is not the dominant effect.

A second source of signal loss is the cluster algorithm. By applying the cluster algorithm to n-side tracks with a large track impact angle θ , not all strips which contribute to a cluster are recognized, because of the flat charge distribution of the cluster. This means, that the loss of signal on the n-side is mainly due to loss of signal from shallow tracks. For further discussion see the comments to fig. 5.16.

The second important parameter is the efficiency of the detector. The efficiency is defined as follows:

$$\epsilon = \frac{\text{number of hits in the CST linked to penetrating tracks}}{\text{total number of tracks going through the CST}}. \quad (5.7)$$

where with CST, here there is meant the sensitive area of the CST. The efficiency is closely correlated to the hit finding. If very low thresholds for the hit finding are chosen, most 'real' hits are found and thus the efficiency is high. But at the same time the number of 'noise' hits is increasing and the probability that a noise hit near a track position is found increases. This leads to wrong links between tracks and CST hits. To investigate this, the same procedure as above is performed, but by selecting an arbitrary track position for a detector where no track was found to pass through. Since this method is a measure for the quality of the track linking, the resulting value is called purity: The lower this number is, the fewer noise hits are linked. The purity p of the calculated efficiency numbers given is thus expressed as:

$$1 - p = \frac{\text{number of links which are found}}{\text{number of arbitrary chosen coordinates going through a half ladder}}. \quad (5.8)$$

So in case there are no noise hits this number should be near 0 because only 'real' hits are linked. But the efficiency calculated with formula 5.7 is overestimating the actual efficiency, since it includes the number of accidentally linked noise hits as well. At the same time, the number given for the purity is too high, since in reality there is a competition between real hits and noise hits. But since it is not known, which hit is true and which hit is noise, the two effects can not be unfolded with the given data sample. The desired 'real' efficiency would be:

$$\epsilon \cdot p = \frac{\text{number of true hits in the CST linked to penetrating tracks}}{\text{total number of tracks going through the CST}}. \quad (5.9)$$

Table 5.3 shows the efficiencies and the purity numbers of the CST hit finding for p- and n-side with different cuts on the hit- and cluster-threshold for the '95 data. The true efficiency numbers according to formula 5.9 can either be calculated with

monte carlo data, since there the real hits are known, or using tracks from cosmic particles traversing the whole CST, so that two hits can be used to define the track, leaving two hits to calculate efficiency with. There are several reasons for the

detector side	hit threshold in units of σ	cluster threshold in units of σ	efficiency in %	1 - p in %	purity in %
p-side	2	5	87	5	95
n-side	1	4	41	13	87
p-side	1	5	89	27	73
n-side	1	3	54	31	69

Table 5.3: *Hit finding efficiency and purity for p-side and n-side in dependence of the thresholds used in the cluster algorithm.*

inefficiencies: The most frequently occurring problem was the improper distribution of the digital control signals to the decoder chips on the hybrids. Mistakes occurred at two stages. The first one was the sequencer of the OnSiROC. This sequencer had several faults. Most of these faults were discovered during the year, but some remained and were only discovered and fixed after the shutdown, so that the data taken were inefficient due to faulty sequences coming from the OnSiROC sequencer. This kind of error occurred in about 6 to 7 % of all events. The second stage was the detector ending print. As described in chapter 3 the distribution of the digital signals on the ending print sometimes did not work properly and so the decoder chips were loaded with the wrong sequences. It is very difficult to state how many events were affected by this problem, but it is assumed that the 'ending print' problem can be blamed for most of the inefficiency observed on the p-side.

There is an additional effect which leads to considerable loss in efficiency, especially on the n-side: An ionizing particle traversing the detector creates electron hole pairs along its track. Assuming an undistorted electrical field in the silicon, the electrons and holes drift along lines to the readout strips.

Therefore the silicon cluster pulseheight is expected to increase with the signal path length, since more silicon material is traversed and more charge is created. The resulting pulseheight is proportional to $\frac{1}{\sin\theta}$, where θ is the angle of the track with respect to the z -axis. Fig. 5.16, left picture, shows the cluster pulseheight multiplied by $\sin\theta$ versus θ for the linked tracks of p- and n-side. As expected, on the p-side the pulseheight rises with rising angle θ , which gives a flat distribution. On the n-side, the resulting curve has a triangular shape. This can only be explained by the fact that a large amount of charge (up to 50 %) in the cluster is not collected for tracks with $\theta \neq 90^\circ$.

For $\theta = 90^\circ$, a ratio $\text{signal(p-side)}/\text{signal(n-side)}$ can be calculated. This ratio yields $\text{signal(p)}/\text{signal(n)} = 1.39 \pm 0.09$. This is in agreement with the value which is expected by using eq. 4.2, 1.26.

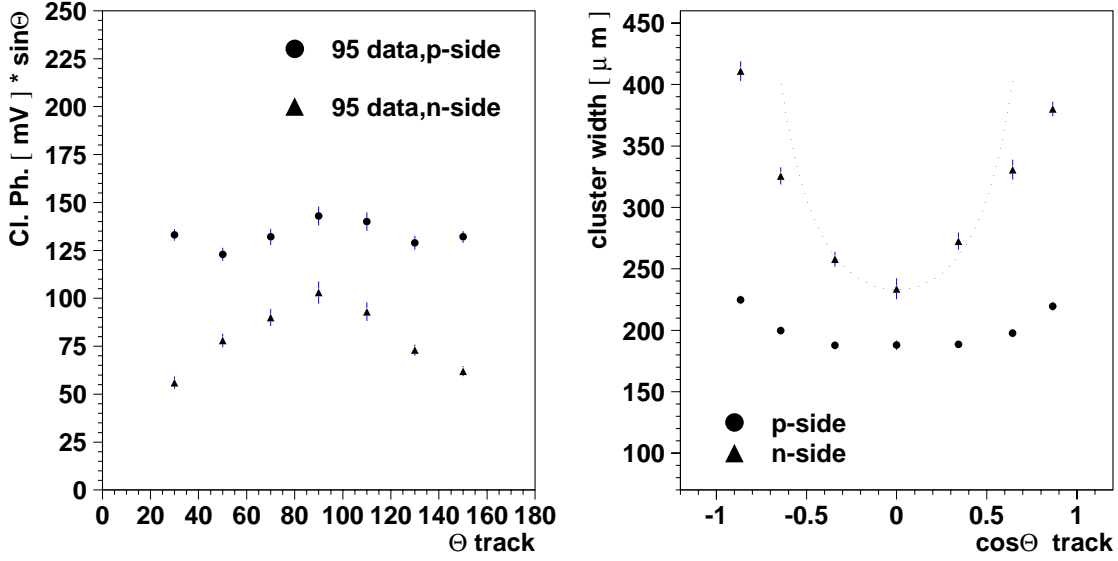


Figure 5.16: *Cluster pulseheight (left picture) and cluster width (right picture) versus track impact angle theta. For the cluster width on the p-side, the errors on the measurements are of the same size as the points (2-3 %).*

The signal to noise ratio at $\theta = 90^\circ$ can be calculated to S/N (p-side) = 11.6 ± 0.24 and S/N (n-side) = 7.2 ± 0.4 . These signal to noise ratios at $\theta = 90^\circ$ are better than could have been expected from calculation and suggest again that formula 4.3 has a slightly too high noise term.

This results imply, that the low efficiency and the low signal to noise ratio on the n-side are traced back to particles traversing the silicon wafers at $\theta \neq 90^\circ$. An illustration to the problem of inefficient charge collection at $\theta \neq 90^\circ$ is given in fig. 5.16, right picture. Here the width of a cluster in the silicon sensors versus the track impact angle theta is plotted: The cluster width is smallest for tracks traversing the silicon at an angle $\theta = 90^\circ$. The shallower the tracks are, the wider the cluster is. Since theta is perpendicular to the $r\phi$ coordinate, the track traverses the silicon along the $r\phi$ strip and the effect is small on the p-side. On the n-side the track passes an increasing number of strips with increasing angle. So the charge is spread over an increasing number of strips. Due to the very low signal to noise ratio on the n-side and the flat charge distribution over many strips, either the cluster is not recognized any longer (lower efficiency on the n-side), or only part of the strips which contribute to this cluster are found (cluster pulseheight on the n-side lower than expected).

Taking into account the geometrical impact only, the cluster width is a function of $\frac{1}{\text{tg}\theta}$:

$$\text{clusterwidth}(\theta^\circ) = \sqrt{\text{clusterwidth}^2(\theta = 90^\circ) + \left(\frac{\text{detector thickness}}{\text{tg}\theta}\right)^2}.$$

The dotted line in the histogram represents this function.

In the range $60^\circ < \theta < 120^\circ$ there is good agreement between the measured points and the geometrical prediction. For shallower angles, not all strips belonging to a cluster are found, thus resulting in a loss of pulseheight per cluster. Both plots in fig. 5.16 indicate, that the reason for the low signal to noise ratio obtained from fig. 5.15 can be explained by the loss of signal on the n-side from shallow tracks.

5.8 Conclusions

The lower half of the central silicon tracker has been installed in the H1 experiment at HERA in the shutdown 1994/95, thus being the first silicon vertex detector operated at an ep-collider.

In particular, all modules which have been installed have proved to be fully operational. This high reliability of the detector system is mostly due to very intensive testing of all single components and of the finished modules before installation. In the end of 1995, out of more than 80000 wire bonds, only 3 bonds had to be renewed.

Data analysis shows, that the detector can be operated in the HERA environment and close to the beam line, and that the inefficiencies are understood. In particular, those inefficiencies due to sequencer code and detector endring print were removed in 1996 and 1997 and the readout errors disappeared.

The signal to noise ratio and the efficiency can be further improved by using double or triple subtraction of the APC buffers, a technique which is successfully applied in 1997.

In 1997, online hit finding code was installed to reduce the raw data volume. This code is based on the experience gained in offline studies on raw data processing and hit finding. So, with further alignment being done in 1997, the CST is now collecting data to be used for physics analysis.

Fig. 5.17 shows an event as measured by the CST in 1997. The CST linking is performed including global alignment of the CST within H1. Presently, a routine is being developed to include the CST position measurements in the vertex fit.

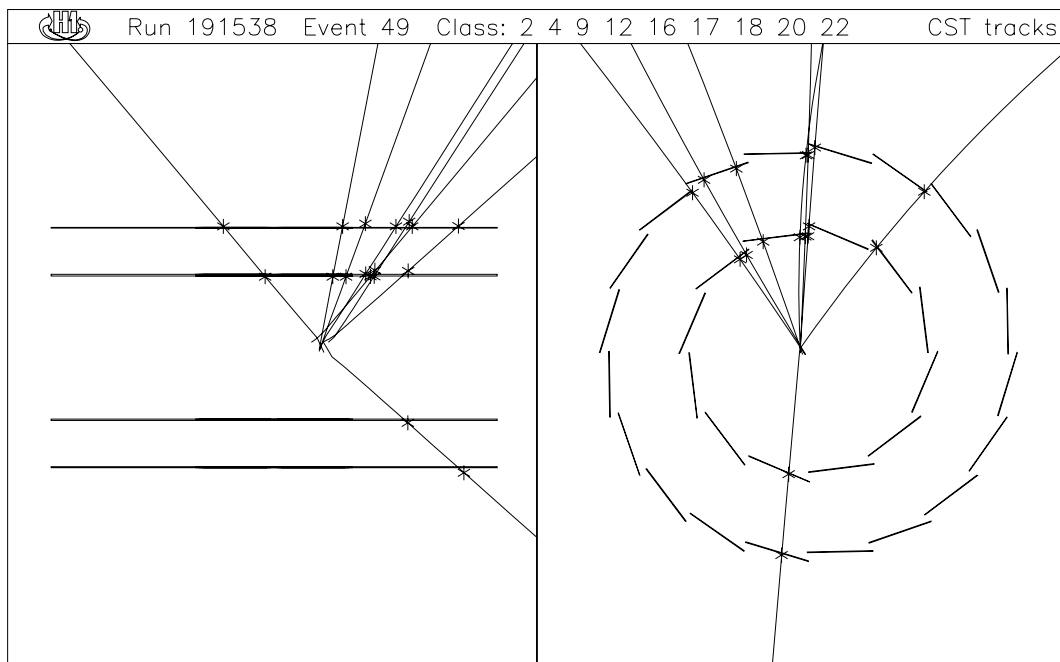


Figure 5.17: *Eventdisplay of a deep inelastic scattering event as measured by the CST in 1997. The left side shows the projection in z (horizontal axis), the right picture shows the $R\phi$ projection. In z as well as in $R\phi$, all tracks from the central tracking chamber could be linked to CST hits. Not shown are tracks which go into the forward direction, thus missing the CST, and noise hits.*

List of Figures

1.1	<i>The HERA ring collider at DESY in Hamburg. The Experiment H1 is situated in the north section of the ring.</i>	7
1.2	<i>Example of the proton bunch structure as measured by the H1 FTOF system. The horizontal axis shows the time scale in ns, the vertical axis shows the number of hits in the FTOF system. The main peak refers to the protons in the main bunches, the peaks left and right show the (5ns) satellites.</i>	9
1.3	<i>Picture of the bunch population in HERA. The horizontal axis shows the bunch number and the vertical axis the current per bunch in μA.</i>	9
1.4	<i>Kinematics of the ep scattering at HERA</i>	10
1.5	<i>Three dimensional picture of all detector components in the main H1 detector as of 1994. H1 components situated in the HERA tunnel down(backwards) the beam lines are shown in a separate picture.</i>	16
1.6	<i>Layout of the luminosity system downstream (backward) of the H1 experiment.</i>	17
1.7	<i>Acceptance of the electron tagger at 44 m. The different curves represent different run ranges with different electron beam tilts.</i>	19
1.8	<i>Side view of the central tracking of H1.</i>	21
1.9	<i>x-y view of a phi-section of the central jet chamber.</i>	22
2.1	<i>Feynman diagram of the boson gluon fusion, producing a $c\bar{c}$ pair.</i>	27
2.2	<i>Example of a Feynman diagram of the hadronic component of the boson gluon fusion producing a $c\bar{c}$ pair in lowest order.</i>	28
3.1	<i>Δm distribution, for D^*s from all subtriggers (a) and for D^*s triggered by subtrigger 84 (b), both pictures after applying the analysis cuts.</i>	35
3.2	<i>Δm distribution, for events triggered by ST 84. The solid line represents the wrong sign combinatorial background, the fitted curve is obtained using eq. 3.7.</i>	37
3.3	<i>The total γp cross section as a function of W. Shown are results from H1 and ZEUS in the high W region and results from fixed target experiments covering the low W range.</i>	40

- 3.4 *Distribution of the transverse momentum of the D^* -mesons from photoproduction events. Shown is the visible differential cross section $d\sigma^{vis}(\gamma p \rightarrow c\bar{c}X)/dp_t$ for $-1.5 < \eta < 1.5$ and $0.04 < y < 0.24$ in bins of p_t . The results are given with statistical errors and those systematical errors which depend on p_t . Not included are $\pm_{10.9}^{14.2}\%$ common systematical errors and errors due to theoretical uncertainties. The solid histogram shows the NLO QCD prediction [21], using the MRS-H proton parton density parametrisation (MRS-G : dotted histogram line) with a charm mass of 1.5 GeV , calculated at $W_{\gamma p} = 95 \text{ GeV}$ 41*
- 3.5 *Δm distributions for different bins in p_t . The points show the data, the histogram shows the wrong sign combinatorial background. The fit (solid line) was obtained the same way as for the total Δm distribution, with a fixed width of 0.9 MeV . The statistical errors include the error due to variations in the width of the Δm distribution. Fig. a) to c) show the distributions for the three different bins: a: $1.8 < p_t < 2.5$, b: $2.5 < p_t < 3.5$, c: $3.5 < p_t < 6.0 \text{ GeV}$ 42*
- 3.6 *η distribution of the D^* -mesons from photoproduction events. Shown is the visible differential cross section $d\sigma(\gamma p \rightarrow c\bar{c}X)/d\eta$ for $p_t > 1.8 \text{ GeV}$ and $0.04 < y < 0.24$. The error bars show the statistical errors and those systematical errors which depend on η . Not included are $\pm_{10.9}^{14.2}\%$ common systematical errors and errors due to theoretical uncertainties. The solid histogram shows the NLO QCD prediction, using the MRS-H proton parton density parametrisation (MRS-G : dotted histogram line) with a charm mass of 1.5 GeV , calculated at $W_{\gamma p} = 95 \text{ GeV}$ 43*
- 3.7 *Δm distributions for different bins in η . The points show the data, the histogram shows the wrong sign combinatorial background. The fit (solid line) was obtained the same way as for the total Δm distribution. The statistical errors include the error due to variations in the width of the Δm distribution. Fig. a) to d) show the distributions for the four different bins: a: $1.5 > \eta > 1.0$, b: $1.0 > \eta > 0.5$, c: $0.5 > \eta > 0.0$, d: $0.0 > \eta > -0.5$ 44*
- 3.8 *χ^2 , as given in eq. 3.12, calculated for different slope parameters λ . Each curve is calculated with one fixed value for the normalisation parameter σ_0 . For visibility reasons, not all calculated curves have been included in this plot. 47*
- 3.9 *Covariance ellipse for σ_0 and λ as obtained from fig. 3.8. A calculated point enters this histogram, if $1.6 < \chi^2 < 1.72$ 47*
- 3.10 *H1 measurements of $\sigma_{\gamma p}$, together with the fit as calculated in this analysis. The data points show $\sigma_{\gamma p}(\gamma p \rightarrow c\bar{c})$ for $-1.5 < \eta < 1.0$ and $p_t > 2.5 \text{ GeV}$ 48*
- 3.11 *Slope parameter λ of the energy dependence $\sigma_{tot} \sim W^{2\lambda}$ or $\frac{d\sigma}{dt}(\text{elastic}) \sim W^{4\lambda}$ for different types of processes. 49*

4.1	<i>Photo of the lower half of the Central Silicon Tracker.</i>	51
4.2	<i>Transverse impact parameter resolution of tracks extrapolated from the CST to the common event vertex as a function of material placed between the interaction vertex and the second layer of silicon detectors. For this calculation an intrinsic resolution of the CST detectors of $10\ \mu\text{m}$ is assumed. The solid line refers to the beam pipe in 1995, which consisted of 2 mm thick aluminium and will be replaced by a 1 mm thick Carbon Fiber Composit beam pipe with a $100\ \mu\text{m}$ thin aluminium layer (dashed line). The dotted line refers to no beam pipe at all, just the first layer of silicon detectors, which is situated at a radius of 57.5 mm.</i>	53
4.3	<i>The principle of a silicon detector.</i>	54
4.4	<i>The use of p-blocking implants for isolating n-side strips: a) shows the n-side of a depleted silicon detector with a conductive sheet due to trapped oxide charges between the strips, b) shows the ohmic charge separation of the strips by p-blocking implants.</i>	55
4.5	<i>Model of capacitive coupling in a silicon detector with intermediate strips.</i>	56
4.6	<i>Photo of the n-side of one of the CST detectors, showing an area of about $2.5 \times 3.2\ \text{mm}^2$.</i>	57
4.7	<i>Schematic view of a half ladder. The upper part of the drawing shows the p-side, the lower part the n-side of one half ladder.</i>	59
4.8	<i>Sketch of the carbon fiber end-flange with cooling pipes. The cooling pipes branch off into the balconies. On these balconies, ladders are mounted such that the hybrids are fixed on the balconies.</i>	60
4.9	<i>Sketch of part of the read out: two half ladders are connected to the end ring print. The end ring print serves as a distributor for power and control signals. Furthermore the electrical analog output signals are converted to optical signals. Outside the H1 detector, in the electronic trailer, the optical analog signals are converted back into electrical signals and digitized with fast analog to digital converters in the ONSIROC [58]. Additionally, the digital control signals from the sequenzer module, which is situated on the ONSIROC, are converted into optical signals by converter cards.</i>	61
4.10	<i>Photo of part of Detector Endring Print.</i>	62
4.11	<i>Electrical diagram of one channel of the APC chip.</i>	63
4.12	<i>Circuit diagram of the analog preamplifier of the APC 128.</i>	64
4.13	<i>Flowchart of control signals for operating the APC</i>	66
4.14	<i>Layout of the Decoder chip.</i>	68
4.15	<i>Schematic drawing of the differential input of the decoder chip.</i>	69
4.16	<i>Oscilloscope photo of clock pulse entering- and leaving the Decoder chip. The two lower lines, the triangular clock pulse (CLK +) and the line at zero (CLK -) show the decoder input signals, the upper line shows the output pulse (Sϕ 1).</i>	70

4.17	<i>Sketch of one shift register cell and the corresponding clock cycle to operate the cell.</i>	70
4.18	<i>Sketch for measuring I/V characteristics of the DAC.</i>	71
4.19	<i>I/V characteristics of the transistor used for the current supply.</i>	72
4.20	<i>Electrical circuit to measure the voltages of the special events on the hybrid. The special voltages can be connected to the analog output line using bits 49 - 56 of the decoder chip.</i>	72
4.21	<i>APC 128 bond pad layout. The overall dimensions are $3.5 \times 6.3\text{mm}^2$, and the units given in the fig. are in μm.</i>	74
4.22	<i>Decoder bond pad layout</i>	75
5.1	<i>Raw data pulse height distribution for one early and late HL-pair (a: p-side, b: n-side): Shown is the pulseheight of each strip for all 1280 strips of two neighbouring half ladders, which form one read out unit.</i>	77
5.2	<i>Raw data pulseheight distribution of one strip over n events. A gaussian fit shows a width of about 37 ADC counts.</i>	78
5.3	<i>Pulseheight distribution of special voltage V_{analog}. The small deviation from the gaussian fit on the left hand side of the distribution is due to read out errors. The width of the distribution is 2.5 ADC counts. This includes the noise from the read-out chain as well as the noise from the power supply.</i>	79
5.4	<i>Distribution of the baseline values of all events, calculated from the n-side strip values of one APC. The gaussian fit shows a σ of 24 ADC counts. The events to the left and right side of the peak are due to faulty readout.</i>	81
5.5	<i>Correlation between neighbouring strips for p-side (a,b) and n-side (c,d). a) and c) show raw data, b) and d) show the data after subtraction of the common baseline. Subtraction of the baseline on an event by event basis removes the correlations between strips. Neighbouring strips show a slight anticorrelation.</i>	82
5.6	<i>Correlation between two chips from neighbouring half-ladders for p-side (a) and n-side (b).</i>	82
5.7	<i>Correlations between different events, calculated for one detector. There is shown the baseline of event $m+n$ subtracted from the baseline of event n, squared. In case of time dependent common mode, the form of the distributions should change with the time scale m. The form of the distribution can partially be explained by the Gaussian form of the baseline distribution. There is, however, a tail of the distribution seen in picture (b), which cannot be explained by the assumption of a Gaussian distribution.</i>	83
5.8	<i>Development for the pedestal values of one channel with time.</i>	84

5.9	Noise (σ) distribution for all strips of one HL pair (1280 strips), p-side (a) and n-side (b). For both p-side and n-side the most probable value is ≈ 10 mV (30 ADC counts). The contributions at zero come from strips with overflow and from saturated strips.	85
5.10	Noise for each strip for one event, shown for p-side (a) and n-side (b) for the first 400 strips of one read out module.	86
5.11	Typical hit in raw data (a), common baseline subtracted data (b) and common baseline and pedestal subtracted data (c).	88
5.12	Sketch for producing a 'hit CST - hitprediction' distribution	89
5.13	Distribution of the distance between any CST cluster and the track impact point for p-side (left) and n-side (right). The unit is in strip numbers, which gives $55 \mu\text{m}$ per unit for the p-side and $88 \mu\text{m}$ for the n-side. Thus the width of the distributions are 0.7 mm and 1.9 mm, respectively, which mirrors the resolution of the tracker. These resolutions were obtained using vertex fitted tracks. The combinatorial background on the n-side is higher due to a lower threshold for hit-finding.	89
5.14	Distribution of the distance between any CST cluster and the track impact point for both p-side (left) and n-side (right) for wrong combinations. An arbitrary track position is assumed in a half ladder with no track passing through. This arbitrary track position is then subtracted from the hits in the silicon in the same way as described above.	90
5.15	Pulseheight distributions for all linked hits, for p-side (left) and n-side (right), corrected to $\theta = 90^\circ$ (normal incidence).	91
5.16	Cluster pulseheight (left picture) and cluster width (right picture) versus track impact angle theta. For the cluster width on the p-side, the errors on the measurements are of the same size as the points (2-3 %).	94
5.17	Eventdisplay of a deep inelastic scattering event as measured by the CST in 1997. The left side shows the projection in z (horizontal axis), the right picture shows the $R\phi$ projection. In z as well as in $R\phi$, all tracks from the central tracking chamber could be linked to CST hits. Not shown are tracks which go into the forward direction, thus missing the CST, and noise hits.	96

List of Tables

1.1	<i>Run ranges with corresponding trigger efficiency and integrated, satellite bunch, high voltage and deadtime corrected luminosity. . . .</i>	25
3.1	<i>Compilation of systematic errors contributing to $\sigma_{\gamma p}$.</i>	38
3.2	<i>Results on the differential cross sections in p_t. The results are given with statistical errors and all systematical errors. Not included are errors due to theoretical uncertainties.</i>	41
3.3	<i>Results on the differential cross sections in η. The results are given with statistical errors and all systematical errors. Not included are errors due to theoretical uncertainties.</i>	43
3.4	<i>Compilation of data necessary to calculate the visible ep and γp cross sections. The efficiency given in the table includes the trigger efficiency in the case of ET 33. For ET 44 the trigger efficiency is included in the number given for the luminosity. The numbers for $N_{rec}^{D^*}$ have been obtained for the visible range: $-1.5 < \eta < 1.0$ and $p_t(D^*) > 2.5 \text{ GeV}$, and are not corrected for the acceptances of the electron taggers. The values for acceptance and photon flux given are average values.</i>	46
4.1	<i>Summary of various reconstruction efficiencies for D^0 mesons in photoproduction with and without a vertex detector [51]. Charged particles have been confined to $\eta < 1.5$, and a vertex separation of $d/\sigma > 2.3$ has been required in the case of a vertex detector. Acceptance and reconstruction efficiencies depend on details of the analysis and only round numbers are given.</i>	52
4.2	<i>Relation between set DAC bits and output current</i>	71
5.1	<i>Number of saturated strips per half ladder for various half ladders. . .</i>	78
5.2	<i>Number of events rejected for analysis due to a 4σ cut on the baseline or on the special events for various half ladders.</i>	81
5.3	<i>Hit finding efficiency and purity for p-side and n-side in dependence of the thresholds used in the cluster algorithm.</i>	93

Bibliography

- [1] ZEUS Collaboration, M. Derrick et al., Phys. Lett. **B439** (1995) 225
- [2] HERA-B Collaboration, I. Abt et al., DESY-PRC 95/01, January 1995
- [3] M. Dueren for the HERMES Collaboration, Proc. of the XXXIst Rencontres de Moriond, QCD and High Energy Hadr. Interactions, Les Arcs, France, March 23-30, 1996, to be published
- [4] S. Levonian and A. Panitch, H1 internal note, H1-09/95-454
- [5] J. D. Bjorken and Emmanuel A. Paschos, Phys. Rev. **185** (1969) 1975
- [6] F. Halzen and A. D. Martin, Quarks and Leptons, p. 217
- [7] H1 collaboration, S. Aid et al., Z. f. Phys. **C69** (1995) 27
- [8] P. V. Landshoff, hep-ph/9410250, August 1994, Proceedings of the Zuoz Summer School on Hadronic Aspects of Collider Physics, Editor: M. P. Locher A. Donnachie, invited Talk at the Eilat Workshop on DIS and diffractive scattering, February 1994, Editor: A. Levy
- [9] Phys. Rev. D, Particles and Fields, Part 1, **D54** (1996) 191
- [10] H1 Collaboration, I. Abt et al., Nucl. Instr. and Meth. **A386** (1997) 310
- [11] H1 Collaboration, J. Bürger et al., H1 06/92-226, PRC 92/01
- [12] H1 SPACAL-Group, R. D. Appuhn et al., Nucl. Instr. Meth. A374(1996) 149
- [13] H1 Collaboration, Technical Proposal, PRC 93/02, March 8, 1993
- [14] W. Eick et al., Nucl. Inst. Meth. **A386** (1997) 81
- [15] H1 Collaboration, T. Ahmed et al., DESY-95-024 / Z.Phys. **C66** (1995) 529
- [16] V. Andreev, H1 internal report, H1-10/96-493
- [17] W. Erdmann, Ph.D. thesis, ETHZ-IPP internal report 96-1
- [18] J. Riedlberger, Nucl. Phys. **B** (Proc. Suppl.) **44** (1995) 423

- [19] T. Wolff et al., Nucl. Inst. Meth. **A323** (1992) 537
- [20] S. Eichenberger et al., Nucl. Inst. Meth. **A323** (1992) 532
- [21] S. Frixione, P. Nason and G. Ridolfi, Nucl. Phys. **B454** (1995) 3
S. Frixione, M. L. Mangano, P. Nason and G. Ridolfi, Phys. Lett. **B348** (1995) 633
- [22] Phys. Rev. D, Particles and Fields, Part 1, **D54** (1996) 189
- [23] S. Frixione, M. L. Mangano, P. Nason, G. Ridolfi, CERN-TH-97-16, Feb 1997 100pp, e-Print Archive: hep-ph/9702287, to be published in Heavy Flavours II, Editors: A. J. Buras and M. Lindner, World Scientific
- [24] C. F. Weizsäcker, Z. Phys. **88** (1934) 612,
E. J. Williams, Phys. Rev. **45** (1934) 729
- [25] S. Frixione et al. Phys. Lett. **B319** (1993) 339
- [26] M. Glück, E. Reya and A. Vogt, Phys. Rev. **D45** No.11 (1992) 3986
- [27] S. Frixione, M. L. Mangano, P. Nason and G. Ridolfi, Phys. Lett. **B348** (1995) 633
- [28] A. Levy, H. Abramovicz and K. Charachula, Phys. Lett. **B269** (1991) 458
- [29] M. Arpagaus, Ph.D. thesis, ETHZ-IPP internal report 94-2
- [30] R. K. Ellis, P. Nason, Nucl. Phys. **B312** (1989) 551
- [31] Phys. Rev. D, Particles and Fields, Part 1, **D54** (1996)
- [32] G. J. Feldmann et al., Phys. Rev. Lett. **38** (1977) 1313
- [33] ALEPH Collaboration and DELPHI Collaboration and L3 Collaboration and OPAL, Nucl. Inst. Meth. **A378** (1996) 101
- [34] JETSET, T. Sjöstrand, Comp. Phys. Com. **39** (1986) 347
T. Sjöstrand and M. Bengtson, Comp. Phys. Com. **43** (1987) 367
PYTHIA, M. Bengtson and T. Sjöstrand, Comp. Phys. Com. **46** (1987) 43
- [35] G. Ingelman, J. Rathsman and G.A. Schuler, Comp. Phys. Com. (1997) 101-135-142, hep-ph/9605285
- [36] M. Glück, E. Reya and A. Vogt, Z. f. Phys. **C53** (1992) 127
- [37] B. Anderson, G. Gustafson, G. Ingelmann and T. Sjöstrand, Phys. Rev. Rep. **97** (1983) 33
T. Sjöstrand, Comp. Phys. Comm. **27** (1983) 243, **28** (1983) 229

-
- [38] A. D. Martin, W. J. Stirling and R. G. Roberts, *Phys. Rev.* **D50** No.11 (1994) 6734
- [39] M. Goossens, CERN Program Library Long Writeup W5013
- [40] S. Aid et al., H1-Coll., *Nucl. Phys* **B472** (1996) 32
- [41] A. D. Martin, W. J. Stirling and R. G. Roberts, *Phys. Lett.* **B354** (1995) 155
- [42] A. Donnachie and P. Landshoff, *Phys. Lett.* **B296** (1992) 227,
H. Cheng, J.K. Walker and T.T. Wu, *Phys. Lett.* **B44** (1973) 97
- [43] H1 Collaboration, S. Aid et al., *Nucl. Phys.* **B468** (1996) 3
- [44] H1 collaboration, C. Adloff et al., hep-ex/9703012, DESY 97-042, March 1997
- [45] H1 Collaboration, S. Aid et al., *Z. f. Phys.* **C70** (1996) 609
- [46] J. Moeck, H1 preliminary, paper to be submitted to the HEP '97 conference, Jerusalem
- [47] S. Schiek, Ph.D. thesis, Internal Report, DESY F11/F22-97-01, February 1997
- [48] H1 Collaboration, S. Aid et al., *Phys. Lett* **B392** (1997) 234
- [49] H1 Collaboration, T. Ahmed et al., *Nucl.Pys.*, **B439** (1995) 471
- [50] H1 Collaboration, T. Ahmed et al., *Phys.Lett.* **B354** (1995) 494
- [51] R. Eichler and S. Frixione, Proceedings of the Workshop on Future Physics at HERA, Hamburg, 1995/96, hep-ph/9609337, Editors: A. De Roeck, R. Klanner
- [52] W. Erdmann et al., *Nucl. Inst. Meth.* **A372** (1996) 188
- [53] R. Horisberger and D. Pitzl, *Nucl. Inst. Meth.* **A326** (1993) 92
- [54] D. Pitzl et al., *Nucl. Inst. Meth.* **A348** (1994) 454
- [55] J. Gassner, Dipl. Thesis, ETHZ-IPP Internal Report 96-4, December 1996
- [56] H. Niggli, Dipl. Thesis, ETHZ-IPP Internal Report 94-5, Oktober 1994
- [57] S. Steiner, private communication
- [58] S. Prell, Ph.D. Thesis, University of Hamburg, 1996, DESY FH1-96-02
- [59] G. Klaiber, Diploma Thesis, ETHZ-IPP Internal Report 95-5, September 1995
Roland Horisberger, private communication
- [60] M. Lindström, *Nucl. Inst. Meth.* **A357** (1995) 129

Acknowledgements

I would like to thank my colleagues in the H1 Collaboration for their support and for creating a nice working atmosphere, especially in the 'North Hall'.

Particularly I thank Ralph Eichler for giving me the possibility to work in his group and for his continuous help and encouragement.

I am grateful to Roland Horisberger, who introduced me into the world of electronics and chips and agreed to be my co-examiner. Working with him was a pleasure.

Many thanks to Kurt Gabathuler, who put up with me as a room mate. His dry sense of humour and 'optimistic' views helped me in many situations.

Daniel Pitzl deserves my gratitude for the excellent teamwork and expertise during many long hours in the electronic trailer debugging the silicon tracker.

Thank you very much to all other members of the CST group: Wolfram Erdmann, Hubert Niggli, Stefano Passaggio, Silvan Streuli. I very much enjoyed working with you!

Christoph Grab receives my special thanks for introducing me into physics analysis and the mysteries of computing at H1.

Thanks to all members of the Hamburg Zürich group for their support and help: Urs Langenegger, Martin zur Nedden, Katharina Müller, David Müller and Yorgos Tsipolitis.

Of course, there are many people who I should thank, who have helped me during the last four years, but there are so many, that it is impossible for me to name all of them individually. Never the less, THANK YOU!

I don't know how I can thank Phillip Biddulph enough. His love and humour kept me going.

Finally I would like to thank my parents and my sister for their moral support and encouragement.

Curriculum vitae

Name: Monika Biddulph
Maiden Name: Wagener
Date of Birth: 14. October 1966
Place of Birth: Siegen, Germany
Nationality: german

Education

1973 - 1977 Katholische Grundschule, Rudersdorf
1977 - 1986 Gymnasium am Rosterberg, Siegen
1986 Abitur
1986 - 1992 Study of Physics at the Universität-Gesamthochschule Siegen
1990 - 1992 Diploma Work in Experimental Physics
Title: "Dynamische Effekte durch Raumladung und Rekombination
in einer Ionisationskammer mit Frischgitter"
1993 - 1997 Graduate Education in Experimental Physics at the
Swiss Federal Institute of Technology (ETH Zürich), Zürich